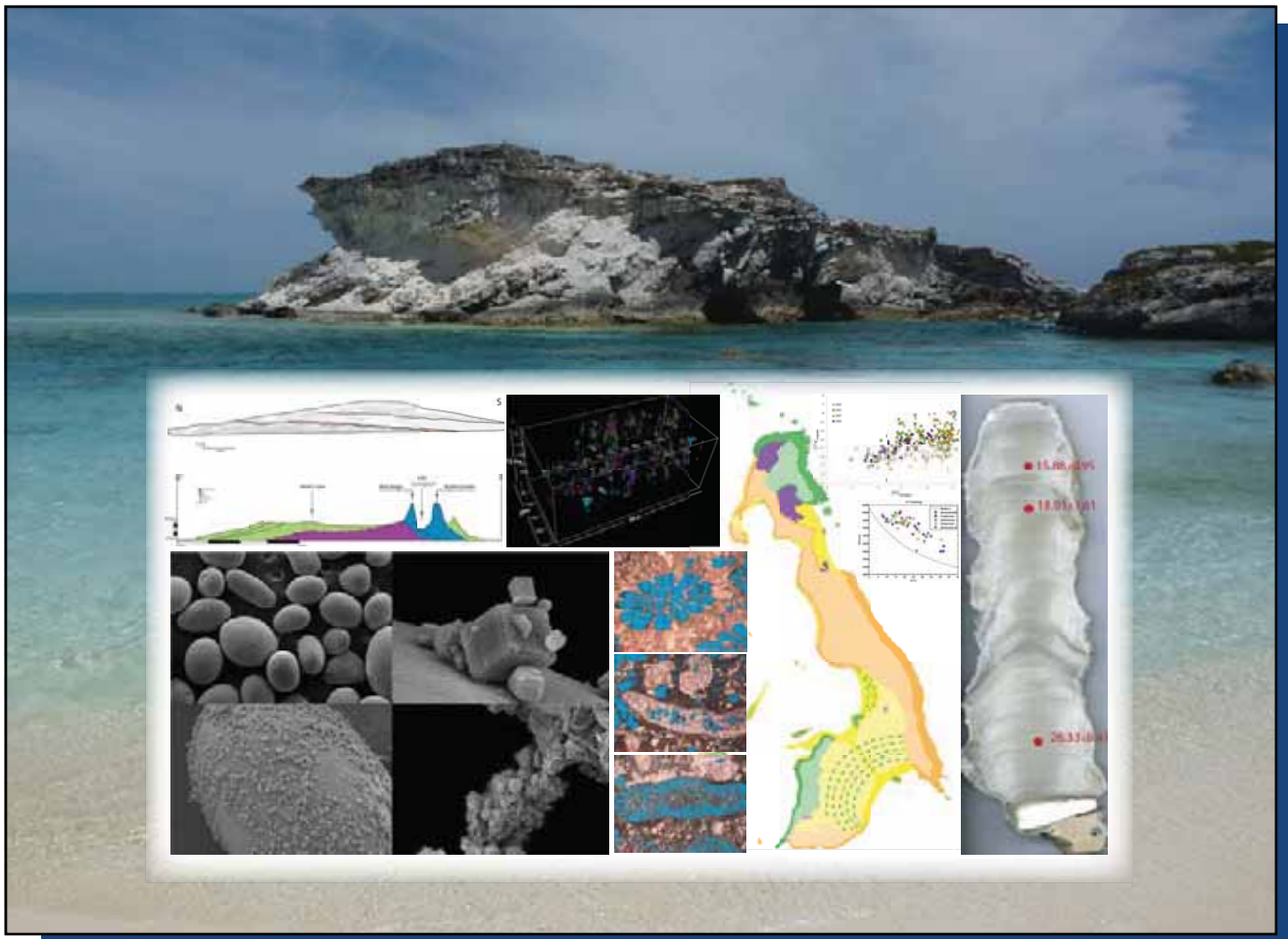


Comparative Sedimentology Laboratory

Rosenstiel School of Marine and Atmospheric Science
University of Miami



Annual Review Meeting
October 11 - 12, 2010



Comparative Sedimentology Laboratory

Rosenstiel School of Marine and Atmospheric Science
University of Miami



Annual Review Meeting
October 11 - 12, 2010



CSL Annual Review Meeting 2010

Table of Contents

Meeting Program	iii
Meeting Participants	vii
Industrial Associates Field Seminar Participants	ix
CSL Associates	xi
Complex Holocene Sediment Accretion around Antecedent Pleistocene Topography, Exumas, Bahamas <i>Kelly L. Jackson, Angela Pumputis, Ani Aiza Asha'ari, Gregor P. Eberli, Donald F. McNeill, and Paul M. ("Mitch") Harris</i>	1
Sedimentological Evidence for Sub-Orbital Sea Level Changes within the Last Interglacial, New Providence Island, Bahamas <i>Samuel B. Reid, Gregor P. Eberli, Donald F. McNeill, Paul M. (Mitch) Harris, Klaas Verwer, and Darrell Kaufman</i>	7
Spatial Variation of Facies and Early Diagenetic Sequences on Glover's Reef <i>Noelle J. Van Ee, Gregor P. Eberli, Eberhard Gischler, and Govert J. Buijs</i>	13
Using Isotopic Tools to Understand Effects of Elevated Nutrient Levels on Scleractinian Corals <i>Quinn B. Devlin and Peter K. Swart</i>	19
Depositional Architecture, Hydrodynamics, and Morphometrics of Cold-Water Coral Mounds on the slope of Great Bahama Bank <i>Thiago B.S. Correa, Mark Grasmueck, Gregor P. Eberli, Klaas Verwer and Sam Purkis</i>	21
Revisiting the Concept of Reciprocal Sedimentation <i>Gregor P. Eberli</i>	27
No Need for Fractures – the Matrix Dual-Porosity System of the Upper Quintuco in the Neuquén Basin, Argentina <i>Michael Zeller, Guillermina Sagasti Crippa, Maria A. Celentano, Pablo A. Crespo, Anthony R. Thompson, Jose Luis Massafarro, Klaas Verwer, Gregor P. Eberli</i>	31
Computational modeling of carbon dioxide sequestration in saline reservoirs <i>Caitlin M. Augustin, Peter K. Swart, Timothy H. Dixon</i>	37
Sulfur and Carbon Isotopic Variation in the Lower Carboniferous: Evidence for OAEs <i>Peter K. Swart, Samantha Evans, Gregor P. Eberli, and David Katz</i>	39

The $\delta^{13}\text{C}$ of Organic Material in Platform Derived Sediments: Implications for Reconstructing the Global Carbon Cycle <i>Amanda Oehlert, Kathryn Lamb-Wozniak, Quinn Devlin, Greta J. Mackenzie, John J.G. Reijmer, and Peter K. Swart</i>	43
Speleothems from Bahamas Blue Holes: Geochemical archives of Atlantic climate variability <i>Monica M. Arienzo and Peter K. Swart</i>	47
The Use of Multiply Substituted ‘Clumped’ Isotopologues in Carbonate Geochemistry <i>Sean T. Murray and Peter K. Swart</i>	49
Characterization of Onlapping Reef Sequences: The Dominican Republic Drilling Project <i>James S. Klaus, Donald F. McNeill, Albertus Ditya, Yula Hermanati, Gregor Eberli, and Peter Swart</i>	51
Sonic Velocity Variations in Pleistocene Reef Systems, southern Dominican Republic <i>Albertus Ditya, Gregor P. Eberli, Donald F. McNeill, and James Klaus</i>	55
Isotope Signature as a Tool for Meteoric Diagenesis <i>Yulaika Hernawati, Don McNeill, Jim Klaus, Gregor P. Eberli, & Peter K. Swart</i>	59
Large carbon isotopic changes preceding Pleistocene glaciations cast doubt on Neoproterozoic Snowball Earth Interpretations <i>Peter K. Swart and Martin J. Kennedy</i>	61
The Determination of Leakage of Carbon Dioxide from Reservoirs Using Cavity Ring Down Spectrometry <i>Ben Galfond, Dan Riemer, and Peter K. Swart</i>	65
Best Practice for Acquisition, Processing, and Interpretation of 3D GPR Data to Visualize Deformation Bands, Fractures, and Karst in Carbonates <i>Mark Grasmueck and Pierpaolo Marchesini</i>	67
Visualization and Quantification of fracture-related Karst in Barremian limestones, Cassis, France <i>Kenri Pomar, Gregor P. Eberli, Mark Grasmueck, and Juliette Lamarche</i>	73
Tracking and Quantifying Fluid Flow in Fractured Cretaceous Carbonates with 4D Ground Penetrating Radar (GPR): Madonna della Mazza Quarry, Italy <i>Pierpaolo Marchesini, Mark Grasmueck, Gregor P. Eberli, Remke L. Van Dam</i>	79
Effect of pore structure on electrical resistivity in carbonates <i>Klaas Verwer, Gregor P. Eberli & Ralf J. Weger</i>	85
Sonic Velocity of Holocene Interparticle Porosity Rocks <i>Gregor P. Eberli, Ralf J. Weger, and Klaas Verwer</i>	91
From Sediment to Rock: Velocity Evolution during Controlled CaCO_3 Precipitation <i>Ralf J. Weger, Peter Swart, and Gregor P. Eberli</i>	95

Meeting Program

Comparative Sedimentology Laboratory

2010 Annual Review Meeting

Monday, October 11 th		Morning
08:30	Coffee	
9:00-9:20	Complex Holocene Sediment Accretion around Antecedent Pleistocene Topography, Exumas, Bahamas <i>Kelly L. Jackson, Angela Pumputis, Ani Aiza Asha'ari, Gregor P. Eberli, Donald F. McNeill, and Paul M. ("Mitch") Harris</i>	
9:20-9:40	Sedimentological Evidence for Sub-Orbital Sea Level Changes within the Last Interglacial, New Providence Island, Bahamas <i>Samuel B. Reid, Gregor P. Eberli, Donald F. McNeill, Paul M. (Mitch) Harris, Klaas Verwer, and Darrell Kaufman</i>	
9:40-10:00	Spatial Variation of Facies and Early Diagenetic Sequences on Glover's Reef <i>Noelle J. Van Ee, Gregor P. Eberli, Eberhard Gischler, and Govert J. Buijs</i>	
10:00-10:10	Using Isotopic Tools to Understand Effects of Elevated Nutrient Levels on Scleractinian Corals <i>Quinn B. Devlin and Peter K. Swart</i>	
10:10-10:30	Coffee Break	
10:30-11:00	Depositional Architecture, Hydrodynamics, and Morphometrics of Cold-Water Coral Mounds on the slope of Great Bahama Bank <i>Thiago B.S. Correa, Mark Grasmueck, Gregor P. Eberli, Klaas Verwer and Sam Purkis</i>	
11:00-11:20	Revisiting the Concept of Reciprocal Sedimentation <i>Gregor P. Eberli</i>	
11:20-11:40	No Need for Fractures – the Matrix Dual-Porosity System of the Upper Quintuco in the Neuquén Basin, Argentina <i>Michael Zeller, Guillermina Sagasti Crippa, Maria A. Celentano, Pablo A. Crespo, Anthony R. Thompson, Jose Luis Massafiero, Klaas Verwer, Gregor P. Eberli</i>	
11:40-11:45	Computational modeling of carbon dioxide sequestration in saline reservoirs <i>Caitlin M. Augustin, Peter K. Swart, Timothy H. Dixon</i>	
12:00	Lunch	

- 13:00-13:20 Sulfur and Carbon Isotopic Variation in the Lower Carboniferous: Evidence for OAEs
Peter K. Swart, Samantha Evans, Gregor P. Eberli, and David Katz
- 13:20-13:35 The $\delta^{13}\text{C}$ of Organic Material in Platform Derived Sediments: Implications for Reconstructing the Global Carbon Cycle
Amanda Oehlert, Kathryn Lamb-Wozniak, Quinn Devlin, Greta J. Mackenzie, John J.G. Reijmer, and Peter K. Swart
- 13:35-13:40 Speleothems from Bahamas Blue Holes: Geochemical archives of Atlantic climate variability
Monica M. Arienzo and Peter K. Swart
- 13:40 -13:45 The Use of Multiply Substituted ‘Clumped’ Isotopologues in Carbonate Geochemistry
Sean T. Murray and Peter K. Swart
- 13:45-14:15 Coffee Break
- 14:15 -14:45 Characterization of Onlapping Reef Sequences: The Dominican Republic Drilling Project
James S. Klaus, Donald F. McNeill, Albertus Ditya, Yula Hermanati, Gregor Eberli, and Peter Swart
- 14:45 -15:00 Sonic Velocity Variations in Pleistocene Reef Systems, southern Dominican Republic
Albertus Ditya, Gregor P. Eberli, Donald F. McNeill, and James Klaus
- 15:00 -15:05 Isotope Signature as a Tool for Meteoric Diagenesis
Yulaika Hernawati, Don McNeill, Jim Klaus, Gregor P. Eberli, & Peter K. Swart
- 15:30 Core Workshop
Dominican Republic Cores / Exumas Cores
- 16:30 Reception in Commons

- 08:00 Coffee
- 8:30-8:50 Large carbon isotopic changes preceding Pleistocene glaciations cast doubt on Neoproterozoic Snowball Earth Interpretations
Peter K. Swart and Martin J. Kennedy
- 8:50-8:55 The Determination of Leakage of Carbon Dioxide from Reservoirs Using Cavity Ring Down Spectrometry
Ben Galfond, Dan Riemer, and Peter K. Swart
- 8:55-9:15 Best Practice for Acquisition, Processing, and Interpretation of 3D GPR Data to Visualize Deformation Bands, Fractures, and Karst in Carbonates
Mark Grasmueck and Pierpaolo Marchesini
- 9:15-9:30 Visualization and Quantification of fracture-related Karst in Barremian limestones, Cassis, France
Kenri Pomar, Gregor P. Eberli, Mark Grasmueck, and Juliette Lamarche
- 9:30-10:00 Coffee Break
- 10:00-10:15 Tracking and Quantifying Fluid Flow in Fractured Cretaceous Carbonates with 4D Ground Penetrating Radar (GPR): Madonna della Mazza Quarry, Italy
Pierpaolo Marchesini, Mark Grasmueck, Gregor P. Eberli, Remke L. Van Dam
- 10:15-10:30 Effect of pore structure on electrical resistivity in carbonates
Klaas Verwer, Gregor P. Eberli & Ralf J. Weger
- 10:30-10:45 Sonic Velocity of Holocene Interparticle Porosity Rocks
Gregor P. Eberli, Ralf J. Weger, and Klaas Verwer
- 10:45-11:00 From Sediment to Rock: Velocity Evolution during Controlled CaCO₃ Precipitation
Ralf J. Weger, Peter Swart, and Gregor P. Eberli
- 11:00-12:30 Future Projects & Discussion
- 14:00 Departure for Field Trip

**INDUSTRIAL ASSOCIATES ANNUAL REVIEW MEETING
COMPARATIVE SEDIMENTOLOGY LABORATORY
October 11-12, 2010**

PARTICIPANTS

Aaron Adams

Anadarko Petroleum Corporation
1201 Lake Robbins Drive
The Woodlands, TX 77380
aaron.adams@anadarko.com

Jiro Asada

INPEX Corporation
Akasaka Biz Tower, 5-3-1- Akasaka
Minato-ku, Tokyo 107-6332
JAPAN
Jiro.asada@inpex.co.jp

Ian Billing

Saudi Aramco
Enigneering Building Room X4360
Dhahran 31311
Saudi Arabia
ian.billing@aramco.com

Tina Christie

BP America Inc.
501 WestLake Park Blvd.
Houston, TX 77079
Tina.Christie@bp.com

Marcelle Marques Erthal

Petróleo Brasileiro S/A
CENPES/PDEXP/GSEP
Prédio 20 – Sala 1056B
Rua Horácio Macedo, 950
Cidade Universitária - Ilha do Fundão
21941-915 Rio de Janeiro – RJ, Brazil
mmerthal@petrobras.com.br

Laurel Gandler

Hess Corporation
500 Dallas St.
Houston, TX 77002
lgandler@hess.com

Beatriz Garcia-Fresca (Bea)

Chevron Energy Technology Co.
6001 Bollinger Canyon Rd.
San Ramon, CA 94583-2324
Beatritxe@chevron.com

Paul M. Harris (Mitch)

Chevron Energy Technology Company
6001 Bollinger Canyon Rd., D-1212
San Ramon, CA 94583-2324
MitchHarris@chevron.com

Franek Hasiuk

ExxonMobil Upstream Research Co.
URC-GW3-972B
P.O. Box 2189
Houston, TX 77252-2189
Franek.hasiuk@exxonmobil.com

Iulian Hulea

Shell Intl Exploration & Production B.V.
Postbus 60
2280 AB Rijswijk
The Netherlands
Iulian.Hulea@shell.com

Gareth D. Jones

Chevron Energy Technology Co.
6001 Bollinger Canyon Rd.
San Ramon, CA 94583-2324
Gareth.d.jones@chevron.com

Gianni Mallarino

ConocoPhillips Company
600 N. Dairy Ashford, PR3060
Houston, TX 77079
Gianni.Mallarino@conocophillips.com

Jose Luis Massafarro
YPF S.A.
Dirección Exploración y Desarrollo de
Negocio
Macacha Güemes 515 (C1106BKK), Puerto
Madero
Buenos Aires, Argentina
jmassafarro@ypf.com

Kathleen McFadden (Kat)
ConocoPhillips Company
600 N. Dairy Ashford
Houston, TX 77079
Kat.A.McFadden@conocophillips.com

Paul Milroy
BG Group
100 Thames Valley Park Drive
Reading, Berkshire RG6 1PT
United Kingdom
Paul.Milroy@bg-group.com

Ray Mitchell
Reservoir Quality Prediction,
Technology
ConocoPhillips Company
173 GB, Bartlesville Technology Ctr.
Bartlesville, OK 74004
ray.w.mitchell@conocophillips.com

William Morgan (Bill)
ConocoPhillips Company
600 N. Dairy Ashford – OF3006
Houston, TX 77079-1175
w.a.morgan@conocophillips.com

Wendy Peace
Woodside Energy Ltd.
Woodside Plaza
240 St. Georges Terrace
Perth WA 6000, Australia
Wendy.Peace@woodside.com.au

Scott Pluim
Hess Corporation
500 Dallas St.
Houston, TX 77002
spluim@hess.com

Freyd Rad
Anadarko Petroleum Corporation
1201 Lake Robbins Drive
The Woodlands, TX 77380
Freyd.Rad@anadarko.com

Cinzia Scotellaro
BG Group
100 Thames Valley Park Drive
Reading, Berkshire RG6 1PT
United Kingdom
Cinzia.Scotellaro@bg-group.com

Tsuyoshi Shikama
INPEX Corporation
Akasaka Biz Tower, 5-3-1- Akasaka
Minato-ku, Tokyo 107-6332
JAPAN
Tsuyoshi.shikama@inpex.co.jp

Sarah Thompson
Anadarko Petroleum Corporation
1201 Lake Robbins Drive
The Woodlands, TX 77380
sarah.thompson@anadarko.com

Klaas Verwer
Statoil ASA
Sandsliveien 90
5254 Sandsli, Bergen, Norway
KLVER@statoil.com

Brigitte Vlaswinkel
Shell Intl Exploration & Production B.V.
Postbus 60
2280 AB Rijswijk
The Netherlands
B.Vlaswinkel@shell.com

THE COMPARATIVE SEDIMENTOLOGY LABORATORY & ASSOCIATES
Annual Review Meeting, October 11 & 12, 2010

PRINCIPAL INVESTIGATORS

Gregor P. Eberli	Professor, Seismic Stratigraphy
Mark Grasmueck	Associate Professor, Subsurface Imaging
James Klaus	Assistant Professor, Paleontology
Donald F. McNeill	Scientist, Sedimentology
Peter K. Swart	Professor, Geochemistry

ASSOCIATE SCIENTISTS

Greta Mackenzie
Ralf Weger

SCIENTIFIC COLLABORATORS

Ida Fabricius	Technical University of Denmark
Mark A. Knackstedt	Australian National University
Juliette LaMarche	University of Marseille, France

STUDENTS

Monica Arienzo, Caitlin Augustin, Thiago Correa, Quinn Devlin, Albertus Ditya, Ben Galfond, Yulaika Hernawati, Kelly Jackson, Rosely Marçal, Pierpaolo Marchesini, Irena Maura, Sean Murray, Jan Norbistrath, Amanda Oehlert, Al Piggot, Kenri Pomar, Sam Reid, Angela Rosenberg, Rani Sianipar, Noelle Van Ee, Amanda Waite, Michael Zeller

VISITING STUDENTS

Dayse Daltro
Angela Pumputis

RESEARCH ASSOCIATES

Amel Saied

STAFF

Karen Neher	Office Manager
Cory Schroeder	Technical Specialist

Complex Holocene Sediment Accretion around Antecedent Pleistocene Topography, Exumas, Bahamas

Kelly L. Jackson, Angela Pumputis¹, Ani Aiza Asha'ari², Gregor P. Eberli, Donald F. McNeill, and Paul M. (“Mitch”) Harris³

¹ *Petrobras, Brazil*

² *Universiti Teknologi Petronas, Malaysia*

³ *Chevron Energy Technology Company, San Ramon, CA*

Key Findings

- Windward margin stratigraphic architecture records high-frequency sea level fluctuations within Pleistocene sea level highstands.
- Geologic mapping reveals a complicated juxtaposition of Holocene and Pleistocene grain-dominated stratigraphic units that is more accurate than remote sensing alone.
- Ridges of Pleistocene eolianites formed during marine isotope stages 5e, 9, and 11 build the backbone of the Exuma Cays Land and Sea Park. These ridges provided a template for complex Holocene accretion during the past 6,000 ybp.

Project Motivation

Quaternary high-frequency sea level high stand variability is recorded in the stratigraphic units of the Exumas windward margin of Great Bahama Bank (Figure 1). The Exumas include more than 350 islands (cays) that feature a complex juxtaposition of Pleistocene and Holocene grain-dominated stratigraphic units.



Figure 1: The Exuma Cays are located along the windward margin of Great Bahama Bank forming the western margin of Exuma Sound.

Field mapping and coring in the Exuma Cays Land and Sea Park (ECLSP) (Figure 2) provides insight into the lateral and vertical heterogeneity of depositional facies resulting from sea level highstands with variable frequency and amplitude. During the last sea level highstand 125 kyrs ago in marine isotope stage (MIS) 5e, sea level peaked approximately 6 m higher than present after previously fluctuating for several meters (Thompson and Goldstein, 2005). Older sea level highstands were also higher (MIS 9 at 330 kybp and 11 at 410 kybp) or lower (MIS 7 at 240 kybp) than the present day sea level. Holocene sediment accretion took place during the past 6,000 years.

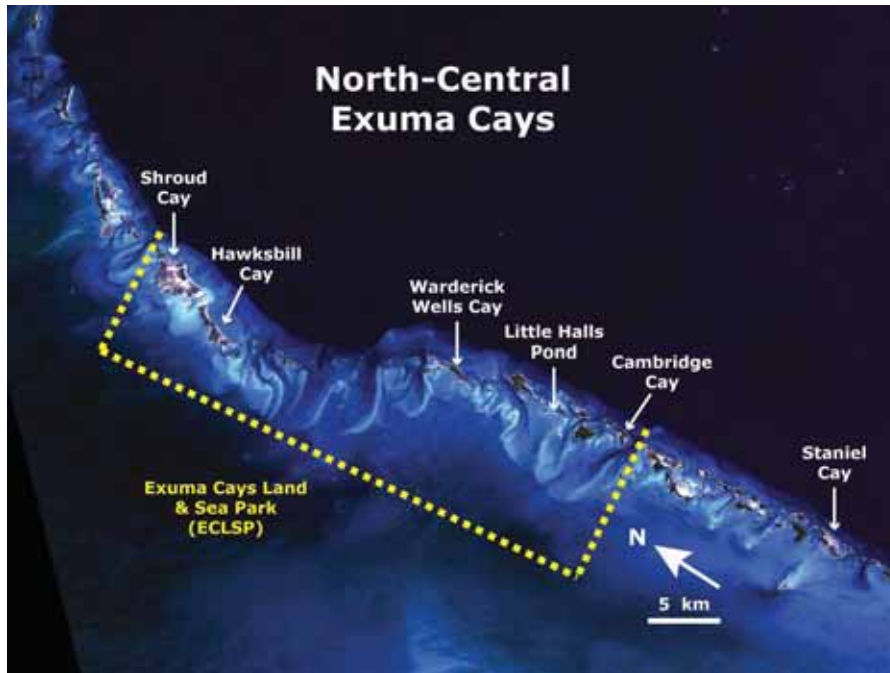


Figure 2: Location of the Exuma Cays Land and Sea Park (ECLSP). Approximately half of the Exuma Cays margin is shown here (Landsat image from Harris and Ellis, 2009).

The first objective of this project is to document sea level highstand variability and its impact on the stacked successions of shallow-water carbonates and eolianites along the Exumas windward margin. Today, the exposed strata display a complicated array of stacked and laterally accreting marine and eolian deposits that have been documented throughout the Bahamas, for example, on New Providence Island (Garret and Gould, 1984; Hearty and Kindler, 1997, see also Reid et al., this volume) as well as on Bimini, Cat, San Salvador, Abaco, and Eleuthera (Kindler and Hearty, 1996). McNeill and Hearty (2009) documented complicated successions and juxtaposition of facies and ages along the southern Exumas windward margin suggesting that the Exumas prograded eastward from the older middle Pleistocene (potentially MIS 11 or 13) to the late Pleistocene (MIS 5e). Petrie (2010) documented the lateral coexistence of grain-dominated Holocene tidal flat and tidal delta deposits with Pleistocene eolianites in Shroud Cay, Exumas.

The second objective of this project is to document the heterogeneity that is generated by the interaction of antecedent topography with Holocene sediment accretion. Detailed geologic maps created by combining satellite imagery and detailed surface mapping of Pleistocene and Holocene strata in the Exumas extends previous work by Petrie (2010).

Preliminary results from Pleistocene cores collected from Warderick Wells and surrounding cays document the vertical successions and stratigraphic heterogeneity in relation to Pleistocene sea level fluctuation.

Heterogeneity

Harris and Ellis (2009) documented that satellite imagery and GIS data can be used to visualize and interpret the geology of the Exumas. While the satellite-derived mapping proved to be a great, user-friendly method, extensive field mapping revealed that ground-truthing is still a necessary component to truly understand the stratigraphic complexities of the Exumas windward margin. Satellite-derived geologic interpretations by Harris and Ellis (2009) for Hawksbill Cay determine the distribution of Pleistocene and Holocene facies (Figure 3 B and C). In the northern part of Hawksbill Cay, the maps derived from remote sensing are accurate for the most part when compared to extensive field mapping conducted in July 2010 (Figure 3 D). The southern portion of Hawksbill Cay, however, shows distinct differences between the satellite-derived interpretations and field mapping.

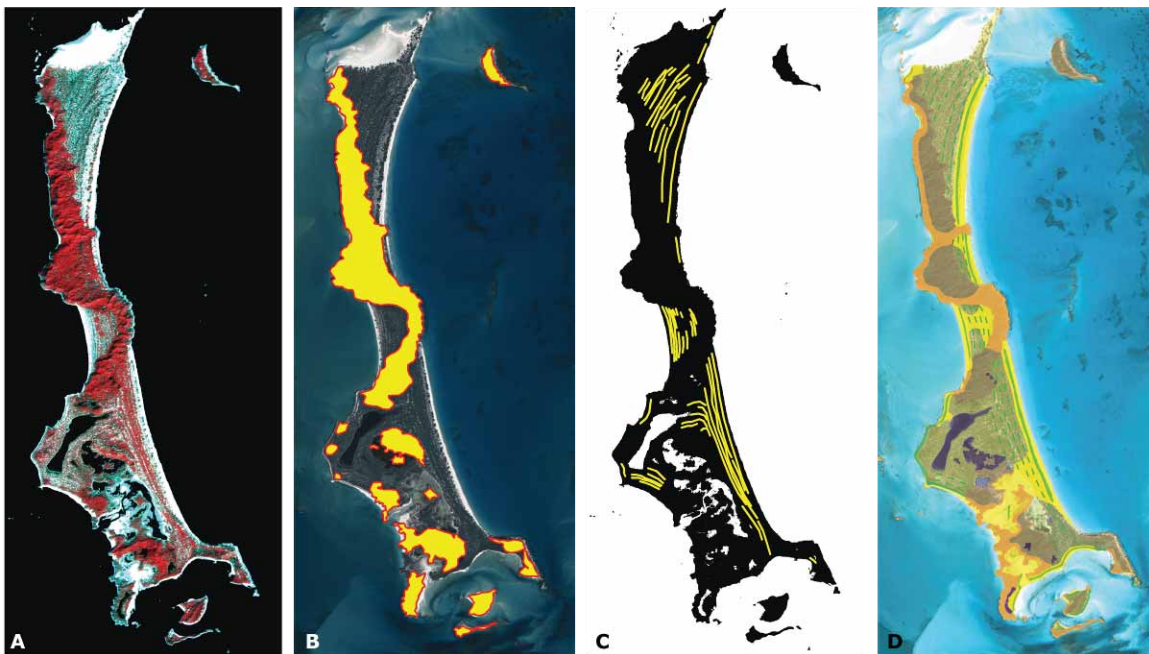


Figure 3: Hawksbill Cay, Exumas. (A) Quickbird CIR image of Hawksbill Cay (Harris and Ellis, 2009), (B) Interpretation of Pleistocene units from Quickbird color image (Harris and Ellis, 2009), (C) Interpretation of Holocene strandlines on Quickbird land mask image (black) (Harris and Ellis, 2009), (D) Geologic interpretation from field mapping in July 2010.

To document the complex lateral heterogeneity of the Exumas windward margin, geologic mapping was conducted on 15 large and numerous smaller cays within the Exuma Cays Land and Sea Park (ECLSP), which covers 456 km² and extends 35 km along the platform margin. Heterogeneity is generated by the interaction of antecedent topography with younger accretion where juxtapositions are often abrupt and discontinuous. Examples from Hawksbill Cay (Figure 3), Warderick Wells, and

Cambridge Cay (Figure 5) illustrate how Holocene sediment accretion fills accommodation space between pre-existing Pleistocene topography. Ridges of Pleistocene eolianites form a backbone to later Holocene sediment accretion on most of the large cays in the ECLSP. Unlike the 1.5 m leeward reef terrace documented in the southern Exumas (Halley et al., 1991), no Pleistocene reef deposits were observed outcropping on any of cays within the ECLSP. Occasionally, fenestral porosity was observed in Pleistocene rocks outcropping near modern sea level suggesting the presence of ancient beach deposits.

Holocene sediment accretion fills accommodation space between Pleistocene eolianite ridges with generally seaward prograding catenary beach ridges (Figure 4) and back beach storm ridges. Emergent Pleistocene headlands form anchors where catenary Holocene beach ridges form and prograde seaward (Figure 4) (Garrett and Gould, 1984; Kindler and Hearty, 1996). These ridges prograde seaward 100 – 500 m and extend shore parallel up to 1 km (i.e., Hawksbill Cay, Figure 3). Cemented back beach storm ridges create vertical successions that are centimeters to several meters in scale and more frequently occur on the leeward side of the cays. Holocene dune complexes accrete vertically (up to 30 m high) on pre-existing Pleistocene topography. These dune complexes occur most often along the windward side of the cays.

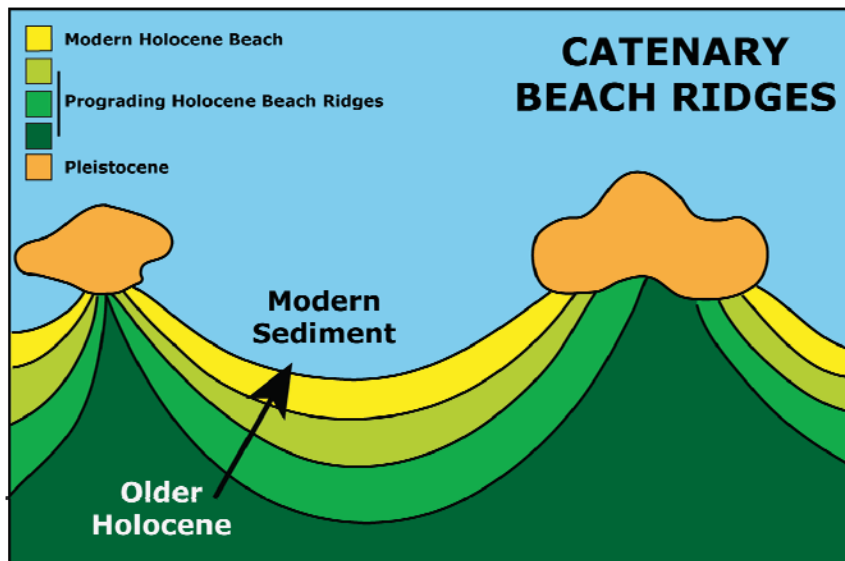


Figure 4. Schematic diagram illustrating the formation of prograding Holocene catenary beach ridges in the Exumas. Pleistocene remnants form anchor points by which catenary ridges can prograde seaward (modified from Kindler and Hearty, 1996).

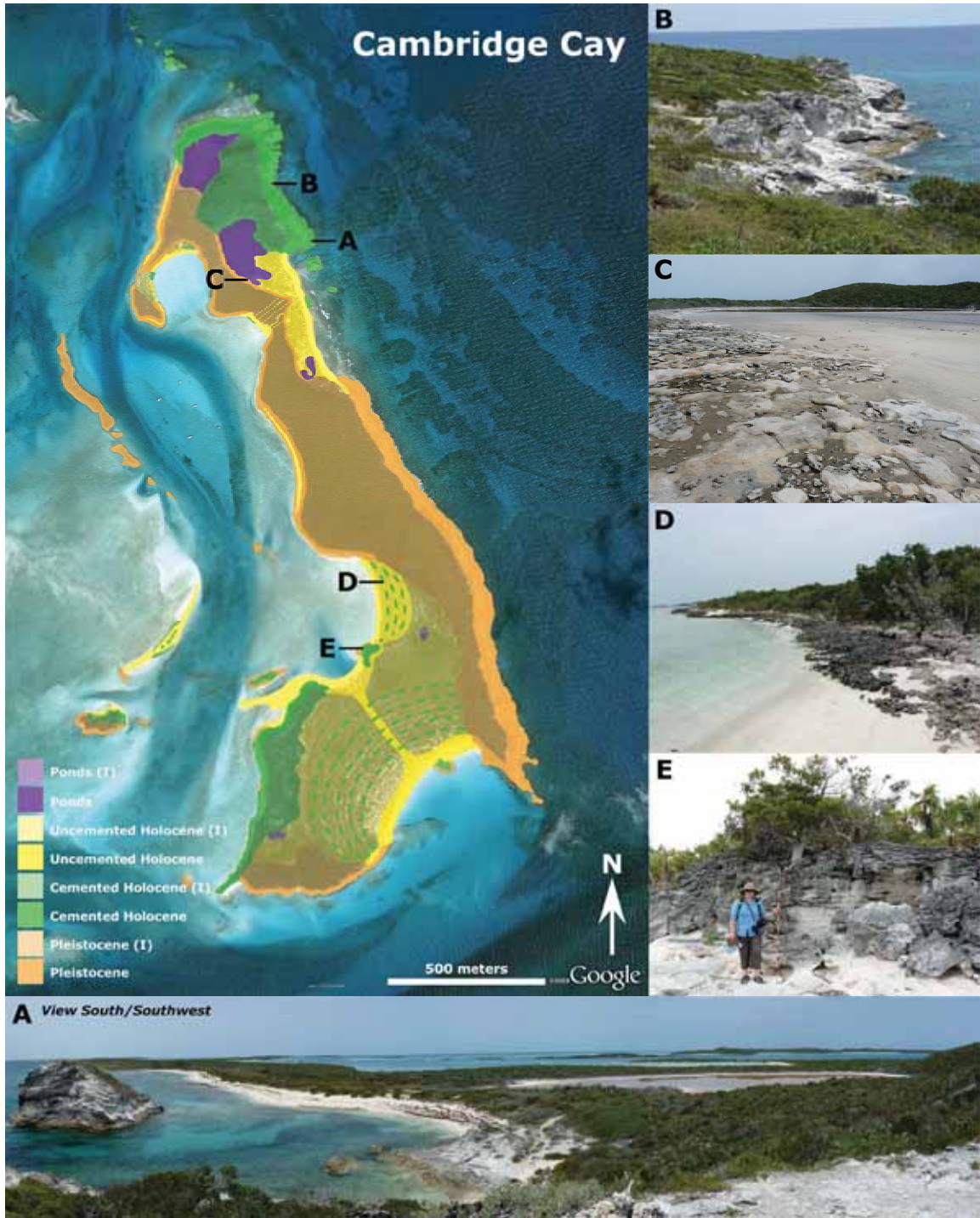


Figure 4: Cambridge Cay displays a prime example of complex Holocene sediment accretion around antecedent Pleistocene topography (Base map from Google Earth, 2010). Color shadings represent observed (darker shades) and interpreted (I) (lighter shades). (A) View south/southwest standing on top of large Holocene dune. (B) View north of eroding cliffs of Holocene dune facies. (C) Pleistocene outcropping along the edge of one of the northern ponds. (D) Pleistocene beach to eolianite facies. (E) 2 m + Holocene back beach storm ridges that developed on the leeward side of Cambridge Cay.

Preliminary results from cores drilled in the ECLSP feature primarily carbonate grainstones that were deposited in subtidal, beach, and eolian environments. Exposure horizons, identified by distinct calcretes, separate up to three distinct Pleistocene successions documenting deposition during three Pleistocene sea level highstands. These are tentatively correlated to MIS 5, 9, and 11 (125, 330, and 410 kybp, respectively).

Summary

Holocene and Pleistocene grain-dominated stratigraphic units in the Exuma Cays Land and Sea Park reveal complicated facies juxtapositions that are often abrupt and discontinuous. Pleistocene antecedent topography resulting from MIS 5e and potentially 9 and 11 directly influenced Holocene sediment accretion during the last 6,000 years. Lateral heterogeneity reveals Pleistocene eolianite ridges filled in or vertically accreted by Holocene prograding catenary beach ridges, back beach storm ridges, and Holocene dune complexes.

References

- Garrett, P., and Gould, S. J., 1984, Geology of New Providence Island, Bahamas: Geological Society of America Bulletin, v. 95, p. 209-220.
- Halley, R. B., Muhs, D. R., Shinn, E. A., Dill, R. F., and Kindinger, J. L., 1991, A +1.5-m reef terrace in the southern Exuma Islands, Bahamas: Geological Society of America Abstracts and Programs, v. 23, no. 1, p. 40.
- Harris, P. M., and Ellis, J., 2009, Satellite imagery, visualization and geological interpretation of the Exumas, Great Bahama Bank: An analog for carbonate sand reservoirs: SEPM Short Course Notes No. 53, DVD.
- Hearty, P. J., and Kindler, P., 1997, The stratigraphy and surficial geology of New Providence and surrounding islands, Bahamas: Journal of Coastal Research, v. 13, no. 3, p. 798-812.
- Kindler, P., and Hearty, P. J., 1996, Carbonate petrography as an indicator of climate and sea-level changes: New data from Bahamian Quaternary units: Sedimentology, v. 43, p. 381-399.
- McNeill, D. F., and Hearty, P., 2009, Windward carbonate margin parasequence geometry linked to precursor topography, Exuma Cays, Bahamas: American Association of Petroleum Geologists Annual Meeting Abstracts, v. 18, p. 140.
- Petrie, M., 2010, Sedimentology of a Grain-dominated Tidal Flat, Tidal Delta, and Eolianite System: Shroud Cay, Exumas, Bahamas: M.S. Thesis, University of Miami, 277 pp., unpublished.
- Thompson, W. G., and Goldstein, S. L., 2005, Open-system coral ages reveal persistent suborbital sea-level cycles: Science, v. 308, p. 401-404.

Sedimentological Evidence for Sub-Orbital Sea Level Changes within the Last Interglacial, New Providence Island, Bahamas

Samuel B. Reid, Gregor P. Eberli, Donald F. McNeill, Paul M. (Mitch) Harris, Klaas Verwer, and Darrell Kaufman

Key Findings

- Paleosols within coeval MIS 5e eolianites and calcretes within foreshore deposits indicate a sea-level fall during the last interglacial highstand
- Downstepping of beach and foreshore facies in a prograding system records the onset of sea-level fall at the end of the interglacial
- The heterogeneity associated with sea-level changes during MIS 5e indicates that a high amount of complexity could be expected with any sea-level highstand

(In)Stability of Pleistocene Sea Level Highstands

Several authors have proposed that the interglacial periods exhibit variations in sea level of a magnitude that would influence shallow-water deposition. For example, Thompson and Goldstein (2005) proposed a sea-level drop of ~ 17 m within the last interglacial (MIS 5e; Fig. 1B). Such a sea level drop would have exposed the entire platform and should be recorded in exposure surfaces within the marine deposits. It should also have produced a break in the eolian deposits as the sediment source feeding the dunes shifted basinward. This study aims to unravel the sedimentary response to the water depth variations within sea-level highstands in both the marine and eolian deposits that form New Providence Island in the Bahamas.

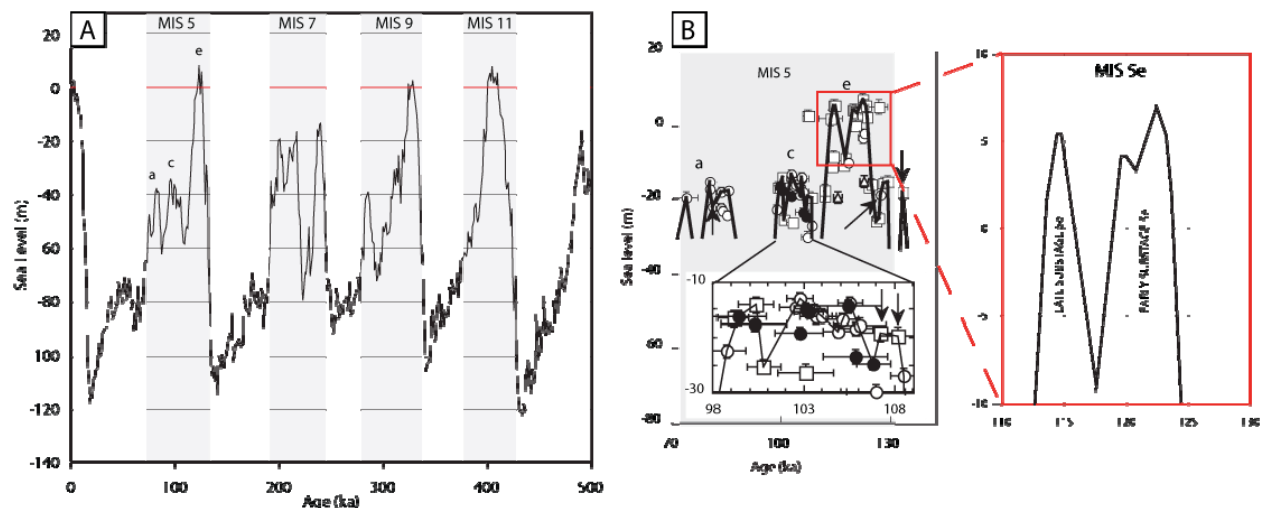


Figure 1: (A) Sea-level curve over the last 500 ka based on stable isotope data (from Lisiecki and Raymo, 2005) with the marine isotope stages labeled on top. (B) Evidence of a mid-highstand sea-level fluctuation of ~17 m within MIS 5e based on coral terraces in Barbados (redrawn from Thompson and Goldstein, 2005).

When did New Providence Island form?

New Providence is an $\sim 200 \text{ km}^2$ island (12 km N-S x 30 km E-W) situated at the northwest corner of the New Providence Platform of Great Bahama Bank. It formed during the last three Pleistocene highstands by lateral accretion and vertical succession of subtidal, foreshore, beach, and eolian deposits (Garrett and Gould, 1984; Hearty and Kindler, 1997). Garrett and Gould (1984) first documented both marine and eolian facies and mapped lateral relationships between these facies across the island. Based on the evolutionary history of the land snail *Cerion sp.*, they demonstrated that the deposits spanned a number of ages in the Pleistocene (Phases IA, IB, IC, and II) and Holocene (Phase III). They correlated Phase II with the $\sim 125 \text{ ka BP}$ highstand now generally referred to as Marine Isotope Stage 5e (MIS 5e).

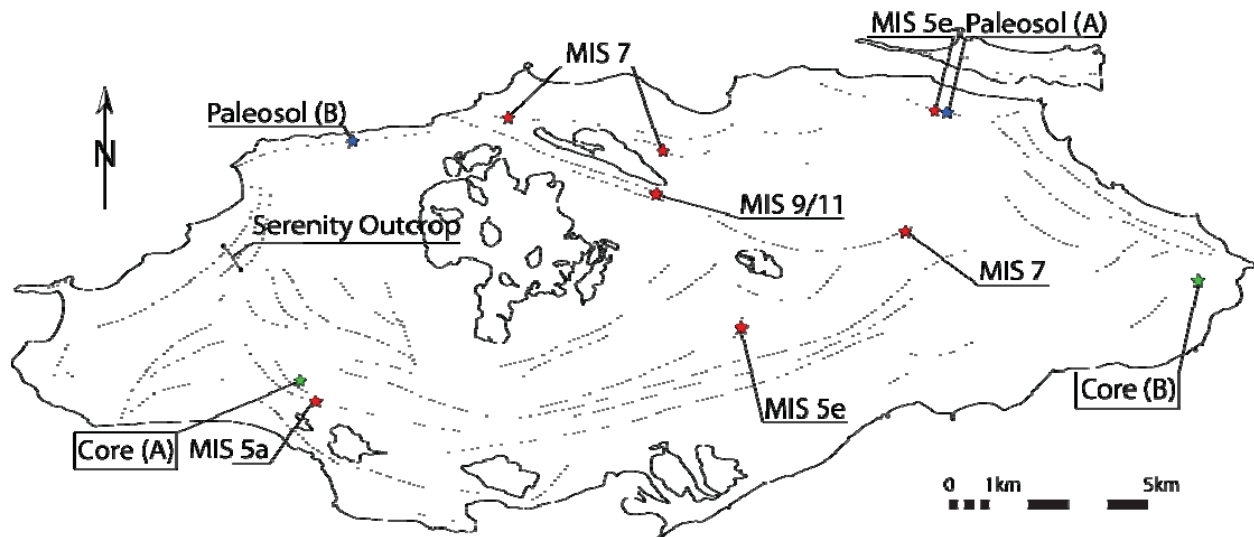


Figure 2: Map of New Providence Island with ridge axes traced as dashed lines. AAR sample locations are shown as red stars, with dates calibrated to the Pleistocene marine isotope stages. Green stars are the locations of two important cores (Fig. 5), blue stars are paleosol locations (Fig. 3).

Hearty and Kindler (1997) re-visited New Providence to better date the chronology of Garrett and Gould's (1984) "Phases" according to the marine isotopic stage (MIS) scale of Imbrie *et al.* (1984). Based on amino acid racemization (AAR) values on both *Cerion* land snails and bulk rock samples, island accretion was interpreted to occur during MIS 1, 5a, 5e, 7, 9, and 11. The new AAR values from this study also yielded dates from MIS 9/11, MIS 7, MIS 5e, and MIS 5a across New Providence (Fig. 2).

These ages are not easy to reconcile with the sea-level curves constructed from oxygen isotope values of benthic foraminifers for each Marine Isotope Stage (Fig. 1). For example, sea level during MIS 7 200 ka ago was -17 m below modern mean sea level, which makes platform-top deposition during that time unlikely (Fig. 1). Similarly, MIS 5a ($\sim 87\text{--}77 \text{ ka}$) is estimated to have peaked at $\sim -17 \text{ m}$ below modern mean sea level (Thompson and Goldstein, 2005, Fig. 1B). However, Dorale *et al.* (2010) provide some evidence from caves in Mallorca that sea level at that time was $\sim +1 \text{ m}$ above present mean sea level. Consequently, flooding of New Providence Island during MIS 5a might have taken place. Additional dating is planned to solve the discrepancies.

Sea Level Instability within the last interglacial (MIS 5e)

The eolian deposits on New Providence Island contain evidence of a sea-level fall within the last interglacial (MIS 5e) as postulated by Thompson and Goldstein (2005). Within two peloidal eolian ridges, a similar paleosol is observed (Fig. 3). The two ridges have been dated using AAR chronology to be MIS 5e. The two paleosols show a similar light orange hue with well cemented rhizomorphs and abundant *Cerion* shells in the back-weathering strata. Both paleosols also show early development of a soil breccia.

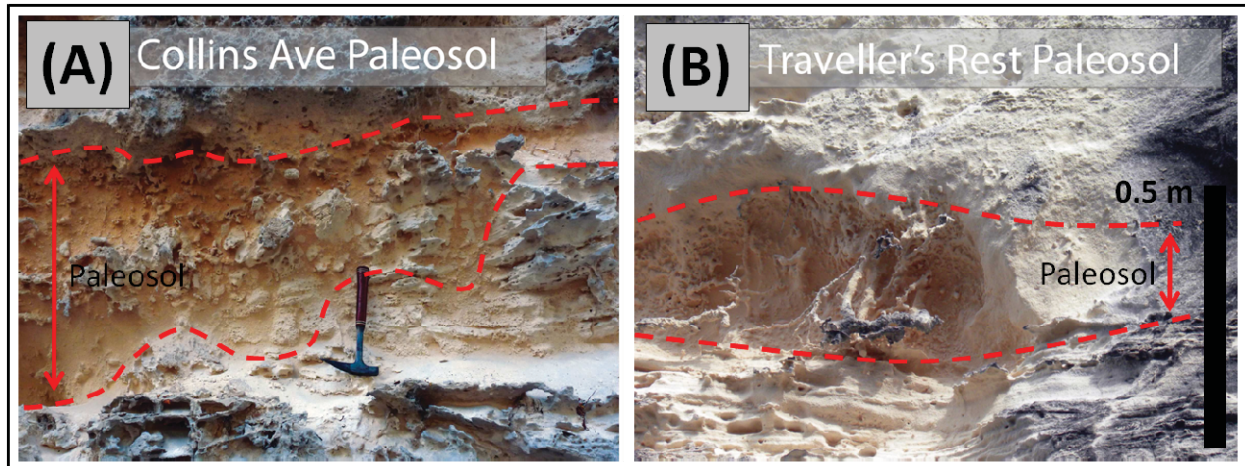


Figure 3: Two similar paleosols within MIS 5e eolian dunes. (A) Paleosol showing a soil breccia at Collins Ave, Nassau Ridge. (B) Paleosol with apparent rhizomorphs weathering out in a roadcut near Traveller's Rest, Gambier Ridge.

Marine and Eolian Deposition During MIS 5e Falling Sea Level

Stacking patterns within foreshore, beach, back-beach, and eolian deposits at the Serenity outcrop document vertical and lateral facies architectures within a prograding marine and eolian system during a falling sea level. In the middle ridge of Serenity, foreshore deposits can be traced up dip to beach and then back-beach deposits (Fig. 4, lower panel). Capping these deposits are lenses of south-dipping eolian foresets overlying poorly developed paleosols in troughs between back-beach dune ridges. The northern ridge exhibits little to no cross-bedded foreshore deposits, but NW-dipping beach deposits can be traced into eolian backset beds.

The lower deposits of the middle ridge are interpreted to have been a northwestward prograding foreshore, beach, and back-beach complex under static sea level. In the northern ridge, a drop in foreshore deposits indicates a falling sea level between deposition of the middle and northern ridges. Additionally, lenticular bedsets of eolian foresets capping the middle ridge indicate an increase in sediment source subsequent to deposition of the middle ridge, possibly due to deflation of offshore sediments during sea-level drop.

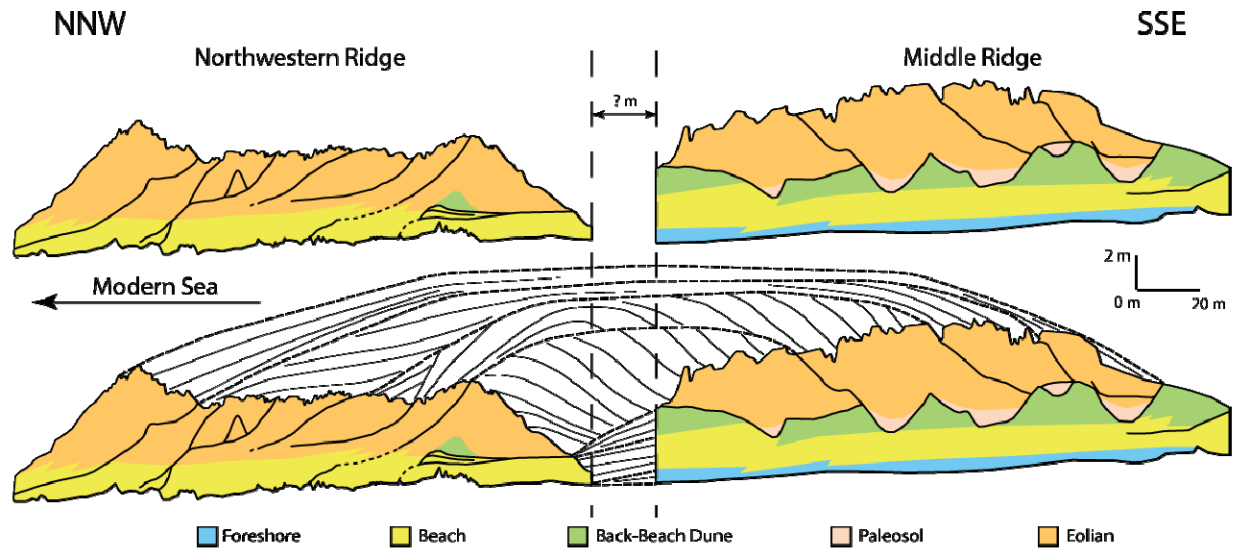


Figure 4: Diagrams of the middle and northwestern ridges of the Serenity outcrop. Bounding surfaces are traced, and interpreted environments are colored accordingly. Note the presence of foreshore and back-beach deposits in the middle ridge but not the northwestern ridge. Eolian deposits have been correlated between the two ridges. Outcrop location can be seen in Fig. 2.

Punctuated Sea Level Fall and Fluctuation at the End of the Last Interglacial (MIS 5e)

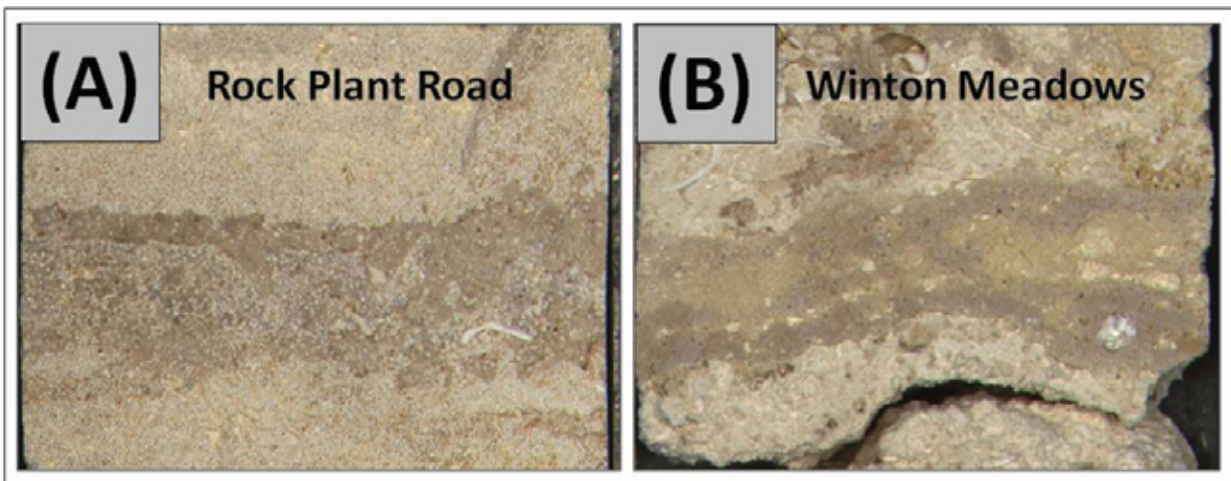


Figure 5: Sections of short cores taken in southern MIS 5 deposits on New Providence Island (Fig. 2.) showing a correlative calcrete horizon across the southern portion of the island. Cores are ~ 7 cm across.

Beach ridges across southern New Providence Island have been shown to exhibit downstepping during progradation. A short core (<1 m) taken between two of the southern beach ridges reveals a thin calcrete (Fig. 5A). A similar calcrete (Fig. 5B) has been identified in a separate core from the southeastern portion of the island (Winton Meadows) and is interpreted as being coeval with the southwestern deposits based on the geomorphology of the southern

ridges (Fig. 2). These two calcretes within uppermost marine foreshore facies indicate a period when sea-level dropped and rose again, further complicating the downstepping pattern of beach deposits.

Conclusions

Evidence for sub-orbital sea-level changes is preserved within the MIS 5 deposits on New Providence. A matched paleosol in northern eolian deposits and a similar calcrete across the southern beach ridges suggests an island-wide period of non-deposition interpreted to be a sea-level drop. This is consistent with sub-orbital changes suggested by Thompson and Goldstein (2005). Additionally, prograding beach-dune complexes on the northwestern rim of the island show evidence of falling sea level during progradation by a drop in the level of foreshore and beach deposits. These sedimentological indicators are evidence for small-scale sea-level fluctuations within the last interglacial.

References

- Dorale, J.A., Onac, B.P., Fornós, J.J., Ginés, J., Ginés, A., Tuccimei, P., Peate, D.W., 2010, Sea-level highstand 81,000 years ago in Mallorca: *Science*, v. 327, p. 860-863.
- Garrett, P., and Gould, S.J., 1984. *Geology of New Providence Island, Bahamas: Geological Society of America Bulletin*, v. 95, p. 209-220.
- Haddad, G.A., Droxler, A.W., Kroon, D., and Müller, D.W., 1993. Quaternary CaCO₃ input and preservation within Antarctic intermediate water: mineralogic and isotopic results from holes 818B and 817A, Townsville Trough (Northeastern Australia margin): *Proceedings of the Ocean Drilling Program, Scientific results*, v. 133, p. 203-233.
- Hearty, P.J., and Kindler, P., 1997. The stratigraphy and surficial geology of New Providence and surrounding islands, Bahamas: *Journal of Coastal Research*, v. 13, n. 3, p. 798-812.
- Imbrie, J., Hays, J.D., Martinson, D.G., McIntyre, A., Mix, A.C., Morley, J.J., Pisias, N.G., Prell, W.L., and Shackleton, N.J., 1984. The orbital theory of Pleistocene climate: support from a revised chronology of the marine ¹⁸O record. *In: Berger, A.L. et al. (eds.), Milankovitch and Climate, Part I*, Dordrecht: Reidel, p. 269-305.
- Kaufman, A., Broecker, W.S., Ku, T.-L., and Thurber, D.L., 1971. The status of U-series methods of mollusk dating: *Geochimica et Cosmochimica Acta*, v. 35, p.1155-1183.
- Lisiecki, L.E. and M.E. Raymo. 2005. LR04 Global Pliocene-Pleistocene Benthic d18O Stack. IGBP PAGES/World Data Center for Paleoclimatology Data Contribution Series #2005-008. NOAA/NGDC Paleoclimatology Program, Boulder, CO, USA.
- Thompson, W.G. and Goldstein, S.L. 2005, Open system coral ages reveal persistent suborbital sea-level cycles: *Science*, v. 308, p. 401-404.

Spatial Variation of Facies and Early Diagenetic Sequences on Glover's Reef

Noelle J. Van Ee, Gregor P. Eberli, Eberhard Gischler¹, and Govert J. Buijs²

¹Goethe University, Frankfurt am Main, Germany ²ConocoPhillips, Houston, TX

Key Findings

- Preliminary data suggest the presence of suborbital sea-level cycles
- Interplay between the physical and biological environments on Glover's Reef introduces facies heterogeneity
- Extensive porosity changes, dissolution, cementation and re-crystallization occur in relatively young rocks

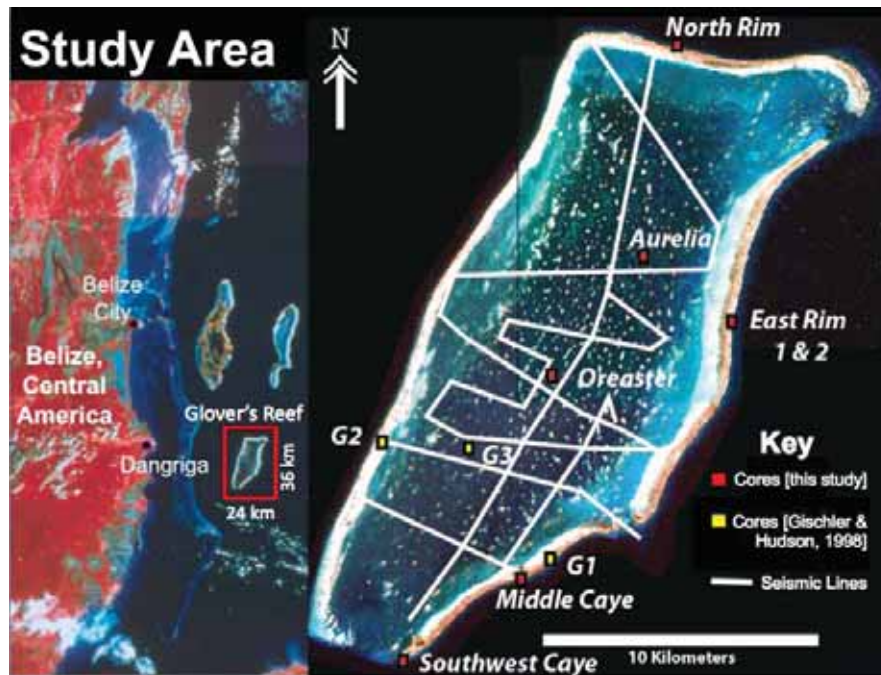


Figure 1: Study area of Glover's Reef, Belize shown with core locations and seismic data.

Geological Investigation on Glover's Reef

Glover's Reef is a 260 km² reef-rimmed platform off the coast of Belize, Central America. As reported last year, Glover's Reef modern facies distribution and patch reef morphology is influenced by the predominant northeast wind direction and the antecedent topography. 111 km of seismic lines across the platform lagoon images antecedent highs beneath 95% of the Holocene patch reefs. That these antecedent highs are Pleistocene reefs has been verified by rotary core drilling (Van Ee et al., 2009).

This follow-up study focuses on the geochemical, petrographical, and lithological investigation of the eight rotary cores taken from six locations across Glover's Reef in

2009. Three rotary cores taken in an east to west transect [originally described by Gischler and Hudson (1998)] provide additional information. Together, these core datasets offer excellent coverage of the platform and illustrate the variability present even within platform top reef deposits.

Suborbital Sea-level Oscillations

A growing body of evidence worldwide supports the presence of suborbital sea-level fluctuations during the Last Interglacial, Marine Isotope Stage 5e (Hearty et al., 2007). Just north of Belize, on the Yucatán peninsula of Mexico, U-series dated, back-stepping reef crest deposits are compelling evidence for a rapid rise in sea level and high stand instability during this time frame (Blanchon et al., 2009). Preliminary data from Strontium isotope and Amino Acid Racemization (AAR) measurements suggest suborbital sea-level cycles are recorded on Glover’s Reef as well.

Strontium isotope ratios were measured for two *Spondylus* (thorny oyster) shells and one *Acropora palmata* (coral) frond. These samples were taken from the Aurelia, Oreaster, and Middle Caye cores, respectively. Stable carbon and oxygen isotope values for all samples plot within the range acceptable for modern marine carbonates, indicating that the samples were taken from a closed system. Despite spanning a wide depth range and several exposure horizons, the results are just below the modern seawater value of 0.7092 (Table 1). The values are very similar to those reported by Gischler et al. (2010) for slightly greater depths and suggest deposition between 0-280 kyr before present (BP) with a mean age of 140 kyr BP (Farrell et al., 1995).

Table 1: $^{87}\text{Sr}/^{86}\text{Sr}$ measurement results for three Glover’s Reef samples.

Sample	Depth (mbsl)	Fossil	$^{87}\text{Sr}/^{86}\text{Sr}$	Std error (%)	Interpreted Age (Mean)
SrAR	6.7	<i>Spondylus sp.</i>	0.709184	0.0010	140 kyr
SrOR	9.0	<i>Spondylus sp.</i>	0.709182	0.0009	140 kyr
XM-36	15.4	<i>A. palmata</i>	0.709180	0.0010	140 kyr

Amino acid geochronology uses the changes in indigenous proteins preserved in carbonate skeletons to estimate the time elapsed since the death of the organism. Racemization, the inversion of L-amino acids to their D-configuration (DL), is the most commonly measured change. The rate at which this change occurs is controlled primarily by temperature, although it also varies with taxonomy, therefore, it is best to measure a suite of monospecific samples from regions with similar geothermal histories (Miller and Brigham-Grette, 1989). AAR geochronology has the capability of extending chronological information on Glovers Reef beyond the range of radiocarbon dating and without the sensitivity to aragonite preservation of U-series dating. Results from a pilot test on seven samples of *Montastraea annularis* from the Southwest Caye core and one sample from the Reef Point outcrop on Ambergris Caye, northern Belize are promising (Figure 2). The Glover’s Reef samples plot in chronostratigraphic order, with one exception, SW3. This sample is from the top of the Pleistocene and may have been artificially aged by heat generated by friction between the drill bit and exposure surface.

Samples SW4-6 cluster, indicating a similar age. In the core they are, however, separated by an exposure surface. This exposure within similar age (MIS 5e) strata is strong evidence of a short (thousands of years) fall of sea level during the last interglacial. A larger sample suite and calibration with Carbon-14 dates will elucidate questions about the presence of suborbital sea-level cycles.

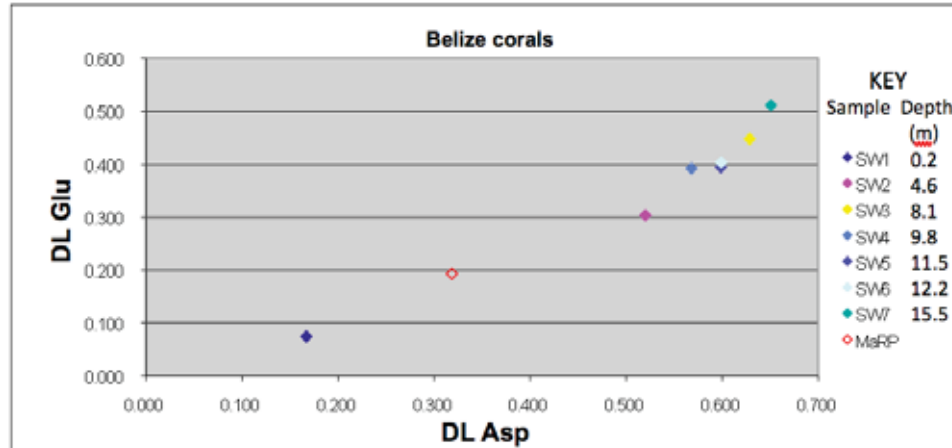


Figure 2: Amino Acid Racemization ratios (DL Asp and DL Glu) for Belize corals. Samples SW1-7 are from the Southwest Caye core. Sample MaRP is from the Reef Point outcrop in northern Belize.

Facies Heterogeneity

Several dominant corals and three facies are recognized in the Holocene of Glover's Reef: *Acropora palmata*, *Acropora cervicornis*, Brain coral (*Diploria*, *Colpophyllia*), Star coral (*Montastraea*, *Siderastrea*, *Dichocoenia*), unconsolidated sand and rubble, well-cemented grain-rudstone, and crustose coralline algae (CCA) and foraminiferan boundstones. The physical and the biological interact on Glover's Reef to create facies heterogeneity. Higher wave energy and water agitation leads to more prevalent *Acropora palmata*, CCA boundstones, and well-cemented Holocene grainstones on the windward versus the leeward side of the platform (Figure 3). On the leeward side of the platform, a paucity of these same facies characterizes core GR2. This core not only lacks the facies common to fully aggraded reefs, with the Pleistocene top at 11.5 mbsl, it also has significantly less inherited topography.

Pleistocene facies include head coral framestone, branching coral grainstone, *Acropora palmata* grainstone, mollusk-*Halimeda* wackestone, coral and shell rubble, and platy coral framestone. This last facies is found only below 13 mbsl in the cayes and consists of plates of bifacial *Agaricia* coral encrusted with CCA, foraminifera, and mollusks. Also found only in the cayes are *Acropora palmata* grainstones, a facies dominated by large pieces of CCA encrusted *A. palmata* that is thought to represent the reef crest environment. Mollusk-*Halimeda* wackestones and coral and shell rubble facies are found only in the patch reef cores (GR3, Oreaster, and Aurelia). In contrast to the margin cores, which contain species and diversity levels indicative of open marine conditions and high energy, patch reef cores display the cyclic patterns, muddier textures, and lower species diversity that are indicative of restricted conditions. While accommodation space is always plentiful on the platform margin, reef growth on the

margin can reduce wave and current energy reaching the interior. Patch reef facies also align with Wallace's (1975) ecological zonation of the lagoon, but the persistence of ecological patterns into the Pleistocene suggest that his explanation of disturbance succession is insufficient.

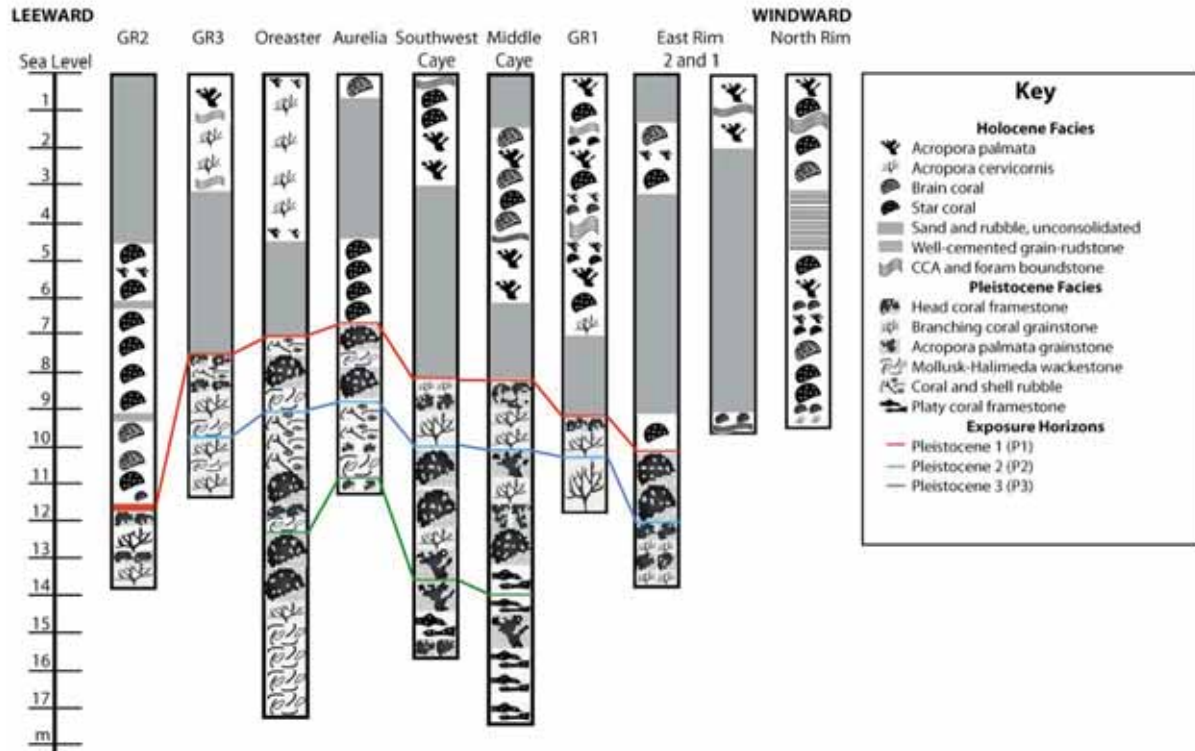


Figure 3: Holocene and Pleistocene facies of Glover's Reef. See Figure 1 for core locations. Windward cores contain more *Acropora palmata*, boundstones, and well-cemented Holocene grainstones than leeward cores. Patch reef cores display shallowing upward cycles. Pleistocene facies of GR2 suggest that, like in the modern, the Pleistocene leeward reef never fully aggraded to sea level.

Early Diagenesis

Holocene Cements

Four cement morphologies are present in Holocene sections of the cores: 1) acicular, 2) botryoidal, 3) microcrystalline, and 4) isopachous, bladed fringe cement (Figure 4). Isopachous, bladed fringe cements are found only in grain-rudstone facies of the most windward core site (North Rim). The other cement morphologies are present at both windward and patch reef cores sites. They are associated with coral, crustose coralline algae (CCA), and encrusting foraminiferan boundstones. Although Gischler and Hudson (1998) report acicular Holocene cements only within the coral skeletal framework, we find it present within the internal pores of gastropods as well. Holocene cements are associated with >50% high magnesium calcite and isotopic values slightly heavier than un-cemented Holocene facies. Holocene cements are present in rocks from 0-10 m below sea level and between 3-7 kyr before present.

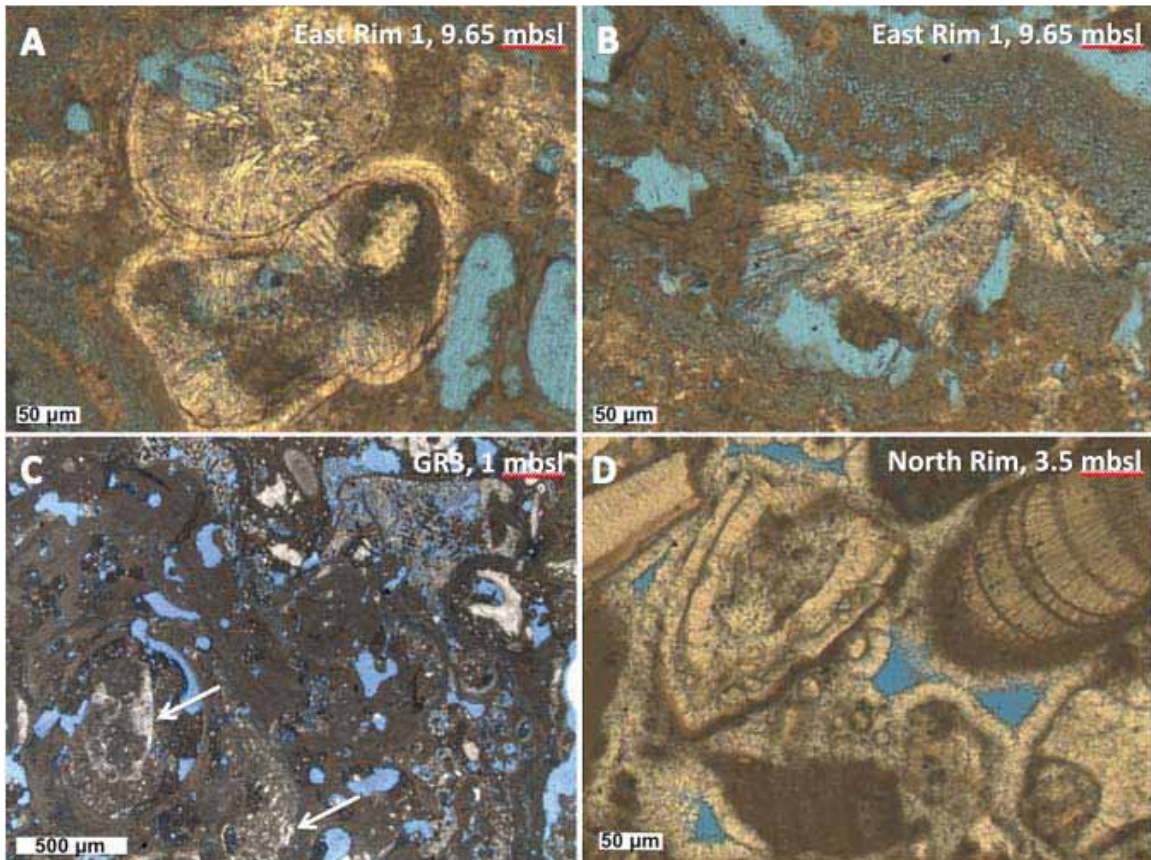


Figure 4: Holocene Cements. Clockwise from the left: Acicular cement within a gastropod cavity (East Rim, 9.65 mbsl), botryoidal cement associated with CCA (East Rim, 9.65 mbsl), microcrystalline cement in a CCA boundstone (GR3, 1 mbsl), and bladed, isopachous fringe cement in a skeletal grain-rudstone (North Rim, 3.5 mbsl).

Pleistocene Diagenetic Features

During the Last Glacial Period, large parts of the Pleistocene limestone of Glover's Reef were exposed and altered with meteoric waters, producing dissolution, caliche formation, root structures, re-crystallization of grains and marine cements, and precipitation of blocky cements. Notably lacking in the Glover's Reef samples are meniscus cements. Aragonite grains are preferentially dissolved or re-crystallized. In the case of *Halimeda* grains, complete porosity inversion can occur in a relatively short amount of time as pores are first filled with cement and the grain is subsequently dissolved leaving only its "ghost" or micritic rim and cement-filled pores in the rock record (Figure 5). In a few rare instances; however, high aragonite (>80%) content is preserved in coral skeletons. The degree of preservation is exclusively associated with CCA and re-crystallized marine cements. This "shield" of metastable minerals preserves coral in a median stage of dissolution or re-crystallization. This stage presents as a friable chalk texture in hand sample, which we find below 13 mbsl in the Middle Caye, Southwest Caye, and Oreaster cores.

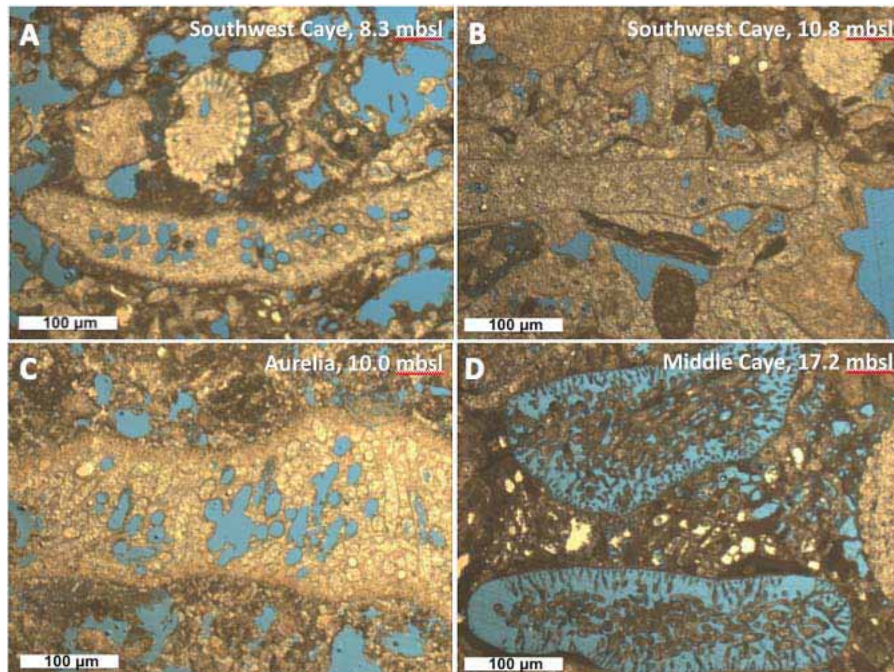


Figure 5: Diagenetic pathways of the green alga, *Halimeda*. A) *Halimeda* is re-crystallized with internal porosity preserved. B) Internal pores are filled with blocky cement and only the micritic rim denotes the presence of a *Halimeda* grain. C) Internal pores are filled with blocky cement while the grain is partially dissolved. D) Complete dissolution of the aragonite grain leads to an inversion of porosity and a *Halimeda* “ghost”.

References

- Blanchon, P., Eisenhauer, A., Fietzke, J., and Liebtrau, V., 2009. Rapid sea-level rise and reef back-stepping at the close of the last interglacial highstand. *Nature*, 458, 881-885.
- Farrell, J.W., Clemens, S.C., and Gromet, L., 1995. Improved chronostratigraphic reference curve of the late Neogene seawater $^{87}\text{Sr}/^{86}\text{Sr}$. *Geology*, 23, 403-406.
- Gischler, E., Ginsburg, R.N., Herrle, J.O., Sachindra, P., 2010. Mixed carbonates and siliciclastics in the Quaternary of southern Belize: Pleistocene turning points in reef development controlled by sea-level change. *Sedimentology*, 57(4), 1049-1068.
- Gischler, E., and Hudson, J.H., 1998. Holocene development of three isolated carbonate platforms, Belize, Central America. *Marine Geology*, 144, 333-347.
- Hearty, P.J., Hollin, J.T., Neumann, A.C., O’Leary, M.J., and McCulloch, M., 2007. Global sea-level fluctuations during the Last Interglaciation (MIS 5e). *Quaternary Science Reviews*, 26, 2090-2112.
- Miller, G.H. and Brigham-Grette, J., 1989. Amino Acid Geochronology: Resolution and precision in carbonate fossils. *Quaternary International*, 1, 111-128.
- Wallace, R.J., 1975. A reconnaissance of the sedimentology and ecology of Glovers Reef Atoll, Belize (British Honduras). Princeton University unpublished Ph.D. dissertation, *Geology*, 140 p.

Using Isotopic Tools to Understand Effects of Elevated Nutrient Levels on Scleractinian Corals

Quinn B. Devlin and Peter K. Swart

Key Findings

- Zooxanthellae utilize ambient DIN thereby reducing their dependency on nutrients translocated from the zooxanthellae
- The shift in the utilization of DIN also causes a reduction in the amount of carbon translocated from the corals to the zooxanthellae and may account for the reduction in coral growth in the presence of elevated nutrients

Introduction

Concern over the survival of coral reefs has prompted many studies on nutrient dynamics in healthy reef systems. Understanding the impact of anthropogenic activities on coral reefs is critical. In particular there is concern surrounding the impacts that excess nutrients have on reef biota since coral reefs thrive in oligotrophic waters.

The mechanism whereby nutrients positively or negatively impact coral growth is not certain, but may involve the symbiotic association between corals and zooxanthellae, a dinoflagellate algae. It is widely accepted that the zooxanthellae provide photosynthate to the coral (Muscatine et al., 1981; Swart et al., 2005), while the coral provides nitrogen to the zooxanthellae through waste excretions (Falkowski et al., 1993; Muscatine et al., 1978).

Nitrogen isotope tracer studies allow for the direct observation of transport, uptake, and assimilation by organisms. We have utilized methods of stable isotope geochemistry and nutrient analyses to monitor the uptake and assimilation of dissolved inorganic nitrogen (DIN: NH_4^+ and NO_3^-) added to experimental incubations of zooxanthellate corals. In addition, carbon isotope labels have been employed to investigate the response in carbon translocation between the zooxanthellae and coral host. The primary objectives of this study are 1) to develop a better understanding of $\delta^{15}\text{N}$ values of coral tissue and their symbiotic zooxanthellae associated with variable sources and concentrations of external DIN, and 2) to determine the impact of excess DIN on the coral-algal symbiotic relationship, coral growth, and ultimately mortality.

Methodology

Experiments were carried out in which specimens of cultured corals, *Montastraea faveolata*, *Acropora cervicornis*, and *Pocillopora damicornis* were grown in varying concentrations of NH_4^+ or NO_3^- . To assess the impact of DIN we looked at coral growth rates, zooxanthellae density and biogeochemical composition of the coral. To investigate dynamics in N and C cycling, we employed techniques of stable isotope geochemistry.

Corals were incubated indoors at the University of Miami's Experimental Hatchery. Light levels and temperature were maintained constant throughout the system. Nutrient manipulations were carried out in experimental aquaria. Levels of NO_3^- or NH_4^+ were

manipulated at various concentrations, together with a control maintained at ambient nitrogen levels over several weeks.

Data Analysis

The concentrations of NH_4^+ or NO_3^- were measured within the incubation water throughout several 24 hour time series experiments. Colorimetric analyses were carried out in house with a spectrophotometer. Weekly growth was measured with an optical micrometer (methods of Chris Langdon, University of Miami – RSMAS, Figure 1). Photography was used to supplement the micrometer data to obtain a more accurate measurement of lateral growth. The $\delta^{13}\text{C}$ & $\delta^{15}\text{N}$ compositions of coral and zooxanthellae tissue were measured on an ANCA GC-IRMS.

The $\delta^{15}\text{N}$ of NO_3^- and NH_4^+ in the incubated water will be determined using the method of McIlvin & Altabet (2005). Azide addition will be used to convert DIN to N_2O for analysis.

Initial Results/Implications

Zooxanthellae incorporate DIN from treatment additions and are thus N limited. As N is assimilated into the zooxanthellae, the lighter isotopes are preferentially taken up. We can assess the presence of N limitation through close examination of $\delta^{15}\text{N}$ present in the DIN and algal tissues. In the case of N limitation, the $\delta^{15}\text{N}$ is more enriched in the tissues because of less discrimination against ^{15}N (more incorporation of ^{15}N) due to lower ^{14}N availability. If nitrogen is not limiting, higher discrimination against ^{15}N will result in depleted tissues.

Increased ambient DIN may cause a shift in the N source for zooxanthellae. The NO_3^- or NH_4^+ rich waters may fully satisfy the N demands of the zooxanthellae. If the only benefit to the zooxanthellae from the coral-zooxanthellae symbiosis is a source of N from coral waste excretions, the symbiosis may be altered. Changes in growth rate and biochemical composition of the tissues may indicate that the energy relationship within the symbiosis has changed. Reduction in transfer of photosynthetic carbon from zooxanthellae to coral host may result.

The results of this study will establish values of $\delta^{15}\text{N}$ in coral tissues associated with variable sources and concentrations of DIN in reef habitats, which are not well understood. Impacts of DIN on the coral-algal symbiosis, coral growth and mortality will be assessed.

References

- Falkowski, P.G., Dubinsky, Z., Muscatine, L. and McClosky, L.R. 1993 Population control in symbiotic corals. *Bioscience* 43, 606–611.
- McIlvin M.R. and Altabet M.A. 2005 Chemical conversion of nitrate and nitrite to nitrous oxide for nitrogen and oxygen isotopic analysis in freshwater and seawater. *Analytical Chemistry* 77, 5589-5595.
- Muscatine L. and D'Elia C.F. 1978 The uptake, retention and release of ammonium by reef corals. *Limnology and Oceanography* 23:4, 725-734.
- Muscatine L., McCloskey L.R., and Marian R.E. 1981 Estimating the daily contribution of carbon from zooxanthellae to coral animal respiration. *Limnology and Oceanography* 26, 601.



Figure 1. Coral nubbins of Pocillopora damicornis growing on sled designed for measurement with optical micrometer.

Depositional Architecture, Hydrodynamics, and Morphometrics of Cold-Water Coral Mounds on the slope of Great Bahama Bank

Thiago B.S. Correa, Mark Grasmueck, Gregor P. Eberli, Klaas Verwer and Sam Purkis

Key Findings

- The slope of Great Bahama Bank (GBB) is a major cold-water coral mound province as shown by the average density of 14 mounds per km² for the three surveyed sites.
- Mound structures vary from circular to elongate in shape, and lack a preferred orientation, which contradicts the predictions of previous hydraulic-based models.
- Growth rate of the mounds compete with sedimentation rates; mounds can be buried or experience significant growth depending on the sedimentation rates.

Variability of cold-water coral mound morphologies in the Straits of Florida

Cold-water coral mounds are common features throughout the Florida-Bahamas-Hatteras region, where the strong Florida Current is hypothesized to be one of the main controlling forces on mound morphology and development (Mullins et al., 1981). This hypothesis is often supported by reports of streamlined mounds aligned parallel to the northerly current (Neumann et al., 1977). Recent studies, however, have documented variations in mound morphology associated with different current regimes in the Straits of Florida. Correa et al. (submitted), for example, identified a series of long and linear cold-water coral ridges along the base of the Miami Terrace that are oriented perpendicular to a southward flowing current. In contrast, a large cold-water coral mound field, characterized by variable mound shapes and a tidal current regime, was documented on the slope of Great Bahama Bank (GBB) (Grasmueck et al. (2006). To further explore the effect(s) of hydrodynamics on mound morphology, and to better understand the forces shaping mound fields in the Straits

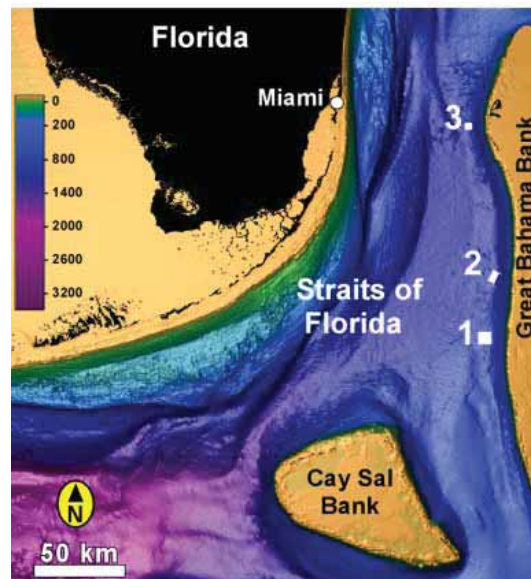


Figure 1: Bathymetric map with the location of the three surveyed sites (white boxes, drawn to scale) on the slope of the Great Bahama Bank (GBB). Base map compiled by Jiangan Luo.

of Florida, this study quantitatively analyzes a large geophysical and current dataset (~80 km² total) from three sites at the base of the western slope of GBB in water depths of 650 to 840 m (Figure 1). The dataset consists of multiple, simultaneously acquired parameters such as bathymetry, side-scan sonar, and bottom current, and was collected using an Autonomous Underwater Vehicle (AUV) that cruises at an altitude of 40 m above the seabed. The datasets have an unprecedented sub-meter resolution (i.e., 0.5 to 3m cell size).

Variability of currents in the three mound fields

The current at each site exhibits clear (albeit slightly different) bi-directional tendencies, which are generally north-south (Figure 2A). The north-south reversal time interval for the three sites is on average ~6 hrs, documenting an internal diurnal tidal current regime at the base of slope of western GBB. Within this general trend, however, currents flow from all other directions during the sampling period (Figure 2B).

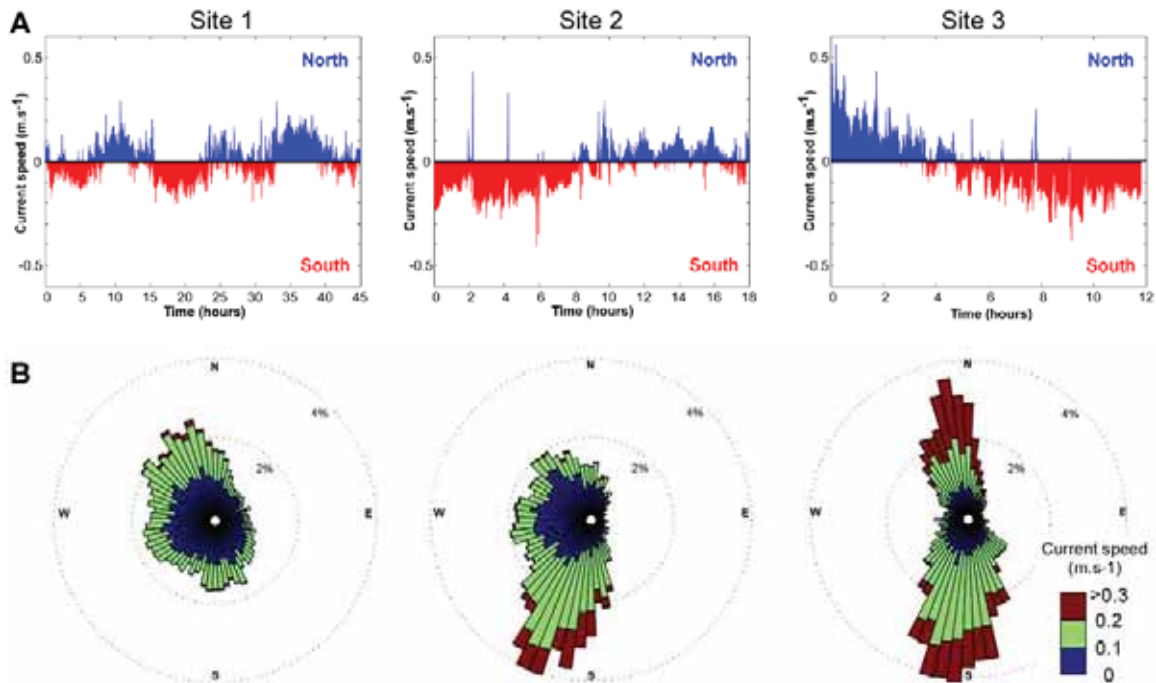


Figure 2: Plots summarizing current regime for the GBB sites. (A) North-south current velocity component (y-axis) vs elapsed survey time (x-axis at different scales) shows that the current reverses approximately every six hours, indicating tidal motion throughout the slope of Great Bahama Bank. (B) Rose diagrams show the relative frequencies of measured current vector directions (5° bin size) and velocities (colors) over the course of the site surveys.

Mound morphometrics

A total of 1095 mounds (a mound being feature at least 1 m in elevation) were extracted from the three sites, giving an average density of 14 mounds per km² on the slope of GBB (Figure 3A). All mounds were then quantitatively analyzed in terms of their area, height, shape, and orientation. Plotting exceedance probability versus mound base area produces a mound size-frequency distribution that is skewed towards smaller mounds (higher probability of occurrence in y-axis), especially at Site 1 (Figure 3A).

Mound base areas vary between 100 to 600,000 m² and are positively correlated with mound heights (1 to 83 m) (Figure 3B). This indicates that the highest mounds often have the largest footprint areas. The shape of a mound is not correlated with the area of its base (Figure 4A) and mounds do not become elongated as their footprint areas increase. Furthermore, a predominant mound orientation is not observed at any site (Figure 4B).

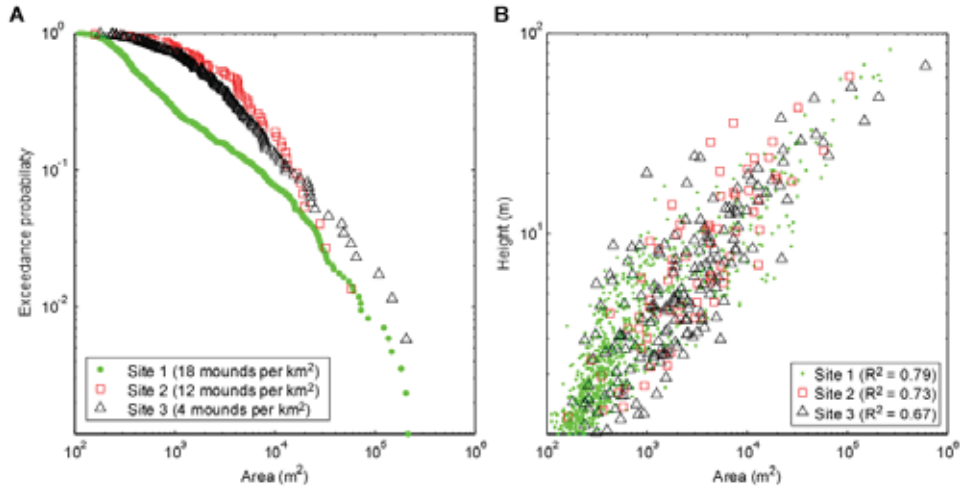


Figure 3: (A) Mound base area (x-axis) vs exceedance probability (y-axis) shows the probability that a given mound is equal to or greater than a given area. The more linear trend at Site 1 reflects the higher occurrence of smaller mounds, relative to Sites 2 and 3. (B) Plot of mound base area vs mound height shows that these parameters are strongly correlated at all sites.

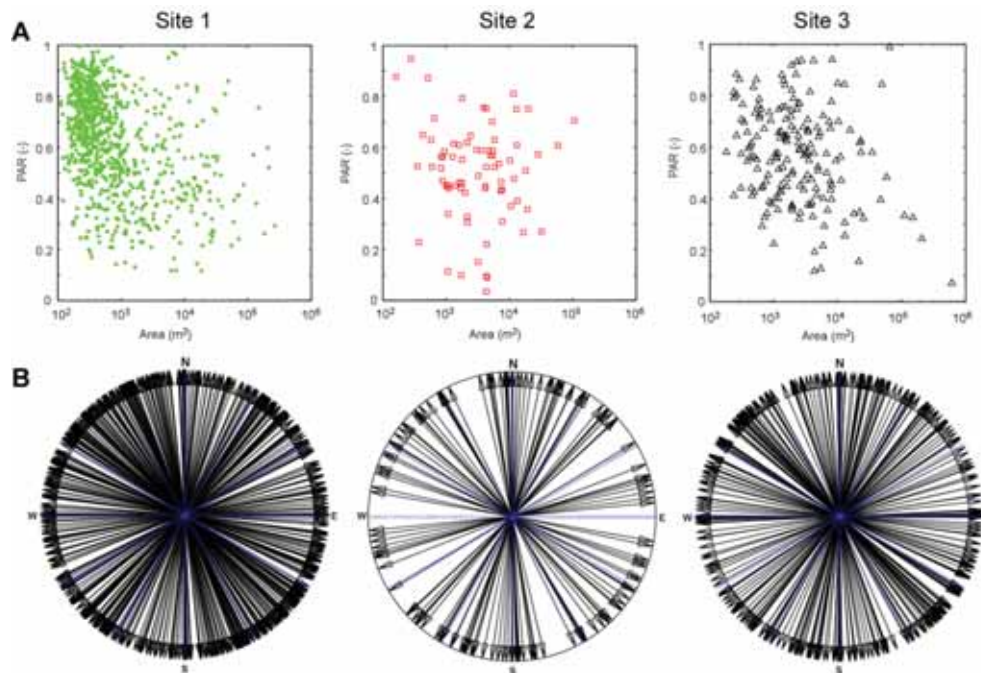


Figure 4: (A) Mound base area vs shape (Principal Axes Ratio, y-axis) for each site showing that mounds do not become elongated (values close to zero) as their footprints increase. (B) Black arrows record the azimuth of the principal axis of every mound. The mounds do not have a preferential orientation in any of the GBB sites.

The mound fields on the GBB slope experience variable (tidal) currents and display complex mound morphologies. In other fields in the Straits of Florida relationships between currents and mound morphology are simpler. For example, teardrop mound morphologies or long linear ridges have been described in unidirectional current regimes (Neumann et al., 1977; Correa et al., submitted). Along the western slope of GBB the complexity in current regime and the complexity in mound morphometrics are large and not well correlated. For example, the highest average mound density and the tallest individual mound are both in Site 1 where the current strength is the lowest (Figures 2 & 3). Yet, Site 1 also has the highest density of small mounds of any site (Figure 3A). Mound orientations are variable in all sites with no preferred alignment along the dominant north-south bottom current direction (Figures 2B, 4B). Therefore, it is hypothesized that a complex interplay of sedimentological, hydrological and biological processes is responsible for the observed variability in mound morphology and distribution at the GBB sites.

Hydrodynamic influence on mound morphology

Larval dispersal and bioerosion play a critical role in shaping cold-water coral mound structures, and likely contribute to the mound variation observed in the GBB fields. The variable current might export larvae in all directions from the top of the mound, thus contributing to complex mound morphologies. At broader spatial scales, mound structures represent natural obstacles for the bottom current. In developed mound fields like the GBB sites, the interaction of the current with sea bottom can produce scours and sediment tails that are attached to or surrounding mounds (Figure 5).

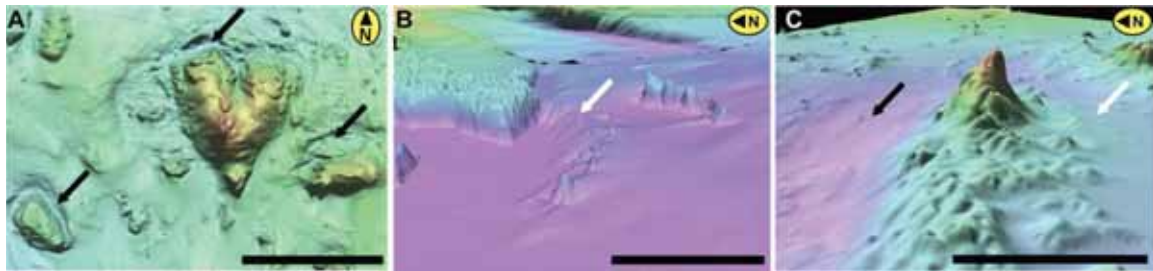


Figure 5: Close-up views of the bathymetric maps of each GBB site showing some of the main depositional features surrounding mounds, such as scours (black arrows) and sediment wedges (white arrows). (A) Scour around heart-shaped mound structure, Site 1. (B) Oblique view of the plateau area in Site 2 showing the sediment wedge that is partially burying small mounds beyond the plateau. (C) Oblique view of the pyramid-shaped Matterhorn mound in Site 3 with several smaller mounds attached in a linear orientation. A linear scour feature developed along the Matterhorn's northern side while sediment wedge onlaps its southern side. Scale bars are 500m.

These current-induced features, and the resulting shapes of the mounds, depend on the orientation of the original obstacle (i.e., mound) with respect to the current (Belderson et al., 1982). If mounds are all oriented in the same direction with respect to the current, similar seabed forms will likely develop (Belderson et al., 1982). However, because the GBB mounds are oriented in a variety of directions, seabed features are fairly diverse at the GBB sites. In addition, the bottom features can develop in both the ebb and flood directions (though usually not equally as shown by the north-pointing sediment streaks on

the backscatter amplitude maps). This contributes further complexity to mound morphologies (Figure 5).

Off-bank sedimentation influence on mound morphology and development

Sedimentation adds another complexity to the GBB study sites. Bank-derived sediments are transported downslope and form up to 90 m thick wedges on the western slope of GBB (Figure 6) (Hine et al., 1981; Wilber et al., 1990). Ocean currents subsequently redeposit some of the bank-derived sediments (Anselmetti et al., 2000). Both the slope deposits and the drift deposits influence mound development by: (1) homogenizing mound perimeters and/or (2) entirely smothering mound structures. For example, at the most upslope site (Site 2) slope deposits partly bury some mounds, especially the small mound structures beyond the topographic highs (Figure 5b). Thus the relatively high sedimentation at Site 2 likely contributes to the flat and smooth depositional architecture and the low average density of exposed mounds (4 mounds/km²). In contrast, the high average mound densities at Sites 1 and 3 (18 and 12 mounds/km², respectively), together with the more irregular depositional architecture characterized by scours and sediment tails (Figure 5), suggest a moderate sedimentation rate at these more basinward sites (Figure 6).

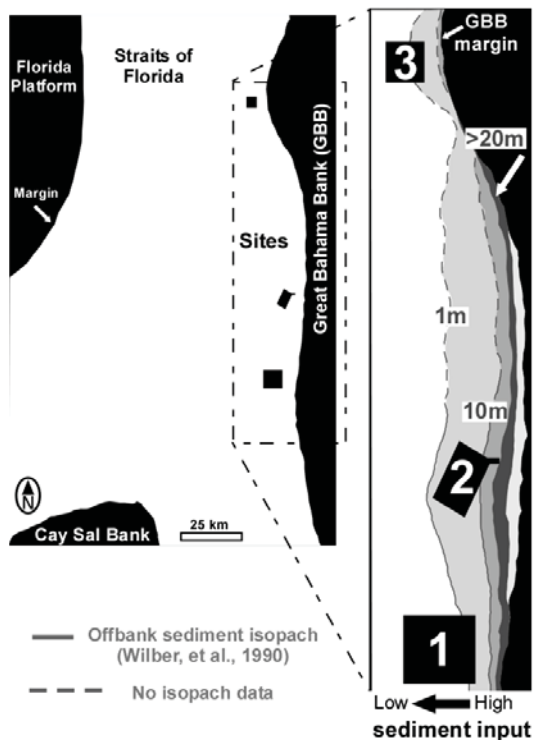


Figure 6: Schematic diagram showing the locations of Sites 1-3 with respect to offbank sediment deposits mapped by Wilber et al. (1990). Site 2 is located within the 1 to 10 m isopach, while most of Site 1 is positioned basinward of the 1m isopach. Although isopach data are not available for Site 3, based on the observed abrupt change in terrain moving basinward, this site is interpreted as crossing the 1m isopach on its upslope side.

Sites 1 and 3 further downslope receive less offbank sediment and may therefore constitute 'optimal' areas for mound development. The relatively high mound densities at these sites (especially at Site 1) suggest that mound growth outpaces sedimentation. Small mounds in these areas are able to avoid burial and eventually develop into large structures. The additional (moderate) source of offbank material, in combination with a

relatively variable current regime (e.g., bidirectional tidal, which can potentially increase bottom turbidity) is interpreted as beneficial to mound growth.

This study reveals that the GBB sites have complex architectural slopes and are part of a major cold-water coral mound province. Morphometric analyses show that mounds vary significantly in area, height, shape and orientation. Although current regime has been implicated as a main controlling factor of cold-water coral mound fields, neither current strength nor direction appear to dictate mound features in the GBB. Instead, a combination of bottom current and sedimentary regimes, both of which vary across the GBB, is hypothesized to drive the observed heterogeneity in mound parameters. Future work on other producing carbonate platform slopes is necessary to determine whether the environmental conditions and cold-water coral mound field characteristics observed here are unique to the GBB leeward slope or are common to all producing banks.

References

- Anselmetti, F.S., Eberli, G.P. and Ding, Z.D., 2000. From the Great Bahama Bank into the Straits of Florida: A margin architecture controlled by sea-level fluctuations and ocean currents. *Geological Society of America Bulletin*, 112(6): 829-844.
- Belderson, R.H., Johnson, M.A. and Kenyon, N.H., 1982. Bedforms. In: S. A.H. (Editor), *Offshore Tidal Sands. processes and Deposits*. Chapman and Hall, London.
- Correa, T., Grasmueck, M., Eberli, G. and Viggiano, D., 2009. Morphometric Analyses and Habitat Characterization of Deep-Water Carbonate Mounds in the Straits of Florida, CSL Annual Meeting, University of Miami.
- Correa, T.B.S. et al., submitted. Quantitative habitat characterization of cold-water coral ridges at the Straits of Florida. *Geology*.
- Grasmueck, M. et al., 2006. Autonomous underwater vehicle (AUV) mapping reveals coral mound distribution, morphology, and oceanography in deep water of the Straits of Florida. *Geophysical Research Letters*, 33(23).
- Hine, A.C., Wilber, R.J., Bane, J.M., Neumann, A.C. and Lorenson, K.R., 1981. Offbank transport of carbonate sands along open, leeward bank margins: Northern Bahamas. *Marine Geology*, 42: 327-348.
- Mullins, H.T., Newton, C.R., Heath, K. and Vanburen, H.M., 1981. Modern Deep-Water Coral Mounds North of Little Bahama Bank - Criteria for Recognition of Deep-Water Coral Bioherms in the Rock Record. *Journal of Sedimentary Petrology*, 51(3): 999-1013.
- Neumann, A.C., Kofoed, J.W. and Keller, G.H., 1977. Lithoherms in Straits of Florida. *Geology*, 5(1): 4-10.
- Wilber, R.J., Milliman, J.D. and Halley, R.B., 1990. Accumulation of bank-top sediment on the western slope of Great Bahama Bank: Rapid progradation of a carbonate megabank. *Geology*, 18: 970-974.

Revisiting Reciprocal Sedimentation in Mixed Systems

Gregor P. Eberli and Michael Zeller

Key Points

- In response to sea level the mixing of carbonates and siliciclastics is not as simple as highstand = carbonates and lowstand = clastics
- On shelves where carbonates and clastics coexist, increased siliciclastic sedimentation occurs during rapid sea level rise because of the combined effect climate change and ravinement erosion
- Longshore currents are a major factor in distributing clastics equally along the basin margins

The Concept Of Reciprocal Sedimentation

Sequence stratigraphic models describe the sedimentary response to sea level in both the siliciclastic and the carbonate systems (e.g. Posamentier et al. 1988; Sarg 1988). In mixed systems the classic model explains changes from siliciclastics to carbonates by reciprocal sedimentation where carbonates are deposited mainly during sea level highstand and siliciclastics during sea level lowstands (Wilson 1967). This concept of reciprocal sedimentation gained more credibility, becoming a paradigm, with the documentation of high rates of sediment production and offbank transport during the Holocene sea-level rise and highstand (e.g. Haak and Schlager, 1989). This highstand shedding seems to place the carbonate environment 180° out of

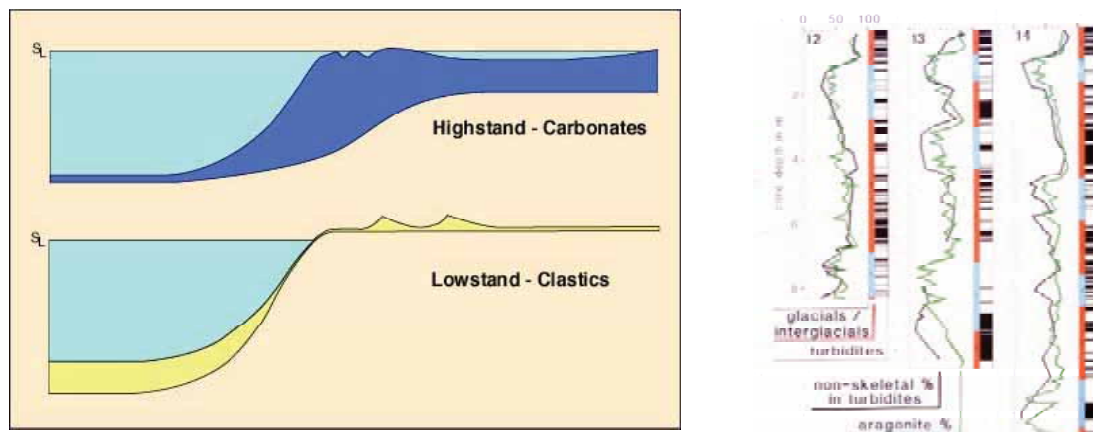


Figure 1: Left: The concept of reciprocal sedimentation proposes that carbonates are deposited mainly during sea level highstand and siliciclastics during sea level lowstands (figure from Scholle website). Right: Turbidite frequency and aragonite content during glacial interglacial periods in the Bahamas confirm that in carbonates turbidite export is mainly during sea level highstands (Haak and Schlager, 1989).

phase with siliciclastic systems where sediment is stored on the inner shelf during high sea level and transported into basinal areas during low sea level. This concept is applied in the sequence stratigraphic models. In siliciclastics environments, turbidite deposition either as basin floor fan or slope fan are a characteristic of the lowstand systems tract. In carbonate sequence stratigraphic models turbidite fans are minor component in some models (Handford and Loucks, 1993) and completely absent in others (Schlager, 2005). Other studies suggested a similar pattern of redeposition in carbonate and siliciclastic environments with maximum development of basinal onlap packages during sea level lowstands (Shanmugan and Maiola, 1983; Sarg, 1988).

Well-documented modern and ancient mixed carbonate-siliciclastic systems question the concept of reciprocal sedimentation. These case studies require revisiting the concept and the notion that carbonates are 180° out of phase with siliciclastics.

The Australian Shelf

The modern Great Barrier Reef is situated on rimmed clastic-carbonate shelf. During the current sea level highstand the clastics are confined to the shoreline, while the barrier reef is flourishing on the shelf edge. The shelf was largely exposed during the last glacial maximum and during this period of lowered base level the rivers cut across the shelf and are refilled during the subsequent transgression (Fielding et al. 2005). In cores from the offshore area, mass accumulation rates of both carbonates and siliciclastics are increased during the Holocene transgression (Figure 2; Page and Dickens, 2005). This sedimentation pattern is not compatible with the concept of reciprocal sedimentation.

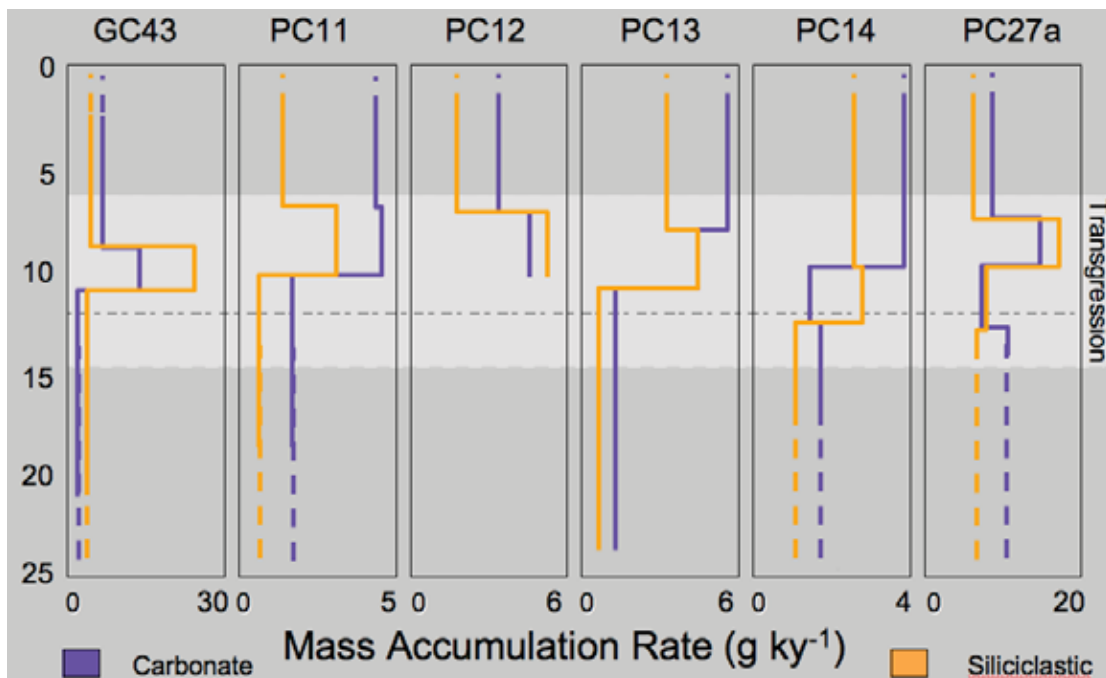


Figure 2: Mass accumulation rates of siliciclastics and carbonates in cores offshore the Great Barrier Reef in Australia. The accumulation is increased in both system, questioning the concept of reciprocal sedimentation (Page and Dickens, 2005).

The Alberta Shelf during the Devonian

On the Alberta shelf, where isolated carbonate buildups coexist with basinal shales, Stoakes (1980) proposed that basinal shale sedimentation is interrupted by rapid sea level rises; during these times carbonate production is dominant. Such a clear reciprocal sedimentation can not be documented in the outcrop. In outcrop, the basinal shales onlap the buildups and are interfingering with platform-shed carbonates. In contrast to Stoakes's assumption, carbonate production is not continuous but also is pulsed. Redeposited carbonates are shed during sea level lowstands while a halo of periplatform carbonates is shed into the adjacent basin during sea level highstands. In addition, maximum shale deposition occurs during the transgressive systems tracts of both 3rd and 2nd order depositional sequences (Figure 3).

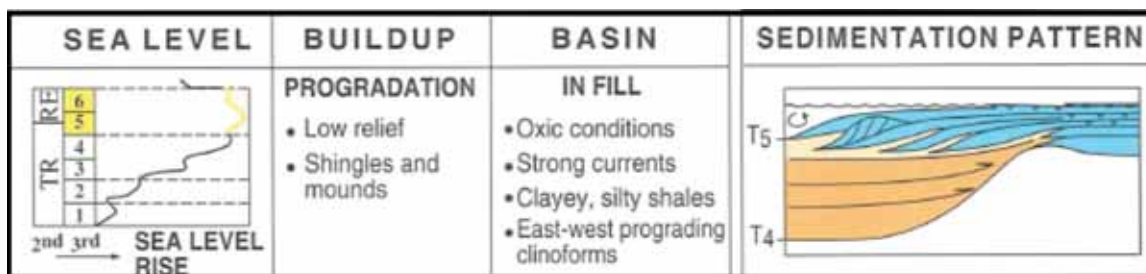


Figure 3: Schematic display of the carbonate platform and siliciclastic (shale) basin fill in response to 2nd order sea level cycle on the Alberta shelf during the Frasnian (modified from van Buchem et al, 2000). Note that the thickest shale accumulation occurs during rapid sea level rise that causes the platform margin to backstep.

The Upper-Jurassic - Lower-Cretaceous Formations in the Neuquén Basin

The Quintuco - Vaca Muerta System in the Neuquén Basin in Argentina is a mixed carbonate siliciclastic system with a high degree of lateral and vertical heterogeneities. Seismic data imaging the Quintuco Formation in the Loma La Lata Field and outcrops of the time-equivalent Picún Leufú Formation in the southern Neuquén Basin both document a lower prograding unit dominantly composed of siliciclastics with upwards-increasing carbonate content. An aggrading middle unit can be subdivided into a lower siliciclastic dominated interval capped by a clean carbonate package, which in turn is overlain by an aggrading upper unit in which siltstones, and sandstones alternate with minor carbonates. In each unit, transitions between siliciclastic and carbonate sedimentation occur rapidly at every scale. At a meter scale clastic sandstones alternate rapidly with clean ooid-skeletal grainstones while on a decameter scale siliciclastic silt- and sandstone dominated packages alternate with pure carbonate intervals. The rapid transitions between siliciclastic and carbonate sedimentation are largely controlled by the available accommodation space on the shelf. High accommodation allows the development of strong longshore currents, which can carry sand and silt material for hundreds of kilometers and thereby turn off the carbonate factory on the shelf. During times of low accommodation, the current cannot reach the shelf environment and high carbonate production leads to mixed and pure carbonate deposits.

Longshore Current Transport of Siliciclastic Sediments

A process that is often underestimated in the mixing of the carbonate and siliciclastic systems is current transport of siliciclastics into the carbonate environment. The current transport occurs both in the shallow and deep-water realm. In the shallow-water coastal long shore transport are efficient in bringing coarse clastics onto the carbonate environment. In the deeper water longshore currents along the slopes and basin floor achieve transport and deposition of clay-sized particles from terrigenous clastic systems, such as deltas. Such longshore currents are caused by either wind-driven water circulation, the gyre in a basin, or tidal waves interacting on a basin scale. Modern examples of these persistent longshore currents are observed in the lakes (e.g. Lake Cardiel in Argentina), the Adriatic Sea and the in the modern mixed system of the Arabian Gulf and the north-eastern coast of South America. In these systems longshore currents distribute fine particles from estuaries along the shores as parallel bars sometimes over hundreds of kilometers. In the ancient, this process is recorded in shore-parallel clinoforms with fines preferentially accumulating in the bottomset, as is observed in the prograding clinoforms in the Cretaceous Bab Basin. In the mixed clinoforms of the Bab Basin, the interaction between these currents and the fluctuating sea level adds to the variable input, transport and deposition of clay-sized particles and the increased carbonate production during sea level rise and highstands.

References

- Fielding, C.R., Trueman, J.D. , Dickens, G.R. and Page, M., 2005, Response of a major river system to the last glacial cycle: geomorphology and internal architecture of the ancestral Burdekin River across the Great Barrier Reef shelf, northeast Australia. IAS Special Publication 35, p. 321-347.
- Haak, A.B. and Schlager, W. (1989). Compositional variations in calciturbidites due to sea-level fluctuations, late Quaternary, Bahamas: *Geologische Rundschau*, v.78, p. 477-486.
- Handford, C.R. and Loucks, R.G., 1993, Carbonate depositional sequences and systems tracts – responses of carbonate platforms to relative sea level. In: Loucks, R.G. and Handford, R.G., (eds.). *Carbonate Sequence Stratigraphy*. AAPG Memoir 57, p. 3-31.
- Page, M.C. and Dickens, G.R., 2005, Sediment fluxes through the Last Glacial cycle in the southern Great Barrier Reef Province, Marion Plateau: new constraints on 'transgressive-shedding' on the northeast Australian margin. *Marine Geology*, v. 219, p. 27-45.
- Posamentier, H. W., M. T. Jervy, and P. R. Vail, 1988, Eustatic controls on clastic deposition I - conceptual framework. *SEPM, Special Publication No. 42*, p. 109-124.
- Sarg, J.F., 1988, *Carbonate Sequence Stratigraphy*. *SEPM Special Publication 42*, p. 155-181.
- Schlager, W. 2005, *Carbonate Sedimentology and Sequence Stratigraphy*. *SEPM Concepts in Sedimentology and Paleontology #8*, pp.200.
- Shanmugam, G. and Muiola, R.J., 1984, Eustatic control of calciclastic turbidites. *Marine Geology* v. 56, p. 273-278.
- Stoakes, F.A., 1980, Nature and control of shale basin fill and its effect on reef growth and termination: Upper Devonian Duvernay and Ireton Formations of Alberta, Canada. *Bulletin of Canadian Petroleum Geology*, v. 28, p. 345-410.
- Wilson, J.L., 1967, Cyclic and reciprocal sedimentation in Virgilian strata of southern New Mexico. *Geological Society of America Bulletin*, v. 78, p. 805-818.

No Need for Fractures – the Matrix Dual-Porosity System of the Upper Quintuco in the Neuquén Basin, Argentina

Michael Zeller, Guillermina Sagasti Crippa¹, Maria A. Celentano¹, Pablo A. Crespo¹, Anthony R. Thompson¹, Jose Luis Massafiero¹, Klaas Verwer, Gregor P. Eberli

¹ REPSOL –YPF, Buenos Aires, Argentina

Key Findings

- In a large field in the Neuquén Basin production is from a heterogeneous mixed carbonate siliciclastic system (Upper Quintuco Formation).
- Production profiles point to a dual porosity system that is commonly interpreted as being controlled by carbonate fracture systems. However, neither faults (seismic data) nor fractures (cores) are observed at any scale.
- A new approach to high resolution modeling with alternative definition of net-to-gross and porosity-permeability relationships is capable of explaining dual-porosity reservoir behavior without a pervasive fracture network.

Motivation

Typical production profiles from a reservoir in the mixed carbonate siliciclastic Quintuco Formation in the Neuquén Basin (Argentina) show variable high initial rates, which drop very rapidly to long-term sustained low rates. This production behavior was hitherto interpreted as being controlled by fractures in the carbonate reservoir. However, faults, fractures or microfractures are not visible in seismic or core data. Moreover pressure data indicate reservoir overpressure, which could not be sustained over decades in a fully communicating fractured reservoir. In order to solve these discrepancies and find an adequate alternative explanation for the reservoir behavior a detailed static reservoir model is built, which can be tested by simulation runs.

Background

The Quintuco-Vaca-Muerta System in the Neuquén Basin

The Neuquén Basin in western Argentina is triangular shaped and surrounded by the Andes to the West, the Sierra Pintada System to the Northeast and the North Patagonian Massif to the South (Figure 1). During the time of Quintuco deposition (Tithonian – earliest Valanginian) the Neuquén Basin was under back-arc extension and the study area had a paleogeographic setting on a shallow, gently inclined shelf. The Vaca Muerta Formation are the basinal shales downslope of the shelf deposits of the Quintuco Formation, which explains the diachronous character of their contact, that is, getting younger towards the basin center (Figure 2).

The producing field is located in the eastern center of the Neuquén Basin and the area of interest has an extent of approximately 20x40 km (Figure 1). Being one of the classical hydrocarbon fields in the area, the field has been perforated by more than 400 wells, of which around 150 were targeting the Upper Quintuco Formation and the rest mainly targeting the underlying Sierras Blancas (Tordillo) Formation.

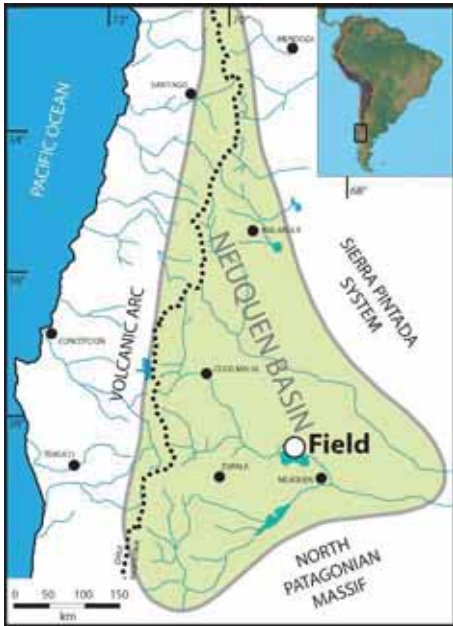


Figure 1: Map of the Neuquén Basin with location of the investigated oil field (after Howell et al. 2002)

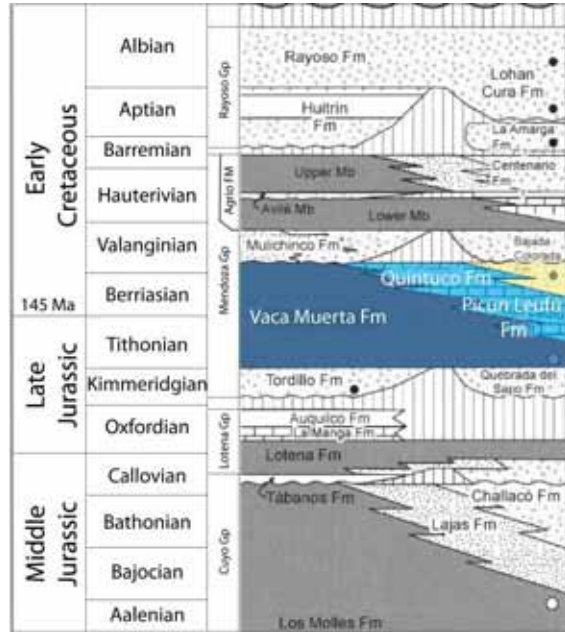


Figure 2: Stratigraphy of the Middle Jurassic to Early Cretaceous deposits in the Neuquén Basin (after Howell et al. 2002). Main production in the field is from the Quintuco and Tordillo formations

Challenges

Explanation of Production Profiles

The typical production profiles from the Upper Quintuco Formation show a high initial production from strata with low matrix porosity and maximum measured permeability of ~10mD. Thus, the profiles point to a dual porosity system of matrix and fracture porosity, although no indications of a pervasive fault, fracture or microfracture system can be found.

Petrophysical Characterization

The rapidly alternating nature of the mixed carbonate siliciclastic system in combination with the multitude of different well log suites complicates adequate petrophysical characterization and creates uncertainties in the available reservoir parameters (Vshale, porosity, water saturation etc.). Moreover core information is restricted to only a few stratigraphic intervals and therefore does not allow detailed facies modeling over larger areas in the field.

Production Allocation

Since most of the wells are perforated in several depths or are open hole and no production logging was carried out, allocation of actually producing intervals is virtually impossible. However in all described cores, porosity and oil stain can be found in clean ooid skeletal grainstones, which are stratigraphically positioned in regressive cycle tops.

Modeling Workflow

Due to these uncertainties it is necessary to develop a workflow to generate a geologically detailed static reservoir model of the highly variable system, which can be tested by history matching in simulation runs. The modeling workflow can be subdivided into 3 main steps (Figure 3):

Framework

Key for any further reservoir modeling is the creation of a reliable geological framework, which is based on the stratigraphic subdivision into zones. This is achieved by well log correlation oriented along depth converted seismic reflections (Figure 3). The resulting stratigraphic well tops (>3700 points) are used for zonation of the model, where layering is adjusted to well log resolution scale in order to preserve all information for the initial geological model.

Attribute Population

Seismic time slices are analyzed and interpreted for different zones in order to obtain orientation and extent data for different zones within the model. The resulting trends are used to populate the petrophysical parameters (Vshale, porosity) over the entire model and thereby create a high resolution reservoir model, which now can be used to calculate further petrophysical parameters.

Input for Reservoir Modeling

Due to the uncertainties in reservoir allocation and petrophysical characterization of the system, net to gross definition can not be as straight forward as in conventional fields. In order to account for these uncertainties a probabilistic approach to net-to-gross was developed. In this approach both Vshale and porosity values are evaluated and given a probability of reservoir potential. The resulting probabilities are multiplied, and produce the final model net-to-gross value for each cell.

Water saturation is based on measured values and a function of porosity, with lower porosity containing more water than higher porosities.

Porosity-permeability relationships are always one of the crucial parameters in carbonate and especially mixed carbonate siliciclastic systems. Initial simulation runs indicate that the measured maximum of 10mD in the highest porosity plugs is insufficient to explain the high production rates. However re-evaluation of measured plugs and thin sections show centimeter scale variations of high and low permeability (Figure 4), where the low viscosity oil in the over-pressured reservoir would ignore low permeability portions and just follow the high permeability flow paths. These small-scale variations can be observed in all wells within the oil stained grainstone intervals. Therefore plug measurements, which integrate low and high permeability, underestimate the effective permeability in the reservoir. As a consequence of these observations cells with higher porosity values are assigned higher permeability values than the actual porosity permeability relations indicate. This behavior would also explain the observed production

profiles with primary high production from the high porosity-permeability layers, which get slowly refilled in the secondary slow production phase.

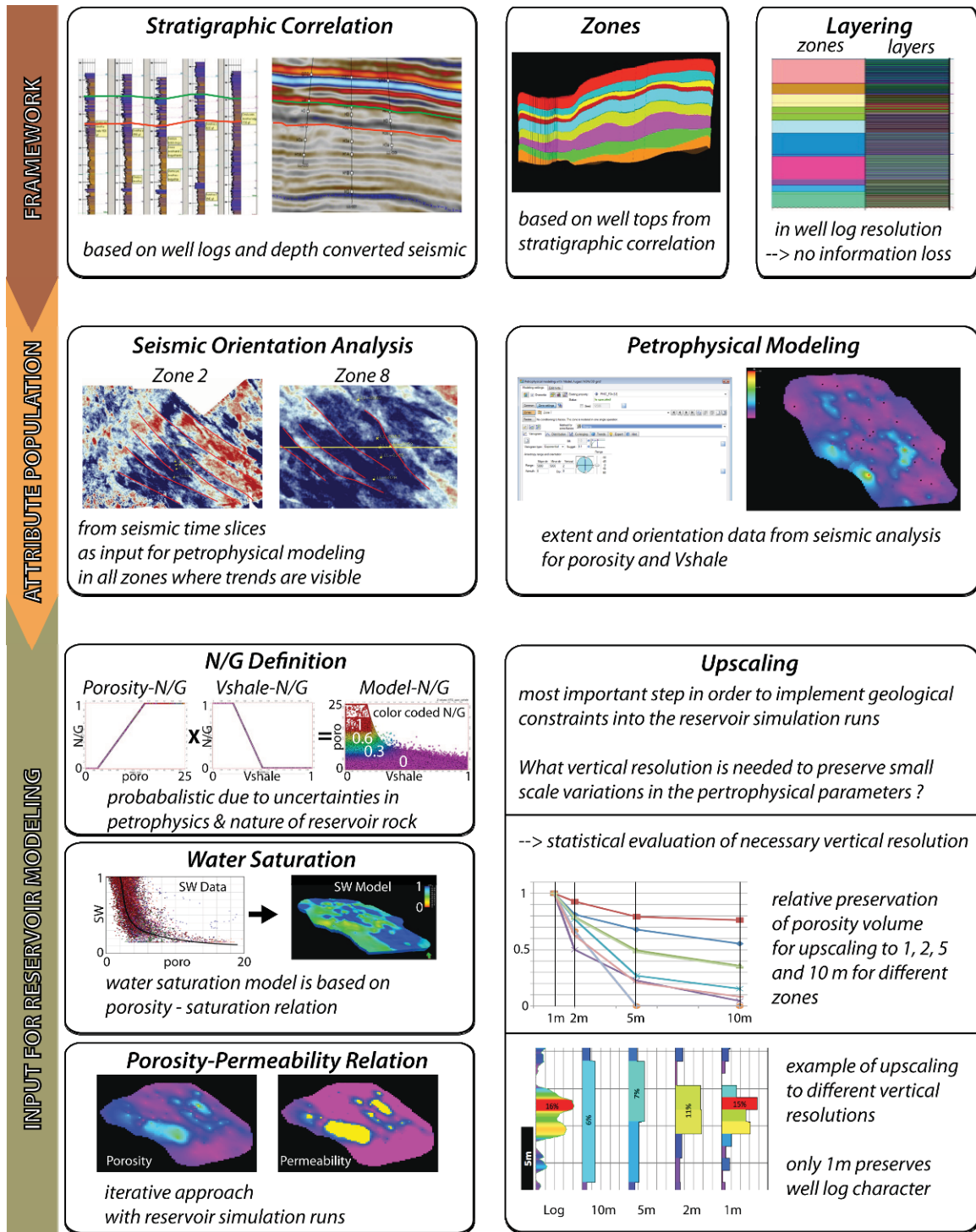


Figure 3: Reservoir Modeling Workflow composed of framework (correlation, zonation and layering), attribute population (seismic analysis, petrophysical modeling) and reservoir engineering input (N/G, Sw, Poro-Perm and Upscaling)

Upscaling is one of the most crucial steps in order to implement geological observations into the reservoir engineering simulation runs. In order to evaluate the optimum vertical resolution, the model was tested with 4 different average cell thicknesses (1,2,5 and 10 m). The resulting grids were analyzed in terms of preserved higher porosity cells (>6%) and preserved maximum porosity (Figure 3). In the investigated field, the rapid variations within the mixed carbonate siliciclastic system require an average vertical resolution of 1m.

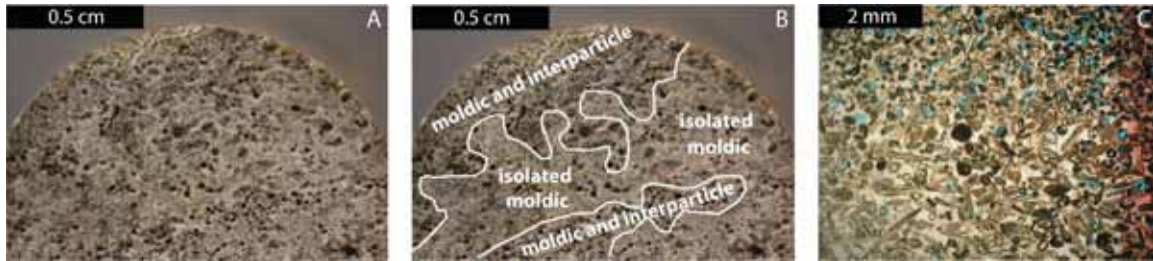


Figure 4: Example of cm scale porosity-permeability variations: A) plug photograph B) plug photograph with zones of high and low permeability C) photomicrograph of the same plug showing permeability alternations in mm scale

Modeling Results

Using the described modeling workflow a high-resolution geological and porosity model is generated (Figure 5A), which now can be used in order to evaluate reservoir potential of the Upper Quintuco field. For example, connected volumes can be extracted based on a porosity threshold and a minimum economic size (Figure 5B). These volumes are checked with historical production data from perforating wells and thereby can be evaluated in terms of remaining reservoir potential for new wells and secondary production.

Due to the high vertical resolution necessary to capture the small-scale variations within the Upper Quintuco, the full field model is not viable to be simulated by reservoir engineering software. Therefore the field is subdivided into sector models (Figure 5D). The main production area of the investigated field is extracted using the connected volumes as guides for the sector model outline (Figure 5C). which does not cut across potential communicating reservoir units.

The final simulation runs based on the sector model demonstrate a very close history match with only small discrepancies. Maximum permeability values necessary for this result are with 25 mD in the same order of magnitude as the observed 10 mD measurements.

Conclusion

With the new modeling approach and the redefinition of net-to-gross and porosity-permeability relationships it has been demonstrated that in contrast to the initial fracture reservoir interpretation an alternative matrix dual porosity system is capable of

explaining the observed historical production profiles. A pervasive fracture network, which is not observed, is therefore not necessary.

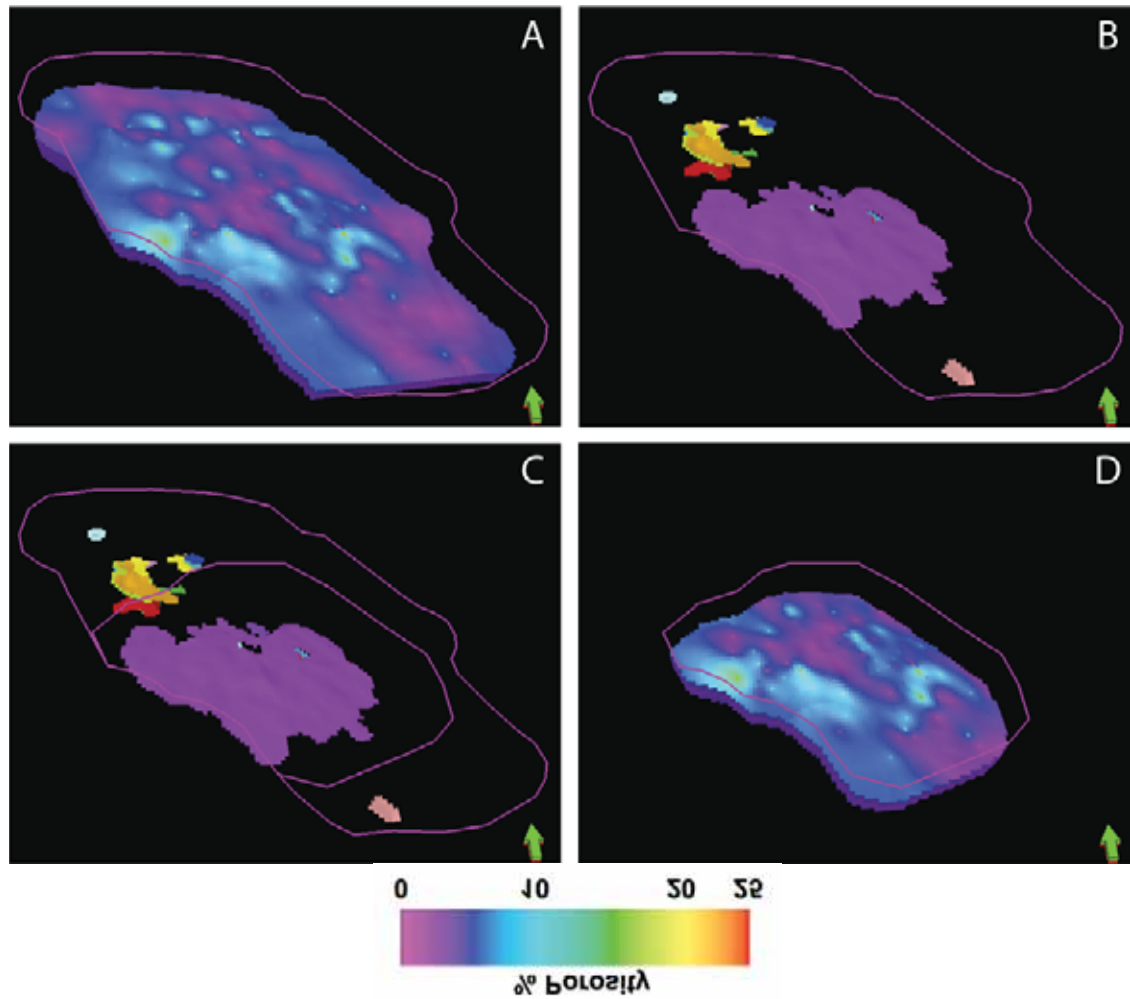


Figure 5: A: Full field porosity model B: Extracted connected volumes >7% porosity C: Extracted connected volumes with sector model boundary. D: New extracted sector porosity of main producing area of the field.

Reference

Howell, J.A., Schwarz, E., Spalletti, L.A. and Veiga, G.D., 2005. The Neuquén Basin: an overview, in: Veiga, G.D., Spalletti, L.A., Howell, J.A. and Schwarz, E., editors, 2005, The Neuquén Basin, Argentina: A case study in sequence stratigraphy and basin dynamics, Geological Society, London, Special Publications 252, 1-14.

Computational modeling of carbon dioxide sequestration in saline reservoirs

Caitlin M. Augustin, Peter K. Swart, Timothy H. Dixon

Key Points

- In order to realize the potential of geological CO₂ sequestration, it is essential to understand the behavior of the carbon dioxide plume, the injection aquifer, and the reservoir seal.
- There are three major outcomes of CO₂ sequestration in reservoirs
 - Deformation, fracture and leakage on the surface
 - Viscous fingering and negative downward migration
 - Stable sequestration within reservoir (no leakage, no migration)

Introduction

When CO₂ is injected into the pore space of a reservoir, reactions with the formation waters can lead to a water that is weakly acidic, but potentially reactive depending on the other constituents of the pore waters and the contacting rock minerals—leading to either carbonate precipitates or the fluid migration of the CO₂ plume (Johnson et al, 2000) . In hydrocarbon fields, it is known that the total stresses can change during this fluid-pressure depletion. However, it is not yet understood whether fluid injection will have a significant effect on total stresses in a reservoir scale sequestration. In order to understand the relationship between the injected carbon dioxide and key reservoir formation characteristics it is vital to accurately model the sequestration environment. We have hypothesized that the ground deformation signal is a key component in modeling both the geochemical and geophysical reactions.

By using data specific to the Farnham Dome Utah injection site (McPherson, 2009), we seek to understand the influence of micro-level reactions (grain/pore level) on the macro-level reservoir system. Through the use of discrete event modeling methods and geochemical computational software such as the Geochemist's Workbench, TOUGH, and NUFT/XTools we will approximate maximum sustainable pore-fluid pressures for injection sites by incorporating poroelastic behavior of reservoir rock into our dataset (Ehlig-Economides, C., Economides, M. 2009).

References

- Johnson, J.W., et al. 2000. Reactive transport modeling of geologic CO₂ sequestration in saline aquifers: the influence of intra-aquifer shales and the relative effectiveness of structural, solubility, and mineral trapping during prograde and retrograde sequestration. DOE
http://www.netl.doe.gov/publications/proceedings/01/carbon_seq/P28.pdf.
- McPherson, B. 2009. Factsheet for Southwest Partnership field validation test,
http://www.netl.doe.gov/publications/proceedings/08/rcsp/factsheets/24SWP_Deep%20Saline%20Sequestration_PhIII.pdf
- Ehlig-Economides, C., Economides, M. 2009. Sequestering carbon dioxide in a closed underground volume. *Journal of Petroleum Science and Engineering*. 70. 123-130.

Sulfur and Carbon Isotopic Variation in the Lower Carboniferous: Evidence for OAEs

Peter K. Swart, Samantha Evans, Gregor P. Eberli, and David Katz

Key Findings

- The Lower Carboniferous portion of the Madison Wyoming Formation (Tournasian) show a large carbon isotope excursion which can be correlated globally. The change of almost 7 ‰ is interpreted as reflecting a large transfer of carbon from the ocean-atmosphere into organic rich sediments.
- There is a co-occurring change in the $\delta^{34}\text{S}$ of the carbonate associated sulfate so that the $\delta^{34}\text{S}$ is positively correlated with the $\delta^{13}\text{C}$, suggesting that variations in the two isotopic systems may be related in a similar manner to that seen in the Ocean Anoxic Events in the Cretaceous.
- The positive covariance between $\delta^{13}\text{C}$ and $\delta^{34}\text{S}$ may be evidence of Ocean Anoxic Events during periods such as the Carboniferous during which there are no deep-sea records.
- The $\delta^{34}\text{S}$ of the CAS is also positively correlated with the concentration of Sr in the carbonate. This suggests a link with the solubility of celestite and may indicate that the $\delta^{34}\text{S}$ might have a diagenetic origin.

Background

In this study we present the $\delta^{34}\text{S}$ of carbonate associated sulfate (CAS) measured in a section of partially dolomitized carbonates of Lower Carboniferous age from the Madison Formation in Wyoming, USA. These rocks show a significant positive carbon isotopic shift in the Tournasian/Osagean which can be correlated not only between numerous outcrops in the Western United States, but also to sections in Belgium and Russia (Katz et al. 2007; Saltzman et al. 2004). It has been suggested that these positive excursion represents a world wide change in the $\delta^{13}\text{C}$ of the oceans, perhaps linked to the ocean anoxic events (OAEs), similar to those documented during other time periods such as the Cretaceous. However, unlike the Cretaceous, there are no physical records of the deposition of organic material in deep ocean basins during the Lower Carboniferous as the deep-sea record no longer exists. In order to explore this possibility in greater detail we have examined the record of $\delta^{34}\text{S}$ across this pronounced C isotopic shift. The results show a strong positive correlation between $\delta^{34}\text{S}$ and $\delta^{13}\text{C}$ and therefore strongly link the origin of the $\delta^{13}\text{C}$ excursion with changes in the S cycle. A similar association has been recently noted in some OAEs in the Cretaceous (Jenkyns, 2010). The probable explanation for this positive correlation is that during periods of high organic material formation (which caused the oceanic $\delta^{13}\text{C}$ values to increase), large ocean basins became anoxic, thereby preserving the organic carbon. In these basins the dominant mode of organic material oxidation was through sulfate reduction. During this process the lighter

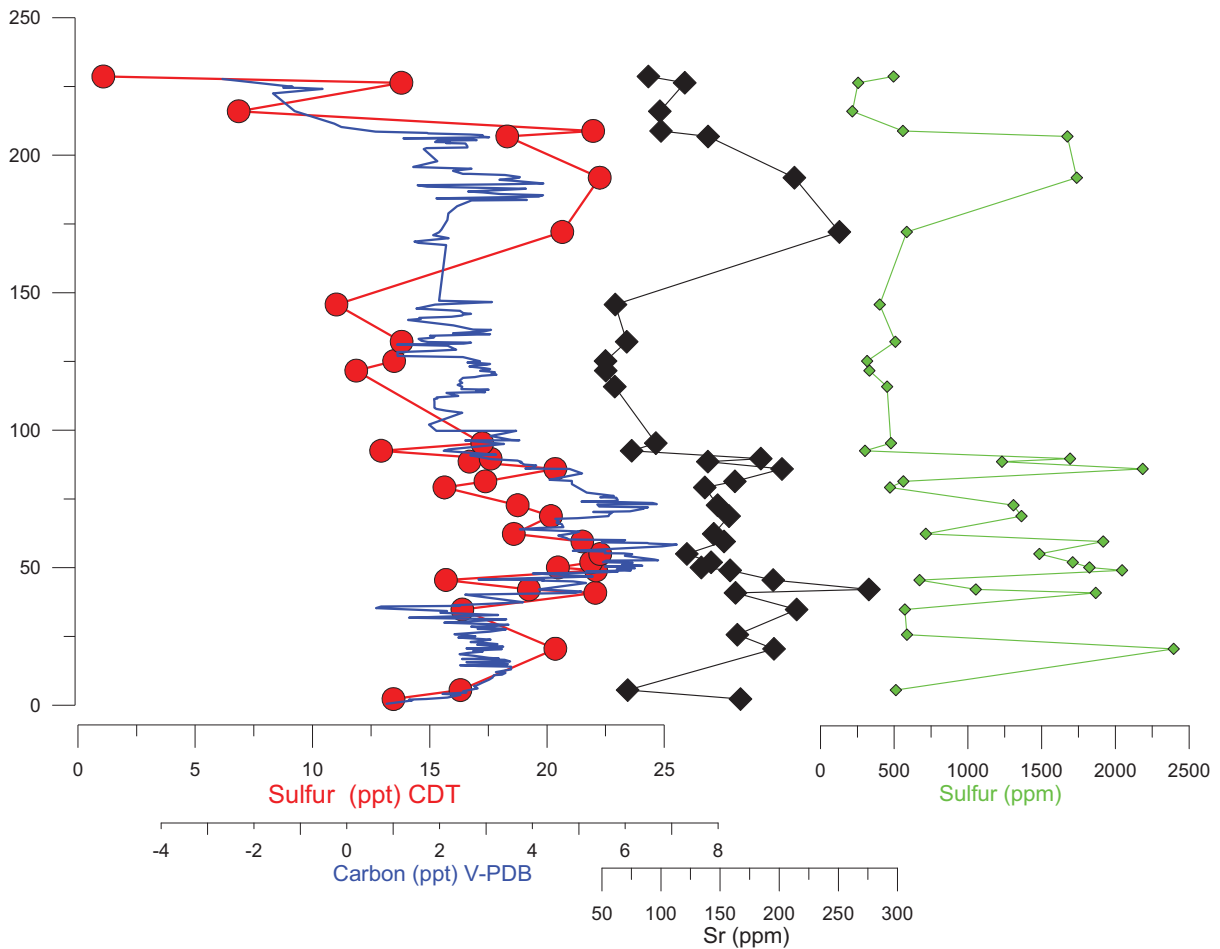


Figure 1: Variations in $\delta^{34}\text{S}$ values of CAS from the Madison Formation (red circles) compared to the $\delta^{13}\text{C}$ in the carbonate (blue). The $\delta^{34}\text{S}$ also shows a positive correlation with the concentration of Sr in the carbonate and to some extent the concentration of sulfur in the carbonate (CAS).

isotope of sulfur is preferentially sequestered in sulfide minerals, leaving water masses in which the sulfate is only partially reduced, enriched in ^{34}S . This enriched sulfate was likely mixed back into the oceans, producing the positive $\delta^{34}\text{S}$ values in the carbonates deposited at this time. The association documented in the Madison Formation rocks may indicate that OAEs were also present during the Lower Carboniferous similar to other portions of the geological record such as the Cretaceous, Jurassic, Ordovician, and Silurian.

Carbonate Associated Sulfate

The issue of CAS, or sulfur trapped within the matrix of carbonate minerals, has attracted significant attention because of the possibility of utilizing this sulfur source to refine the oceanic sulfur isotopic ($\delta^{34}\text{S}$) curve. This curve at present is based mainly on the analysis of evaporite minerals. In addition to the improvement of the $\delta^{34}\text{S}$, $\delta^{34}\text{S}$ analysis of CAS can also provide information regarding oceanic and diagenetic processes influencing carbonate sediments. This study examined the $\delta^{34}\text{S}$ of CAS from a section

from the Madison Formation in Wyoming. This section is Tournasian in age and shows a $\delta^{13}\text{C}$ excursion of almost 7‰ over an interval of 100 m. This excursion can be traced over 500 km between outcrops which represent a progressively deepening sequence along a carbonate ramp. Similar variations are also recognized globally in Europe and Russia. It has been suggested that these positive excursions represent a world wide change in the $\delta^{13}\text{C}$ of the oceans, related to burial of large amounts of organic material, similar to those which occurred during the Cretaceous during Ocean Anoxic Events (OAEs). However, in contrast to the Cretaceous, there are no deep-ocean records of carbon deposition during the Carboniferous and therefore it is not known whether such huge shifts in the $\delta^{13}\text{C}$ represent phenomenon similar to the OAEs.

Results and Discussion

The $\delta^{34}\text{S}$ values of the CAS exhibited an approximate range of between +10 and +23 ‰ (CDT) and showed a positive correlation with the $\delta^{13}\text{C}$ of the carbonates (Figure 1). This type of correlation is similar to that observed in the Cretaceous OAEs. The mechanism proposed for the correlation in the Cretaceous OAEs is that large portion of the deep ocean developed anoxia (Jenkyns 2010). This could have developed either as a result of the massive amounts of organic material which were being produced in the surface ocean (thus enriching the $\delta^{13}\text{C}$ of the oceans), a break down in the ventilation of the deep ocean, or a combination of the two. In these anoxic zones the organic material was partially oxidized by sulfate reducing bacteria leading to fractionation of the sulfur isotope pool in this region. In order to return this sulfur with positive $\delta^{34}\text{S}$ values back into the surface oceans, there had to be a periodic resumption of ventilation of the oceans so that the enriched $\delta^{34}\text{S}$ could influence the shallow carbonates. Hence the observation presented here could be the first evidence of OAEs in the Carboniferous. The $\delta^{34}\text{S}$ also showed a positive correlation with the Sr content of the carbonates (Figure 1). The interpretation of this association is problematic, but may relate to the solubility of celestite. In deep-sea sediments, the concentration of Sr in the pore fluids is limited by the solubility of celestite (Baker and Bloomer 1987), which is controlled by the ion activity product of Sr^{2+} and SO_4^{2-} . Hence a reduction in the concentration of SO_4^{2-} , caused by sulfate reduction, would allow higher concentrations of Sr^{2+} to be present. The Sr in this case being released through the recrystallization of calcite and aragonite. However, this mechanism would not seem to be applicable in the open-ocean as there would be no mechanism of increasing the concentration of Sr. A final, less palatable, hypothesis is that the $\delta^{34}\text{S}$ and the Sr concentrations are diagenetic imprints resulting from $\delta^{34}\text{S}$ signatures developed during burial. This final hypothesis would cast in doubt the use of $\delta^{34}\text{S}$ values of CAS.

References

- BAKER, P.A., and BLOOMER, S.H., 1987, The origin of celestite in deep-sea carbonate sediments: *Geochimica et Cosmochimica Acta*, v. 52, p. 335-340.
- JENKYNS, H.C., 2010, Geochemistry of oceanic anoxic events: *Geochemistry Geophysics Geosystems*, v. 11.
- KATZ, D.A., BUONICONTI, M.R., MONTANEZ, I.P., SWART, P.K., EBERLI, G.P., and SMITH, L.B., 2007, Timing and local perturbations to the carbon pool in the lower Mississippian Madison Limestone, Montana and Wyoming: *Palaeogeography Palaeoclimatology Palaeoecology*, v. 256, p. 231-253.
- SALTZMAN, M.R., GROESSENS, E., and ZHURAVLEV, A.V., 2004, Carbon cycle models based on extreme changes in $\delta^{13}\text{C}$: an example from the lower Mississippian: *Palaeogeography Palaeoclimatology Palaeoecology*, v. 213, p. 359-377.

The $\delta^{13}\text{C}$ of Organic Material in Platform Derived Sediments: Implications for Reconstructing the Global Carbon Cycle

Amanda Oehlert, Kathryn Lamb-Wozniak, Quinn Devlin, Greta J. Mackenzie, John J.G. Reijmer, and Peter K. Swart

Key Findings

- The $\delta^{13}\text{C}$ of organic material cannot always be used to confirm variations in inorganic $\delta^{13}\text{C}$ records interpreted as changes in rates of organic carbon production, burial and preservation.
- Knowledge of regional sea-level history, as well as proximity to platform margin are necessary to generate accurate interpretations of $\delta^{13}\text{C}$ records identified in periplatform sediments.
- The evolution of new organisms may change the relationship of the $\delta^{13}\text{C}_{\text{inorganic}}$ and $\delta^{13}\text{C}_{\text{organic}}$ through time.

Introduction

Changes in the $\delta^{13}\text{C}$ of carbonate sediments through geological time have been interpreted to represent relative variations in the rate of organic carbon production, burial and decomposition. This has led to the description of global carbon cycling through time, and unique and correlatable fluctuations have been used as stratigraphic tie points for globally disparate locations. Carbonate sediments deposited in the deep sea have been the primary source of information about carbon cycle fluctuations and their $\delta^{13}\text{C}$ values have been used to identify major carbon cycle changes such as hyperthermal events, major glaciations, and ocean anoxic events. However, deep marine sequences older than 200 myrs have generally been subducted. As a result, many workers substitute carbonates deposited in marginal settings, including carbonate platforms, epeiric seas, and ramps (Hotinski et al., 2004; Saltzman et al., 2004).

A study conducted on multiple shallow marine carbonate platforms showed the $\delta^{13}\text{C}_{\text{inorganic}}$ records recovered around the world demonstrated a $\delta^{13}\text{C}_{\text{inorganic}}$ pattern unrelated to the global carbon cycle (Swart, 2008). In order to prove that this pattern resulted from global

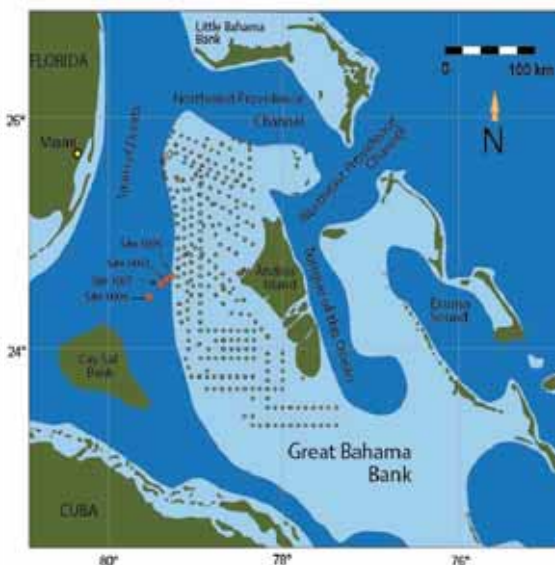


Figure 1: Map of study area showing locations of ODP Leg 166 cores 1003, 1005, 1006, and 1007 (orange circles) and locations of sediment samples from the bank top (yellow

sea-level changes, another record unaffected by diagenesis was necessary to establish the primary nature of the $\delta^{13}\text{C}_{\text{inorganic}}$ signal identified in periplatform sediments. The $\delta^{13}\text{C}$ of co-occurring organic material ($\delta^{13}\text{C}_{\text{organic}}$) has often been used to corroborate changes in the global $\delta^{13}\text{C}_{\text{inorganic}}$ signal. Typically, if both the $\delta^{13}\text{C}$ of the inorganic and organic portions covary in a sedimentary sequence, it is assumed that the variations in the $\delta^{13}\text{C}_{\text{inorganic}}$ values are robust and indicate a real change in the $\delta^{13}\text{C}_{\text{inorganic}}$ of the environment.

This study examined the relationship between $\delta^{13}\text{C}_{\text{organic}}$ and $\delta^{13}\text{C}_{\text{inorganic}}$ in a relatively recent carbonate setting in that measurements of the $\delta^{13}\text{C}_{\text{organic}}$ were made on the same samples in which the $\delta^{13}\text{C}_{\text{inorganic}}$ values were reported by Swart and Eberli (2005). These data were combined with $\delta^{13}\text{C}_{\text{organic}}$ values from the surface sediments of Great Bahama Bank, as well as the various individual organic components which degrade to form the organic matter in these sediments (Fig. 1).

Results

ODP Leg 166 Sites 1003-1007

The $\delta^{13}\text{C}$ values of the organic material ($\delta^{13}\text{C}_{\text{organic}}$) recovered from the periplatform sediments of Leg 166 averaged -15.4‰, and ranged from -14.4 to -16.8‰. The most depleted values were found at Site 1006, furthest from the platform margin, with values becoming progressively heavier closer to the margin. The correlation between the $\delta^{13}\text{C}_{\text{organic}}$ and $\delta^{13}\text{C}_{\text{inorganic}}$ ranged from zero at Sites 1005 ($r^2=0.09, p>0.1$) to a statistically significant positive correlation at Site 1006 ($r^2=0.64, p<0.01$, Fig. 2.). The Pleistocene portion of Site 1006 (the only site at which there was a reasonable continuous Pleistocene record) showed a general pattern in which the more positive $\delta^{13}\text{C}_{\text{organic}}$ values were correlated with positive $\delta^{13}\text{C}_{\text{inorganic}}$ values. These positive values occurred during interglacial periods as defined by negative $\delta^{18}\text{O}$ values of the foraminifera *Globigernoides ruber* and high concentrations of aragonite (Kroon et al., 2000).

Surface of Great Bahama Bank

The $\delta^{13}\text{C}$ of the sedimentary organic material from the bank top averaged -12.2‰ and ranged from -10.9 to -14.3‰. The correlation between the $\delta^{13}\text{C}_{\text{organic}}$ and $\delta^{13}\text{C}_{\text{inorganic}}$ showed no statistically significant correlation on the bank top ($r^2=0.02, p>0.1$), with the exception of the mud-rich wackestone ($r^2=0.70, p<0.01$).

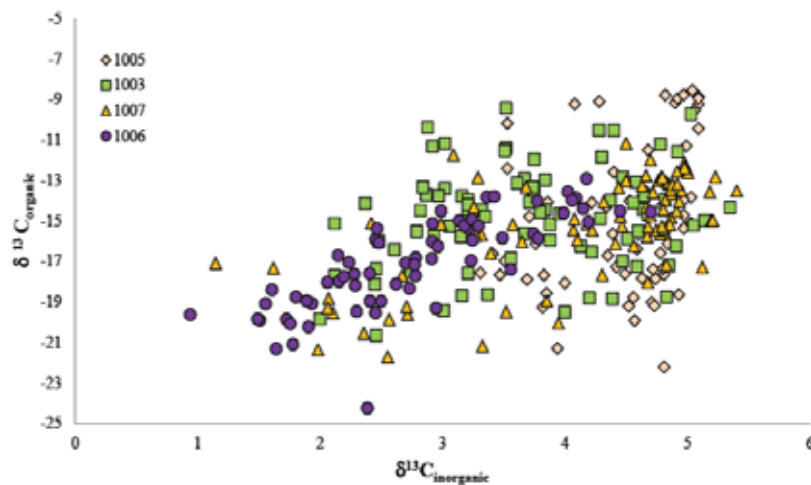


Figure 2: Graph of the correlation between the inorganic and organic $\delta^{13}\text{C}$ values at each ODP Leg 166 Site (1003-1007).

Conclusions

The sedimentary $\delta^{13}\text{C}_{\text{organic}}$ values of the platform top sediments were the result of a contribution of organic material from a variety of sources. Consequently, there was no correlation between the $\delta^{13}\text{C}_{\text{organic}}$ and $\delta^{13}\text{C}_{\text{inorganic}}$ records with the exception of the mud dominated facies. Thus, the average sediment that was available for export from the platform top to the slope was characterized by a relatively heavy organic $\delta^{13}\text{C}$ composition ($-12.2 \pm 1.3\text{‰}$) as well as a relatively heavy inorganic $\delta^{13}\text{C}$ composition ($+4.6 \pm 0.4\text{‰}$).

It can be expected that the sediments deposited on the slopes of GBB would exhibit $\delta^{13}\text{C}_{\text{organic}}$ values that reflects a mixture of platform-derived ($\sim -12.0\text{‰}$) and ocean-derived organic carbon ($\sim -21.0\text{‰}$). The correlation between the $\delta^{13}\text{C}_{\text{organic}}$ and $\delta^{13}\text{C}_{\text{inorganic}}$ changed substantially with increasing distance from the platform margin. In the proximal cores, Sites 1003 and 1005, there was either a very weak or a not statistically significant correlation between $\delta^{13}\text{C}_{\text{organic}}$ and $\delta^{13}\text{C}_{\text{inorganic}}$ values. Conversely at the toe of the slope, Site 1007, and the basin core, Site 1006, there were strongly positive correlations between the organic and inorganic $\delta^{13}\text{C}$ records. If the surface of GBB is considered to be the source of isotopically positive $\delta^{13}\text{C}$ organic material, and the pelagic contribution is a source of isotopically negative organic material, then the $\delta^{13}\text{C}_{\text{organic}}$ values in periplatform sediments can be explained by a simple mixing model between these two sources.

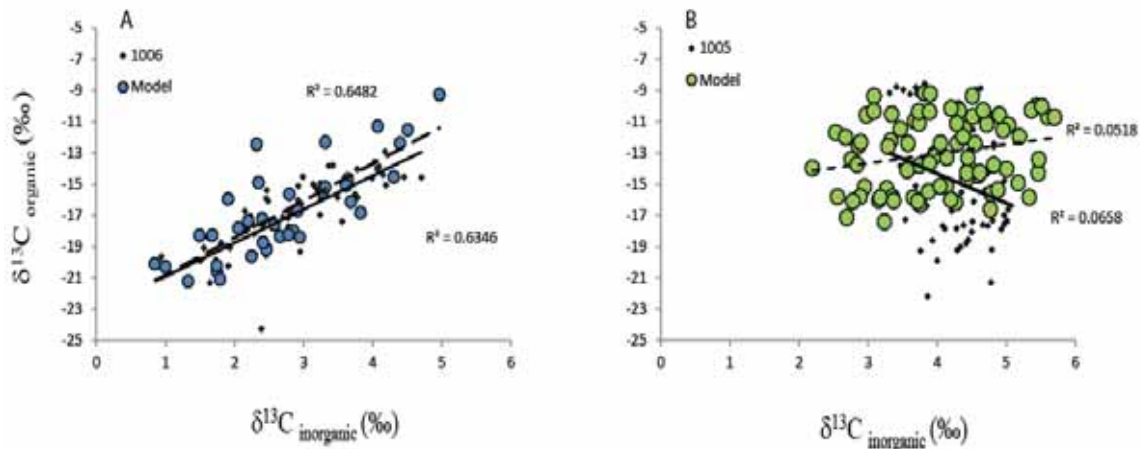


Figure 3: Modeling of the $\delta^{13}\text{C}_{\text{inorganic}}$ and $\delta^{13}\text{C}_{\text{organic}}$ values of the sediments at Sites 1006 (A) and 1005 (B). (A) Model results (blue circles) are plotted on the same axes as the values measured from the sediments (blue diamonds). The observed correlation at Site 1006 ($r^2=0.64$) can be simulated by a platform contribution of organic material and sediments that ranges from 20-90% through time (B) Model results (large green circles) are plotted on the same axes as the measured values (green diamonds). At Site 1005, the observed correlation ($r^2=0.07$, solid line) was simulated through a platform contribution that ranges from 75-90% through time.

This two source mixing model would predict that (i) sediments closer to the platform should be isotopically heavier than those further away, (ii) there should be higher concentrations of organic carbon in sediments closer to the platform, and (iii) there should be an increase in the correlation between $\delta^{13}\text{C}_{\text{organic}}$ and $\delta^{13}\text{C}_{\text{inorganic}}$ in cores further away from the platform. These patterns are observed in the four sites off GBB. The observed trend can be adequately simulated using a simple mixing model, which can

predict the percent input from each source, at each location along the transect (Fig. 3). In this case, the composition of sediment at Site 1006 was between 10 to 80 % platform derived. This relationship changes at Site 1007 to contributions between 40 to 90%, and 75 to 99% at Site 1005.

Application to Ancient Shallow Marine Carbonate Platform Systems

The results of this study call into question the applicability of using the $\delta^{13}\text{C}$ values of the organic carbon from shallow marine carbonate platforms as a method to corroborate changes in the $\delta^{13}\text{C}$ values of inorganic carbonates. The covariance between the $\delta^{13}\text{C}_{\text{inorganic}}$ and $\delta^{13}\text{C}_{\text{organic}}$ in the sediments along the transect from GBB do not exhibit a consistent relationship between the two records at every location. The results of this study have generated a specific model describing how sea-level fluctuations can initiate or terminate the carbonate factory on shallow marine platforms. At proximal locations such as Sites 1005 and 1003, decoupled $\delta^{13}\text{C}_{\text{inorganic}}$ and $\delta^{13}\text{C}_{\text{organic}}$ records are observed because the cores consist primarily of platform material which does not demonstrate a covariation between $\delta^{13}\text{C}_{\text{inorganic}}$ and $\delta^{13}\text{C}_{\text{organic}}$. Distal locations such as Sites 1006 and 1007 demonstrate appreciable covariances between the $\delta^{13}\text{C}_{\text{inorganic}}$ and $\delta^{13}\text{C}_{\text{organic}}$ values because they are the result of a two point mixing system between pelagic and platform produced material. As a result, the covariance of the $\delta^{13}\text{C}_{\text{inorganic}}$ and $\delta^{13}\text{C}_{\text{organic}}$ records recovered from periplatform material cannot be the only means of interpreting global carbon cycling at a study site. A thorough understanding of the depositional environment from which the sediment is sampled, and local sea-level history are the required contextual information necessary to generate interpretations about the coupling or decoupling of $\delta^{13}\text{C}_{\text{inorganic}}$ and $\delta^{13}\text{C}_{\text{organic}}$ records in ancient shallow marine carbonate platforms.

References

- Hotinski, R.M., Kump, L.R. and Arthur, M.A. 2004. The effectiveness of the Paleoproterozoic biological pump: A $\delta^{13}\text{C}$ gradient from platform carbonates of the Pethei Group (Great Slave Lake Supergroup, NWT). *Geological Society of America Bulletin*, 116: 539-554.
- Kroon, D., Reijmer, J.J.G. and Rendle, R. 2000. Mid- to late Quaternary variations in the oxygen isotopic signature of *Globigernoides ruber* at Site 1006 in the western subtropical Atlantic. In: *Proceedings of the Ocean Drilling Program Scientific Results* (Eds P.K. Swart, G.P. Eberli and M.J. Malone), 166, pp. 13-22. Ocean Drilling Program, College Station.
- Saltzman, M.R., Groessens, E. and Zhuravlev, A.V. 2004. Carbon cycle models based on extreme changes in $\delta^{13}\text{C}$: an example from the lower Mississippian. *Palaeogeography Palaeoclimatology Palaeoecology*, 213: 359-377.
- Swart, P.K. 2008. Global synchronous changes in the carbon isotopic composition of carbonate sediments unrelated to changes in the global carbon cycle. *Proceedings of the National Academy of Science*, 105: 13741-13745.
- Swart, P.K. and Eberli, G.P. 2005. The nature of the $\delta^{13}\text{C}$ of periplatform sediments: Implications for stratigraphy and the global carbon cycle. *Sedimentary Geology*, 175: 115-130.

Speleothems from Bahamas Blue Holes: Geochemical archives of Atlantic climate variability

Monica M. Arienzo and Peter K. Swart

Key Findings

- Stalagmites from the Bahamas offer a unique opportunity to analyze climate variability in the subtropical Atlantic
- Complete geochemical records from two stalagmites have been analyzed from 13.5 to 54.0 ka and demonstrate similar responses across Heinrich events
- Trace element records suggest that atmospheric dust may be an important feature of Heinrich events

Introduction

Millennial scale climate variability is a pervasive feature of climate for the last million years. There is evidence for global millennial scale variability during the last glacial period, dominated by Heinrich events and Dansgaard-Oeschger (D/O) events. These events have been documented in the ice core records, deep-sea sediment records and speleothems. Ice core records from Greenland provide a temperature record for the region and demonstrate a change of up to 16°C. Sediment cores from the North Atlantic reveal an increase in ice rafted debris (IRDs), which supports a southward extension of the Laurentide ice sheet and an increase in iceberg discharge associated with Heinrich Events. Speleothem records from diverse localities such as South and Central America, Continental United States, Europe, and China demonstrate changes in precipitation and temperature. However, there is a significant lack of paleoclimate data from the subtropical Atlantic which is critical to understanding the global nature of these events. Our analyses of stalagmites from the Bahamas reveal that Heinrich events are preserved in the geochemical signature of our samples.

Methodology

To date, over 15 stalagmites have been collected and dated from Blue Holes in the Bahamas. Currently submerged, the speleothems are collected using advanced diving techniques at depths ranging from 10 to 40 m below sea level. Two samples, DC-09

Sample	Location	Depth (m)	Age range (ka)
DC-09	Dan's Cave, Abaco Island	16.5	13.7 – 30
DC-14	Dan's Cave, Abaco Island	23.5	13.8 – 54

Table 1: Sample location, collection depth and age range for the analyzed samples

and DC-14, have been analyzed for complete geochemical records (Table 1, Figure 1). These samples have been analyzed for stable carbon and oxygen isotopes, as well as trace elements, at a 20 μm resolution. Oxygen isotope analysis relies on the determination of the ratio of $^{18}\text{O}/^{16}\text{O}$ of the sample relative to a standard by a mass

spectrometer. In the subtropics it has been demonstrated that the amount of rainfall greatly impacts the $\delta^{18}\text{O}$ of the water (Fairchild et al., 2006). Higher rainfall leads to a more depleted $\delta^{18}\text{O}$ signal, whereas heavier $\delta^{18}\text{O}$ values are attributed to lower amounts of rainfall. Carbon isotope values are also linked to temperature and rainfall amount (Fairchild et al., 2006).



Figure 1: a) Sample DC-09 and b) DC-14 with U/Th ages

Implications

Preliminary analysis reveals enrichment in the carbon and oxygen isotope values with amplitudes as large as 4.5‰ associated with Heinrich events. This reflects a change from relatively arid to wetter conditions, which occur over periods as short as 50 years. When comparing the record from DC-09 to DC-14, DC-09 shows a greater C and O change associated with each Heinrich event. This is possibly driven in part by the differences in depth at which the samples were forming.

Also associated with these events is an elevated iron concentration. As the Bahamas is an isolated carbonate platform and does not contain any indigenous sources of iron, we propose that the allogenic iron is derived from Saharan dust, transported to the Bahamas by the trade winds. The iron is leached from the dust through rainwater infiltration and is then co-precipitated with the calcite in the stalagmite. During Heinrich events, there is evidence of significant aridification of the Sahara

region of Africa; therefore large amounts of atmospheric dust could be exported to the Bahamas during these events. This suggests that atmospheric dust may be an important feature of abrupt climate change events.

These records provide a unique opportunity to study climate variations during Heinrich events and may better define the role of the subtropics in forcing such changes. Dating of speleothem formations have also been successfully used in the study of sea-level change in the Bahamas (Lundberg and Ford, 1994). Future dating may better aid in our understanding of sea-level rise during deglaciation in the Bahamas.

References

- Fairchild, I. J., Smith, C. L., Baker, A., Fuller, L., Spotl, C., Matthey, D., McDermott, F., EMIF 2009. Modification and preservation of environmental signals in speleothems, *Earth-Science Reviews*, 75, 105-153.
- Lundberg, J., Ford, D. C. 1994. Late Pleistocene sea level change in the Bahamas from mass spectrometric U-series dating of submerged speleothem, *Quaternary Science Reviews*, 13, 1-4.

The Use of Multiply Substituted ‘Clumped’ Isotopologues in Carbonate Geochemistry

Sean T. Murray and Peter K. Swart

Key Points

- A multiply substituted isotopologue is the natural formation of an isotope bond with multiple isotopic rare elements. With precise measurement, the concentration of ^{13}C - ^{18}O bonds in carbonates can be inferred from measuring the bonds in CO_2
- These measurements can be correlated with temperature of formation creating an accurate paleothermometer that extends beyond the Pleistocene
- They have tremendous potential for the study of diagenetic processes in carbonates

Introduction

Paleothermometry of carbonates has only had limited application to time periods beyond the Pleistocene. This is because of the restrictive requirement of needing to know the oxygen isotope concentration in both the carbonate sample and the water in which it formed in order to calculate formation temperature (Ghosh et al. 2006).

The study of multiply substituted isotopologues examines the natural formation of bonds between multiple rare isotopes (e.g. C^{13} , O^{18} , etc.) rather than with more common isotopes. For example, the formation of the isotopologue $^{13}\text{C}^{18}\text{O}^{16}\text{O}$ (occurring at mass 47) is primarily dependent upon temperature rather than the isotopic composition of the ^{18}O or ^{13}C in the water (Ghosh et al. 2006). By comparison of the measured ratio of 47/44 with the stochastic ratio of 47/44 a parameter known as $\Delta 47$ can be determined which is rigorously temperature dependent.

High precision measurements are necessary in clumped isotope geochemistry as a result of the low abundance of the isotopologue, $^{13}\text{C}^{18}\text{O}^{16}\text{O}$. By using the standard technique of phosphoric acid digestion of carbonate, CO_2 can be collected and analyzed by mass spectrometry on a Thermo-Finnigan 253. This instrument has six collectors allowing for the simultaneous collection of masses 44 through 49 allowing for precision measurements of better than 0.01‰ (Huntington et al. 2009). This means a precision of 1-2 °C can be achieved for the formation of carbonates by analysis of multiply substituted isotopologues. The instrument capable of these analyses will be installed in the stable isotope laboratory in December. We will apply this technique to both primary and diagenetic carbonates.

References

- P. Ghosh, J. Adkins, H. Affek, B. Balta, W. Guo, E. Schauble, E.D. Schrag. ^{13}C - ^{18}O bonds in carbonate minerals: A new kind of paleothermometer. *Geochimica et Cosmochimica Acta* 2006, 70, 1439.
- K.W. Huntington, J.M. Eiler, H.P. Affek, W. Guo, M. Bonifacie, L.Y. Yeung, N. Thiagarajan, B. Passey, A. Tripathi, M. Daeron and R. Came. Methods and limitations of ‘clumped’ CO_2 isotope ($\Delta 47$) analyses by gas-source isotope ratio mass spectrometry. *Journal of Mass Spectrometry* 2009.

Characterization of Onlapping Reef Sequences: The Dominican Republic Drilling Project

James S. Klaus, Donald F. McNeill, Albertus Ditya, Yula Hermanati, Gregor Eberli, and Peter Swart

Key Findings

- Nine new core borings, forty outcrop cores, and outcrop samples document the lithofacies geometry of reef-related clinothems.
- Coral fauna provides preliminary depositional setting, correlation, and age control, including the transition from older *Stylophora*-dominated to modern *Acropora*-dominated fringing reefs.
- Wireline logging planned to confirm key stratigraphic boundaries and define porosity zones.

Project Summary

A combination of core borings and outcrops are used to evaluate the coral-rich clinothems that form a series of onlapping parasequences. Nine new core borings, over forty outcrop cores, and numerous outcrop samples document the facies within a series of highstand depositional events ranging from late Pliocene to Pleistocene. The uplifted southern coast of Hispaniola exposes several terraces that consist of low-angle (5-7° foreslope, ~1° topset) cliniform (sigmoidal) deposits composed of skeletal sand, coral debris, and in situ framework.

The multi-year Dominican Republic Drilling Project (DRDP) project was initiated with support of the Industrial Associates in the summer of 2010 with core drilling and surface sampling. A wireline logging effort is planned (early 2011) and a second phase of drilling pending external support (NSF proposal pending).

Project Objective

Reefs present special challenges for geological and geophysical studies. Reefs are often comprised of disparate carbonate facies arranged in unpredictable and complex three-dimensional arrangements. Furthermore, the petrophysical attributes of reefs can be highly variable at small spatial scales within individual facies. During high-frequency sea level cycles these challenges can become compounded by the formation of onlapping parasequences and iterative phases of diagenetic alteration. The Pliocene-Pleistocene reefs of the southern Dominican Republic (DR) provide a unique opportunity to study the complex three-dimensional architecture and resulting petrophysical attributes of reefs during a period of high-frequency sea level oscillation and superimposed sequential diagenesis.

Regional Geologic & Tectonic Setting

An approximately 150 mile coastal plain bounded by the Cordillera Central to the west and the Cordillera Oriental to the north characterizes the southeastern region of the Dominican Republic. Along the coast, a series of 6 to 8 fairly continuous terraces (Barrett 1962) are encountered in a belt of coastal reef limestones (Figure 1). Like Barbados (Broecker et al., 1968; Mesolella, 1968, Mesolella et al., 1969, 1970; Blanchon and Eisenhauer, 2001; Schellmann and Radtke, 2004) and the coast of Huon Peninsula, New Guinea (Aharon and Chappell, 1986; Eisenhauer et al., 1993; Esat et al., 1999), the reef terraces are preserved by long-term tectonic uplift, such that the youngest formations are located at the lowest elevations close to the present coast, and older reef terraces at higher elevations and further inland.

Radiometric age dates of the youngest 6 m reef terrace suggest an age of ~125 Ka (marine oxygen isotope substage (MIS) 5e (Mann et al., 1995). While no radiometric ages have been determined for the higher terraces, it can be speculated from the sheer number and elevations of terraces and abundance of now extinct coral genera (*Caulastrea*, *Stylophora*, *Placocyathus*), that they represent reef growth back to MIS-31 (~1 Ma) and older. Outcrops from numerous building excavations in Santo Domingo and quarry exposures east of the airport contain abundant *Stylophora minor* and *Stylophora monticulosa*, species not thought to extend beyond the early Pleistocene (0.78 Ma) (Budd et al., 1994).

Based on the digital elevation model (DEM) of the southern coast (Figure 2), the three most clearly defined and traceable terraces are the 6 m coastal terrace, the broad 15 m terrace, and the prominent 30 m terrace. The 30 m terrace gradually increases in elevation landward to a maximum of ~60 m. A prominent terrace is often seen at ~42 m. Based on these elevations, the relative heights of past sea level highstand events, and the well constrained age of the 6 m terrace (125 ka), we estimate the 15 m terrace to represent MIS-7/9, and the 30 m terrace MIS-11 reef growth. The prominent nature of the 30 m escarpment is consistent with recent research suggesting MIS-11 was the longest and warmest interglacial interval of the past 500 kyr (Droxler et al., 1997; Poore et al., 1999; Droxler and Farrell, 2000). Reef growth from what is probably MIS-13-25 is likely underlying the 30 m MIS-11 deposits. The thickness of the 30 m (MIS-11) reef varies, and can be seen in numerous quarry and building excavations to be lying unconformably upon significantly older Pleistocene reef deposits (MIS-31 and older). In the area east of Las Americas airport, a prominent 42 m terrace is seen. This is likely associated with the large MIS-31 highstand (~1 Ma). Deposits underlying the 42 m terrace, and at higher

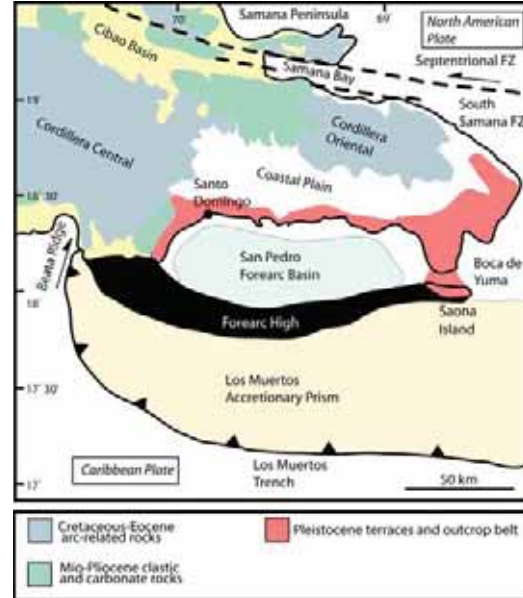


Figure 1: Geological and tectonic map of the Dominican Republic. Pleistocene outcrop belt shown in red. Modified from Mann et al. (1995).

elevation (up to 60 m) can be subdivided into progressively older highstand reefs that cumulatively form the broad 60 m terrace and reef flat that is particularly prominent in the Capital city of Santo Domingo. These older reef deposits are dominated by *Stylophora*, and formed during the low amplitude 40 kyr sea level cycles of the late Pliocene and early Pleistocene.

Preliminary Lithofacies and Key Stratigraphic Boundaries

Initial core descriptions on whole core prior to slabbing allow identification of the major lithologic units and their related bounding surfaces. The cores contain stacked shallowing upward reef packages (Figure 3). Each depositional package generally consists of a basal unit of branching-coral fragments in a skeletal packstone matrix (coral floatstone), and an upper unit of shallow water corals, both branching and massive, in a skeletal packstone to grainstone matrix. The bounding surfaces of the depositional packages tentatively appear to be hardground/non-depositional surfaces or subaerial exposure surfaces. The uplifted terraces are assumed to be older as elevation increases, however, each terrace may be a composite of several Quaternary highstand events. The geometry of the deposits are generally sigmoidal, with a low angle to horizontal topset and an inclined forest (5-7°). The younger deposits generally onlap the uplifted clinoform topography of the previous sequence.

The oldest reefal deposits can be observed in an ~18 m deep quarry excavation (Borda) on the top of the 40-50 m terrace (Figure 3). A series of three shallow-water Plio-Pleistocene (MIS-33-55?) reefs are stacked and separated by clearly defined subaerial exposure surfaces. These reefs are dominated by the extinct Caribbean coral genera *Stylophora* and the dominant modern reef corals *Acropora palmata* and *Acropora cervicornis*. The top of the quarry exposure is capped by back reef/lagoonal deposits of the younger MIS-31 reef consisting of coarse sand and scattered patch reefs of *Montastraea annularis*. As seen in core 2, the MIS-31 deposits thicken towards the 40 m escarpment where they are dominated by typical reef crest corals including *Acropora palmata* and *Diploria strigosa*. The MIS-31 reefs are characterized and easily recognizable in both core and outcrop by the absence of *Stylophora*, and the presence of the extinct genera *Caulastrea*. The boundary with the older underlying deposits is easily recognized by a prominent exposure surface and the presence of *Stylophora*. Two cores were drilled on top of the 30 m terrace; core 1 near the base of the 40 m escarpment, and core 3 near the seaward edge of the 30 m terrace. Core 1 consists of a thick package of MIS-11 back reef/ lagoon deposits overlying the fore reef deposits of the MIS-31 reef

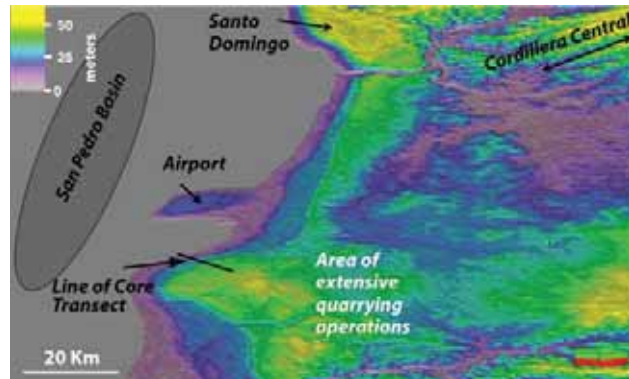


Figure 2: Digital elevation model of southern coast east of Santo Domingo, D.R.. Colors clearly define the 6 m coastal terrace (purple), the 15 m terrace (blue), the 30 m terrace (green), and the 40-50 m terrace (yellow). A transect of five cores was drilled east of Las Americas Airport in an area of extensive quarrying operations.

recognized at ~26 m depth in the core. Core 3 is significantly more complex, consisting of a series of shallowing upward reef sequences bounded by exposure and hardground surfaces. While we currently lack important age constraints, it is likely that the base of this core represents a number of older Pleistocene reefs (MIS-13-29). Core 4, drilled on the 15 m terrace is similar in being composed of a number of shallowing upward reef sequences, likely formed during sea level highstands associated with MIS-7 and MIS-9. Core 5 (20 m) documents a single shallowing upward reef sequence formed during the last interglacial (MIS-5).

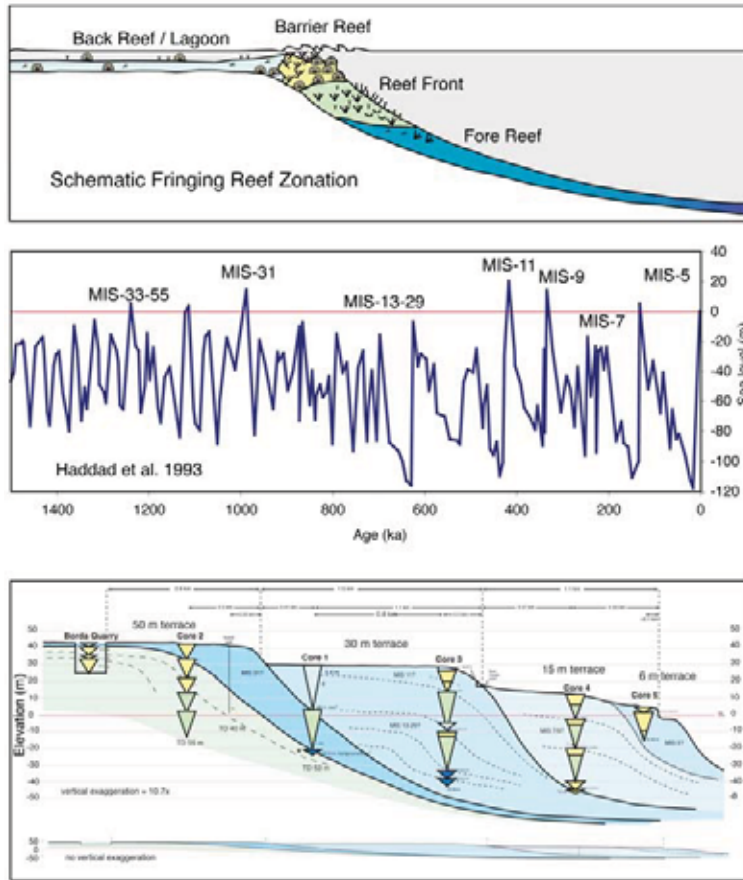


Figure 3: (top) Schematic cross-section of typical fringing reef zonation. Color coding of major reef zones used to distinguish depositional facies in the DR terrace deposits. (middle) Sea-level curve for the past 1.5 Ma based on corrected oxygen isotope curve of benthic foraminifera from site 607 in the North Atlantic Ocean (Haddad et al. 1993). Cross-sectional model of Pleistocene reef development on the southern coast of the Dominican Republic east of Las Americas Int. Airport (Figure 2) including 5 recently acquired cores. Preliminary facies characterizations correspond to the schematic fringing reef zonation model (top).

Selected References

- Barrett, W. J., 1962, Emerged and submerged shorelines of the Dominican Republic, *Revista geográfica: Instituto Pan-Americano de Geografía e História*, vol. 56, p. 51-77.
- Mann, P., F. W. Taylor, R. Lawrence Edwards, and T. Ku, 1995, Actively evolving microplate formation by oblique collision and sideways motion along strike-slip faults: An example from the northeastern Caribbean plate margin, *Tectonophysics*, vol. 246, p. 1-69.
- Mesoella, K. J., 1968, *The Uplifted Reefs of Barbados: Physical Stratigraphy, Facies Relationship and Absolute Chronology. Parts 1 and 2.* Providence, Rhode Island: Brown University, Doctoral thesis. 736. p.

Sonic Velocity Variations in Pleistocene Reef Systems, southern Dominican Republic

Albertus Ditya, Gregor P. Eberli, Donald F. McNeill, and James Klaus

Key Findings

- Velocity is high in the entire reef system including the skeletal grainstone associated with the coral framestone. Velocity variations at a given porosity are not related to either depositional environment or age.
- Two types of cements are commonly found: meteoric cements and micritic microbial cements.
- The high velocity of grainstones can be explained by early micritic cementation.
- The pore types in the reef system tend to be simple but vary in pore size.

Introduction

Reef growth is highly variable even over a small spatial scale, which presents special challenges for geological and geophysical studies (Jordan and Wilson, 1998). A prograding Pleistocene reef system uplifted in the southern Dominican Republic provides a unique opportunity to study its complex three-dimensional architecture, the diagenetic alteration and the petrophysical characteristics. This study focuses on the last objective and we report the first results of what will be a comprehensive data set for assessing the variability in petrophysical properties in these reef rocks.

Fourteen 1 m cores and sixteen hand samples were taken from the various lithologies, depositional environments, and diagenetic features (Figure 1). The lithologies range from wackestones to boundstones that were deposited in back reef, reef crest and fore reef environments. Fifty cylindrical miniplugs, 2.41 cm in diameter, were cut from the different lithologies and depositional environments. Thin sections from one end of each plug were used for petrographical and digital image analysis.

Porosity was measured using a helium picnometer. The p-wave and two orthogonal shear wave velocities were measured using a NER Autolab 1000 system under dry conditions and with variable confining pressures (5, 10, 15, and 20 MPa). Thin sections were petrographically examined and photographed for Digital Image Analysis (DIA).

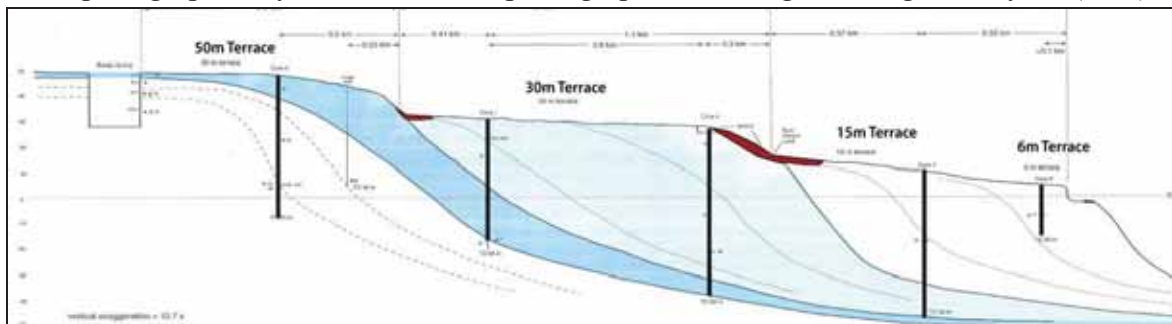


Figure 1. Schematic display of the prograding reef terraces. Samples for this study were taken along the surface of the terraces. Vertical black lines shows position of the cores drilled in 2010.

DIA parameters, which are gamma, aspect ratio, dominant pore size (DOMsize) and perimeter over area (POA), were calculated using the methodology described by (Weger et al., 2009).

Results

The porosity of the samples varies from 7 to 40%. The compressional velocities vary from 3127 km/s to 6051 km/s; the shear waves from 1726 km/s to 3270 km/s. As effective pressures increase from 5 MPa to 20 MPa, the V_p increases in two major different gradients, whereas the V_s remain unchanged. The differences in gradient velocity are caused mainly by various degrees of cementation. All V_p values (@ 20 MPa) are above the Wyllie's time average V_p with a generally inverse correlation between porosity and velocity. At any given porosity, however, large velocity variations of up to nearly 2 km/s occurred (Figure 2).

The V_p/V_s ratio in most of the samples ranges from 1.75 to 2, however, values of 1.6 or 2.35 occurred. The V_p/V_s ratio has a non-constant relationship with porosity, however, variation in the ratio is shown mostly by the high porosity rocks. The increment of the ratio with pressure does not show a unique pattern. The cross plot of V_p/V_s vs. DOMsize shows that larger pores have higher V_p/V_s ratios. But, for samples with small DOMsize the correlation shows a wide range in the V_p/V_s ratio.

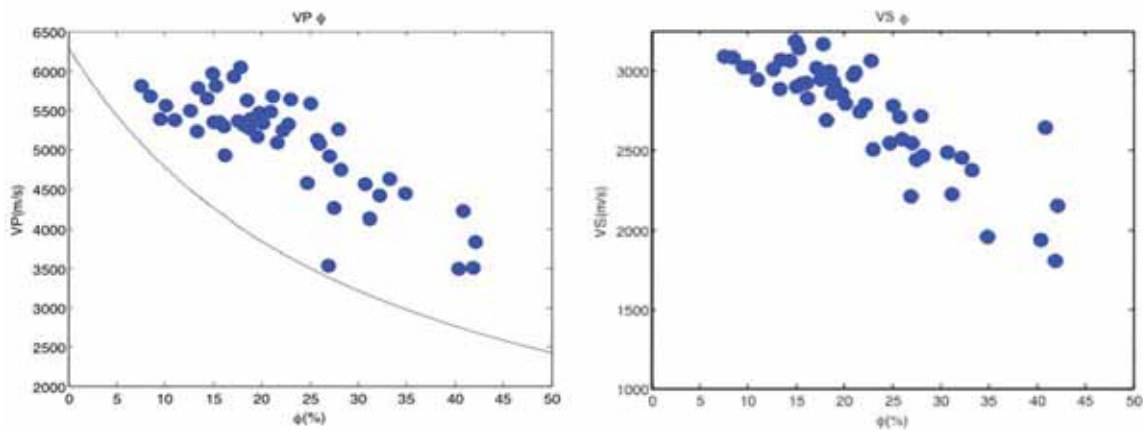


Figure 2. Cross-plot porosity vs V_p and V_s at 20MPa confining pressure. Line in V_p - ϕ plot is the trend line of the Wyllie's time average equation (Wyllie, 1956).

Factors Controlling Sonic Velocity

Reef rocks are generally fast but the large variation at any given porosity in our data set is unexpected. These variations are not due to the depositional environment, texture or the age (Figure 3). The pore types are predominantly intraframe, moldic and vuggy. Rocks with these pore types are known to have high acoustic velocity even if porosity is high (Anselmetti and Eberli, 1993). In these rocks the frame or the cements around the molds produce the necessary rock stiffness for high acoustic velocity. Samples with interparticle pores tend to be somewhat slower but are still fast (Figure 3b). These samples have ubiquitous micritic cements occurring either at grain contacts or more often as bridging cements between the grains (Figure 4). This cement seems to produce enough stiffness to make these grainstones acoustically fast.

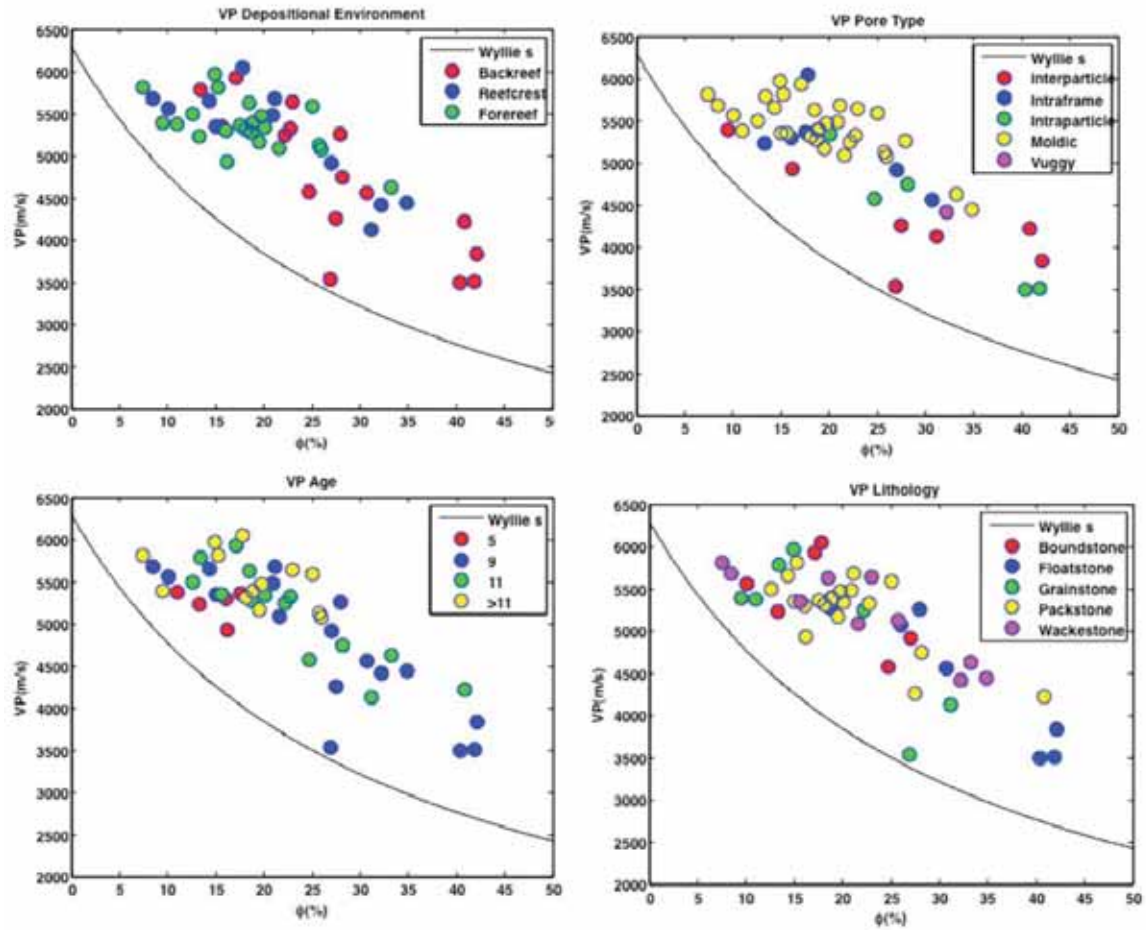


Figure 3. Cross-plot between porosity and V_p with the superposition in color of: (a) Depositional Environment, (b) Pore type (c) Age given as the Marine Isotope Stages (MIS) 5 – 11, and (d) Texture.

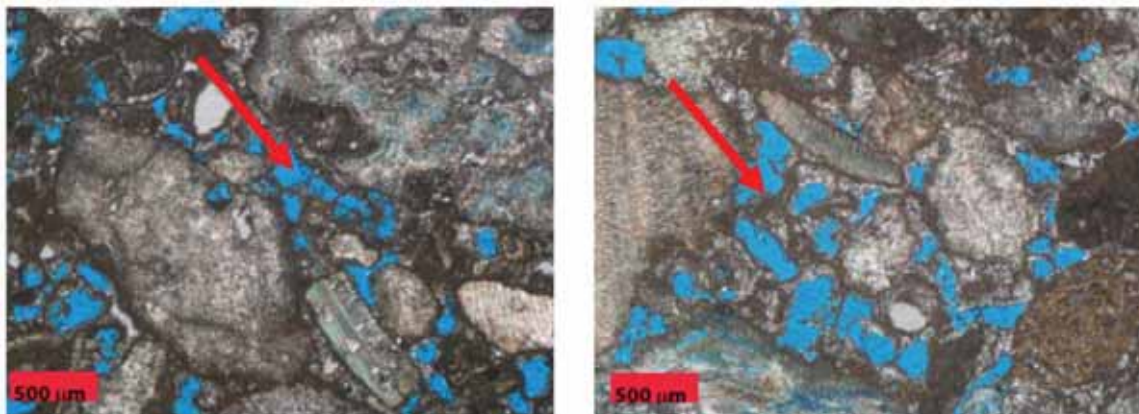


Figure 4. Thin section photomicrographs from a grainstone deposited during the last sea level highstand (MIS 5e). Abundant micritic cement with a filamentous appearance connects the grains and is sometimes mantled by calcitic spar (right picture). This rock with interparticle porosity ($\phi=0.18$) has a high V_p of 5357 km/s.

Digital image analysis relates the pore structure to variations in acoustic velocity (Weger et al., 2009). In this method, the DOMsize taken at the 50% cumulative size is a quantitative measure of the predominant pore size of a given thin section. The complexity of the pore is measured by the perimeter of the area occupied by all pores divided by the pore area (PoA). Rocks with large simple pores are acoustically fast while rocks with small simple pores are slow at a similar porosity (Weger et al., 2009). The reef rocks of this study generally all have simple pore geometry (low PoA) but vary in size (Figure 5). As a result, the correlation between the DIA parameters and the acoustic velocity is less useful with respect to PoA and limited to DOMsize, which shows a slight correlation with velocity.

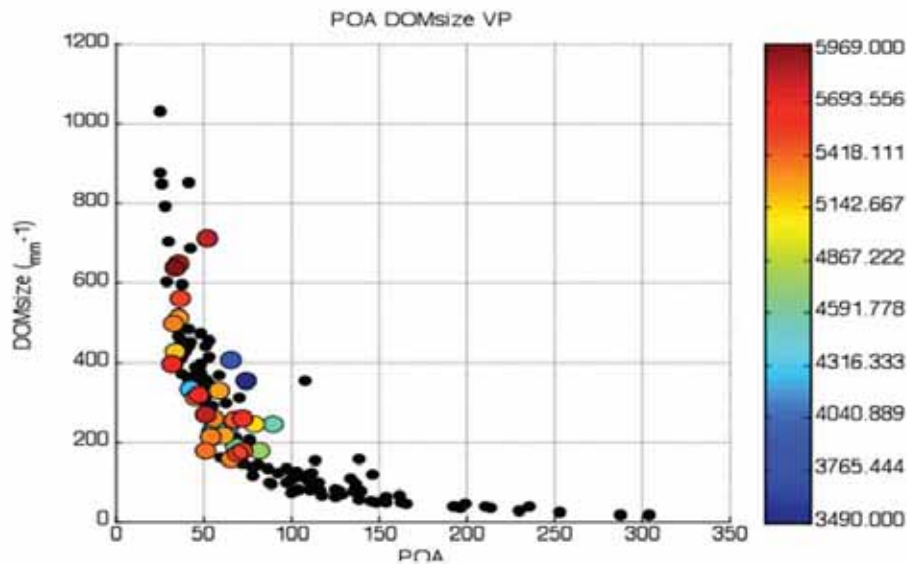


Figure 5. Plot between POA and DOMsize with Vp superimposed in color. Samples from this study are in color, while the black dots are the samples from Weger et al., (2009). The reef rocks tend to have simple pore structure but with a large range in size.

Conclusion

The various facies of the reef system in the Dominican Republic have high acoustic velocities that are the result of stiffness provided by the frame but also by extensive early marine and subsequent meteoric cements. The pore structure of the reef system is generally simple but has variable pore sizes. Thus, the DIA parameters do not provide a good correlation with the acoustic velocity.

References

- Anselmetti and Eberli, 1993, Controls on Sonic Velocity in Carbonates, Pure and Applied Geophysics, 141,287-323.
- Jordan, C and Wilson, J.L., 1998 Reefs: Geologic considerations for geophysicists, The Leading Edge, no.3, p. 325-328
- Weger, R.L, Eberli, G.P., Baechle, G.T., Massafero, J.L., Sun,Y.F., 2009, Quantification of pore structure and its effect on sonic velocity and permeability in carbonates, AAPG Bulletin v. 93, p. 1297-1317

Isotope Signature as a Tool for Meteoric Diagenesis

Yulaika Hernawati, Don McNeill, Jim Klaus, Gregor P. Eberli, & Peter K. Swart

Key Findings

- The carbon isotopic composition of bulk sediments varies relative to the stratigraphy and the diagenetic alteration of the sediments.
- Subaerial diagenesis produces a wide range of $\delta^{13}\text{C}$ and a narrow range of $\delta^{18}\text{O}$ values.

Introduction

The Pleistocene reef terraces of the Southern Dominican Republic extend back over the past 1.8 Ma and have been subsequently exposed and subject to several episodes of meteoric diagenesis. These diagenetic overprints give a great opportunity to understand the meteoric diagenetic history of Caribbean reef cycles. Furthermore, this understanding will be useful in reconstructing the depositional history of this suite of sediments and ultimately in understanding Pleistocene sea-level history.

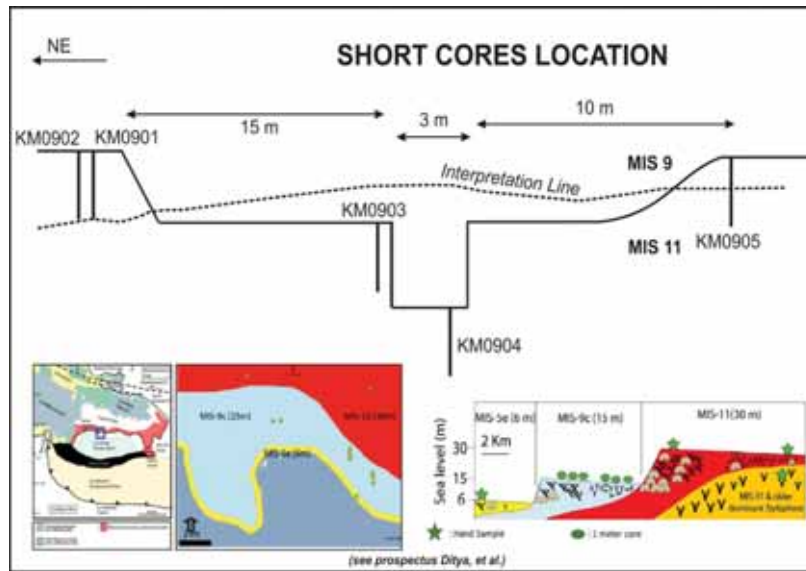


Figure 1. Short cores were taken from different intervals tentatively dated as MIS-9 and 11. Lower left depicts a regional geological map and right a continuously progressive carbonate section from MIS-5e to MIS-11 in S-N direction.

Data Analysis and Result

The geochemical data reported here results from five of 14 short cores collected (Figure 1). Additional analyses will be conducted on numerous deep cores (>30 m) which have been taken through Stage 5, 7, and 9 reef terraces. All of the short cores were taken from

Methods

A series of eight short cores were taken from a series of reef terraces which formed during glacial stage 9 to 11. In addition, three cores, 0 to 50 m in length were taken through reefs which formed during glacial stage 5, 7, 9 and 11. The split cores were drilled with a sample interval of 1 to 2 cm. The resultant samples were analyzed using X-ray diffraction and stable isotope mass spectrometry.

the 15 m terrace. The short cores of KM0901 and KM0902 were close to each other. KM0905 is interpreted to be the same age as KM0901 and KM0902 while KM0903 and KM0904 are considered to be older than those cores.

Stable isotope analysis produced a wide range of carbon isotopic values and a narrow distribution of oxygen isotopic values (Figure 2). This distribution is characteristic of meteoric diagenetic processes (Allan & Matthews, 1982). KM0901, KM0902 and KM0905 are estimated to be younger in age than KM0903 and 04, and contain both aragonite and calcite. Other cores, KM0903 and 04, do not have aragonite and calcite is the dominant mineral. This shows that KM0903 and 04 have undergone longer meteoric diagenesis than the younger cores. The plot of $\delta^{18}\text{O}$ against $\delta^{13}\text{C}$ for those cores shows that core KM0904 has the lightest oxygen isotopic values when compared to cores KM0901/2/3.

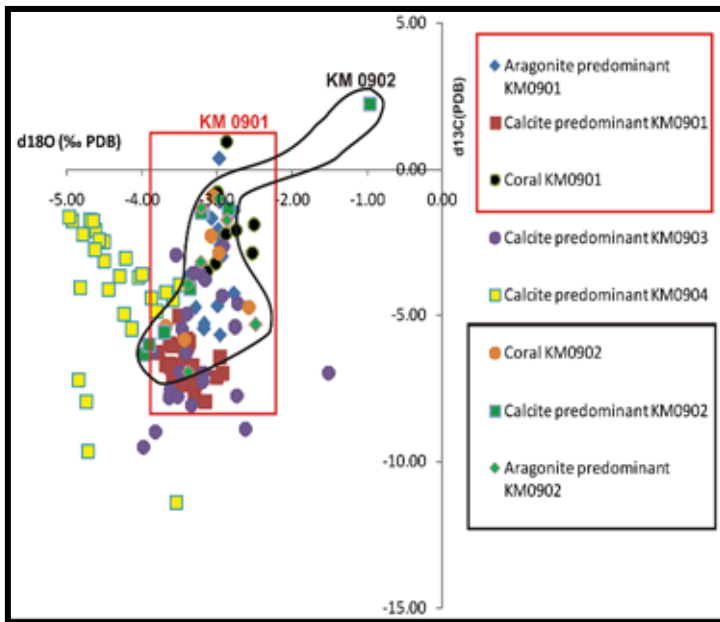


Figure 2. The wide variability in Carbon isotopic values and narrow variability in Oxygen isotopic values are characteristic of subaerial diagenetic (Allan & Matthews, 1982). Core KM0904 exhibits lighter oxygen isotope values than the three other cores.

that core KM0904 has the lightest oxygen isotopic values when compared to cores KM0901/2/3.

In core KM0901, heavier carbon isotopic values are correlated by the predominance of aragonite. As the aragonite content decreases, the carbon values become isotopically lighter. The most negative carbon isotopic values are associated with sub-aerial exposure surfaces. This kind of isotopic signature is typical of meteoric diagenesis (Allan & Matthews, 1982). Since this core intersected only a short time interval there were presumably no significant changes in the depositional processes.

Implication and Future Works

- The correlation between carbon isotopic composition of bulk sediment and stratigraphy shown by isotopic values (C and O) and mineralogy content shows promise for future meteoric diagenetic studies of deep cores taken through the Pleistocene Reef terraces of the Southern Dominican Republic.

References

Allan, J.R., and Matthews, R.K., 1982. Isotope signature associated with early meteoric diagenesis. *Journal of Sedimentology* 29, 797-817.

Large carbon isotopic changes preceding Pleistocene glaciations cast doubt on Neoproterozoic Snowball Earth Interpretations

Peter K. Swart and Martin J. Kennedy

Key Findings

- Similar magnitude changes in the $\delta^{13}\text{C}$ occur prior to both Neoproterozoic and Pleistocene glaciations. In the Neoproterozoic glacial successions the $\delta^{13}\text{C}$ values are widely interpreted to record a dramatic series of global environmental and evolutionary events including the snowball Earth and ocean stratification.
- Like the Neoproterozoic, the preglacial Pleistocene carbon isotope excursions are systematic, reproducible from section to section, and are of a similar 10‰ magnitude.
- In contrast to the Neoproterozoic, however, these excursions are not interpreted to be records of the global carbon cycle because they are at odds with the marine pelagic record even though the records are synchronous.
- We show that the high magnitude negative $\delta^{13}\text{C}$ and $\delta^{18}\text{O}$ of the Neoproterozoic carbonates associated with glacio-eustatically influenced intervals are similar in both the Quaternary and Neoproterozoic and suggest that the Neoproterozoic intervals share a common diagenetic origin to geochemical process which have been documented and are well constrained in the Pleistocene.

Abstract

Large and systematic shifts in the $\delta^{13}\text{C}$ values ($>12\text{‰}$) of carbonate dominated rocks preceding Neoproterozoic glacial successions are widely interpreted to record a dramatic series of global environmental and evolutionary events including the snowball Earth and ocean stratification (Maloof et al., 2010). In addition the variations themselves are the principal basis for global correlations on which the present global stratigraphic framework for the Neoproterozoic is based. The reproducibility of these $\delta^{13}\text{C}$ values from basin to basin, systematic shape and common position relative to glacial intervals is taken as evidence for a globally synchronous marine origin for these values that records changes in the global carbon cycle, however, direct evidence that these events are global and synchronous is lacking. In contrast to the Neoproterozoic, Quaternary deep-sea sediments provide an extremely well constrained record of the extent, magnitude and timing of changes in the global carbon cycle. Both the Neoproterozoic and the Quaternary have experienced large changes in sea level caused by glaciations, and the effect of these sea-level changes during the Pleistocene upon shallow-water carbonates has been to produce an intensively diagenetically altered rock leaving similar $\delta^{13}\text{C}$ and $\delta^{18}\text{O}$ stratigraphic records at globally disparate locations (Allan and Matthews, 1982; Melim et al., 2004; Quinn, 1991). Like the Neoproterozoic, the preglacial Pleistocene carbon isotope excursions are systematic, reproducible from section to section, and are of a similar 10‰ magnitude. In contrast to the Neoproterozoic, however, these excursions are not interpreted to be records of the global carbon cycle because they are at odds with

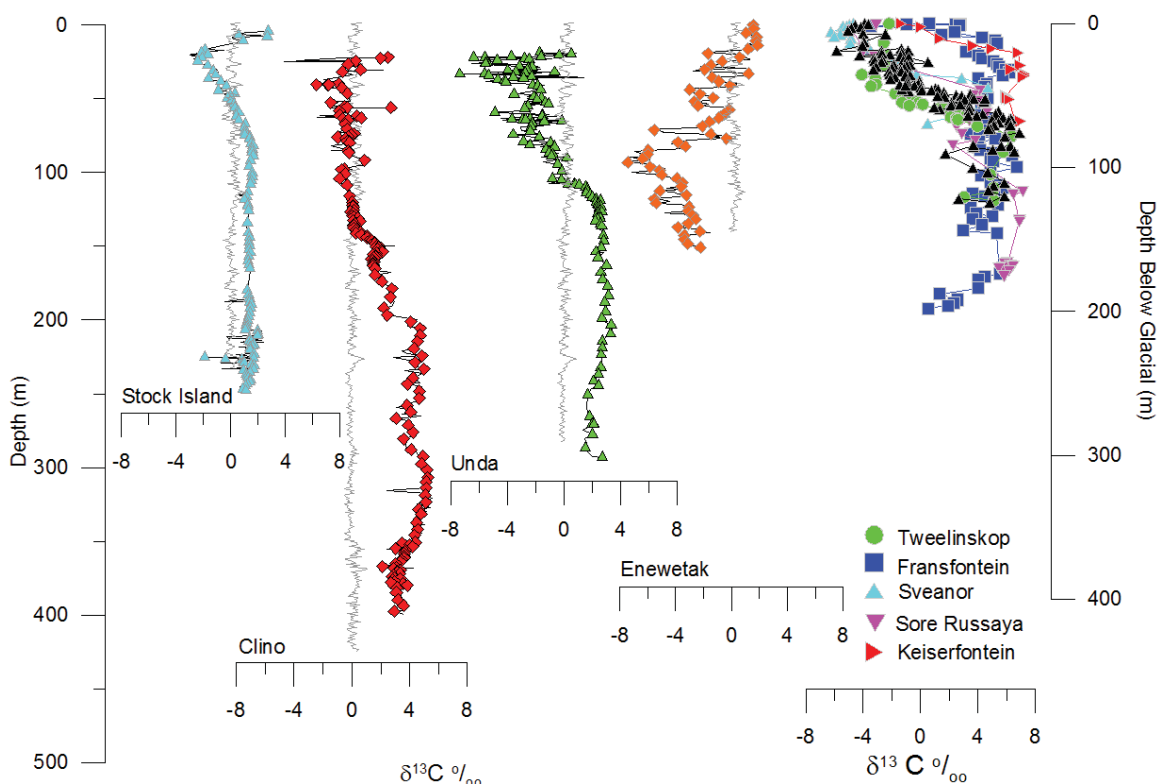


Figure 1: Comparisons of the carbon isotopic records of four Plio-Pleistocene aged cores taken in shallow-water carbonate platform material from the Caribbean and the Pacific Plio-Pleistocene with the oceanic record. All the shallow-water cores show substantial changes with depth reflecting alteration by freshwater. These changes are similar in both the Pacific and Atlantic and bear no resemblance to the oceanic record (grey line behind each data set). Slight differences in the nature of the profiles as a function of depth relate to differences in the rate of sedimentation. Neoproterozoic data are taken from various sources and show a pattern very similar to that seen in the Plio-Pleistocene records.

the marine pelagic record even though the records are synchronous. We show that the high magnitude negative $\delta^{13}\text{C}$ and $\delta^{18}\text{O}$ of the Neoproterozoic carbonates associated with glacio-eustatically influenced intervals are similar in both the Quaternary and Neoproterozoic and suggest that the Neoproterozoic intervals share a common diagenetic origin to geochemical process which have been documented and are well constrained in the Pleistocene.

A primary marine versus diagenetic origin for these and other negative $\delta^{13}\text{C}$ excursions has been argued for based on several lines of evidence that include: 1) the reproducibility of the negative isotope excursion in multiple Neoproterozoic basins; 2) the stratigraphic occurrence beneath glacial deposits that are assumed to be of similar age (based largely on the isotope values); 3) the reproducibility of isotopic excursion in some basins along strike, 4) that imperviousness of $\delta^{13}\text{C}$ values to alteration after deposition as a result of the thick carbonate successions which buffer C isotope values and would

therefore require an impossible volume of pore fluids to alter isotope values (Halverson et al., 2005; Kaufman and Knoll, 1995; Macdonald et al., 2010; Maloof et al., 2010) and insufficient organic carbon is present within sediment to alter isotopic values significantly (Halverson et al., 2005); 5) Finally, it is widely viewed that the unique nature of the Neoproterozoic $\delta^{13}\text{C}$ values argue for a primary origin recording a very different carbon cycle when compared to the Phanerozoic record. Here we show that almost identical features characterize Quaternary shallow water carbonate successions in which better time control and detailed study demonstrate that the variations in $\delta^{13}\text{C}$ values are the product of mixing of modern sediments and those which have been altered very early in their history and do not constrain the global carbon cycle.

As a basis for comparison we present records from three cores in the Bahamas and Florida and one from the Pacific for which the $\delta^{13}\text{C}$ and $\delta^{18}\text{O}$ data have been published previously (Melim et al., 2004; Quinn, 1991). The sediments at these locations were deposited during the Pliocene and Pleistocene and consist of skeletal and non-skeletal derived sediments. Each of the cores were subjected to repeated sea-level changes leaving a section of rocks up to 100 m thick in some cases with highly depleted $\delta^{13}\text{C}$ and $\delta^{18}\text{O}$ values overlying a section with relatively positive $\delta^{13}\text{C}$ values similar to the Neoproterozoic Trezona anomaly (Figure 1). The pattern of $\delta^{13}\text{C}$ and $\delta^{18}\text{O}$ changes in these cores can be succinctly described by the model proposed by Allan and Matthews (Allan and Matthews, 1982). Upper portions of the cores, which are composed on modern non-skeletal sediments most similar to Neoproterozoic allochems, have $\delta^{13}\text{C}$ values as high as +6‰ in the Bahamas. In the Pacific, where the sediments are mainly skeletal in nature, values only reach $\delta^{13}\text{C}$ values of +2 ‰.

Regardless of the reasons suggested by proponents of a marine origin for the $\delta^{13}\text{C}$ signal in the Trezona anomaly, there is evidence supporting a diagenetic origin. First, during the Neoproterozoic glaciations there can be no debate that sea level must have been significantly lower thus exposing shallow-water carbonate platforms to meteoric diagenesis. The similar record of $\delta^{13}\text{C}$ change in Plio-Pleistocene shallow-water carbonates in the Pacific and the Atlantic clearly speaks to this point. Not only can changing sea level produce sediments in platform derived carbonates with similar $\delta^{13}\text{C}$ values which are unrelated to the global carbon cycle, but diagenetic changes, through the evitable development of meteoric vadose, phreatic, and mixing zones which accompany global scale changes in sea level, will produce similar geochemical records on a global scale. A second line of evidence is provided from the $\delta^{18}\text{O}$ value of Neoproterozoic carbonates, routinely ignored in most studies and assumed to be a product of later burial diagenesis. In the diagenetically altered Plio-Pleistocene sections, $\delta^{13}\text{C}$ and $\delta^{18}\text{O}$ values of carbonates co-vary when carbonates reprecipitate (stabilize) from a fluid comprised of both marine and meteoric sources. Where the $\delta^{18}\text{O}$ of the carbonates are influenced only by meteoric fluids, or by the thermal kinetic effects associated with burial diagenesis, then the $\delta^{13}\text{C}$ and $\delta^{18}\text{O}$ values are unrelated. While in many Neoproterozoic sections, co-variation similar to the Plio-Pleistocene are evident, there are also sections in which no co-variations are present. An absence of co-variation between these two isotopes in the Neoproterozoic is often taken as evidence of a diagenetic effect (Halverson et al., 2002), yet the truth is that Plio-Pleistocene diagenesis also often fails to produce co-variation.

Another final argument suggested in favor of the primary origin of the $\delta^{13}\text{C}$ signals in Neo-Proterozoic carbonates is that their extreme range of values is not matched in more recent examples. It is true that Plio-Pleistocene carbonates do not reproduce exactly the same magnitude of change, but the ranges are not as dissimilar as suggested. For example, modern non-skeletal sediments in the Bahamas have $\delta^{13}\text{C}$ values as positive as +6‰, only 2 to 3‰ more negative than typical maximum values reported for the Trezona anomaly in Neo-Proterozoic sections. This difference could be associated with a modest secular change of $\delta^{13}\text{C}$ consistent with Phanerozoic sea water variation. The most depleted $\delta^{13}\text{C}$ values for bulk samples in the Pleistocene are -8 to -10‰, values, once again not vastly different when compared to the Trezona. Most importantly, both the Plio-Pleistocene and Neoproterozoic examples presented here (Figure 1) record a similar progression between the most positive to negative $\delta^{13}\text{C}$ values of similar magnitude.

References

- Allan, J.R. and Matthews, R.K. 1982. Isotope signatures associated with early meteoric diagenesis. *Sedimentology*, 29: 797-817.
- Halverson, G.P., Hoffman, P.F., Schrag, D.P. and Kaufman, A.J. 2002. A major perturbation of the carbon cycle before the Ghaub glaciation (Neoproterozoic) in Namibia: Prelude to snowball Earth? *Geochemistry Geophysics Geosystems*, 3: NIL_22-NIL_45.
- Halverson, G.P., Hoffman, P.F., Schrag, D.P., Maloof, A.C. and Rice, A.H.N. 2005. Toward a Neoproterozoic composite carbon-isotope record. *Geological Society of America Bulletin*, 117: 1181-1207.
- Kaufman, A.J. and Knoll, A.H. 1995. Neoproterozoic variations in the C-isotopic composition of seawater - Stratigraphic and biogeochemical implications. *Precambrian Research*, 73: 27-49.
- Macdonald, F.A., Schmitz, M.D., Crowley, J.L., Roots, C.F., Jones, D.S., Maloof, A.C., Strauss, J.V., Cohen, P.A., Johnston, D.T. and Schrag, D.P. 2010. Calibrating the Cryogenian. *Science*, 327: 1241-1243.
- Maloof, A.C., Ramezani, J., Bowring, S.A., Fike, D.A., Porter, S.M. and Mazouad, M. 2010. Constraints on early Cambrian carbon cycling from the duration of the Nemakit-Daldynian-Tommotian boundary $\delta^{13}\text{C}$ shift, Morocco. *Geology*, 38: 623-626.
- Melim, L.A., Swart, P.K. and Eberli, G.P. 2004. Mixing-zone diagenesis in the subsurface of Florida and The Bahamas. *Journal of Sedimentary Research*, 74: 904-913.
- Quinn, T.M. 1991. Meteoric Diagenesis of Plio-Pleistocene Limestones At Enewetak Atoll. *Journal of Sedimentary Petrology*, 61: 681-703.

The Determination of Leakage of Carbon Dioxide from Reservoirs Using Cavity Ring Down Spectrometry

Ben Galfond, Dan Riemer, and Peter K. Swart

Key Points

- Cavity ring down spectroscopy (CRDS) has the potential to supplant isotope ratio mass spectrometry in a number of different fields of research and industry.
- While the CRDS' stability may decrease the need for constant calibration, great care must be taken when selecting and creating the standards to be used.
- The numerous variables in the sample's matrix can have significant effects on the accuracy of the CRDS.

Background

Recently, advances in optical spectroscopy techniques have begun to supplement traditional isotope ratio mass spectrometry (IRMS) techniques as a means of measuring $\delta^{13}\text{C}$. These units are the size of an office computer and can make high precision $^{13}\text{C}/^{12}\text{C}$ determinations on atmospheric samples every 5 to 10 seconds. Hence ease of use, small size, portability, as well as low cost, have made cavity ringdown spectroscopy (CRDS) an increasingly appealing alternative to traditional IRMS methods. We intend to use these devices to measure and identify possible leakage of CO_2 sequestered in old oil reservoirs. This is part of a department of Energy project design to verify carbon capture and storage. Our initial experiences with two Picarro G1101-*i* CRDS analyzer for isotopic CO_2 show instrument accuracy to be influenced by the composition of the gas. Samples composed of varying nitrogen-oxygen ratios or different humidity levels, as well as those with helium were all subject to a linear deterioration in the accuracy of the instruments. A severe CO_2 concentration dependence was also observed. These issues will be important for scientists using the CRDS in a range of environments, for example in examining soil gas samples, as well as those using the CRDS as a detector interfaced to preparative instrumentation that may cause variations in the sample matrix that must be taken into consideration.

Best Practice for Acquisition, Processing, and Interpretation of 3D GPR Data to Visualize Deformation Bands, Fractures, and Karst in Carbonates

Mark Grasmueck and Pierpaolo Marchesini

Key Findings

- Very dense 3D GPR data acquisition of 5cm for 200MHz antennae enables super-resolution imaging of fractures and Karst.
- Diffractions are caused by sub-wavelength discontinuities like corners, edges and small voids, the basic constituents of fractures and Karst
- Combined reflection and diffraction GPR imaging visualizes joints, faults and karst in any orientation in 3D volumes with side lengths of tens of meters at centimeter resolution.

Introduction

While fractures (faults, joints, deformation bands) and karst play an important role for fluid flow in many carbonate reservoirs, their accurate characterization from seismic and well data is limited due to resolution limits and geometrical complexity. Outcropping reservoir analogues offer an additional source of information. However exposure on only a few vertical walls and horizontal surfaces in combination with superficial alteration prevent the extraction of accurate three-dimensional fracture and karst networks. To overcome this observational gap the CSL has successfully applied 3D Ground Penetrating Radar (GPR) in combination with conventional outcrop mapping to both tight and porous fractured and karstified reservoir analogues. These field studies have shown that GPR can three-dimensionally image complex fracture and karst configurations in unprecedented resolution and clarity. This paper summarizes the key factors for achieving the good GPR results: 1) GPR antenna frequency and site selection, 2) Very dense 3D GPR data acquisition, 3) Relative amplitude preserving 3D migration processing, and 4) Discontinuity and diffraction visualization and interpretation.

2D GPR Reconnaissance Survey for Antenna Frequency and Site Selection

As GPR works best in non-conductive environments, clay content and saline pore water prevent the deep propagation of electromagnetic waves. Previously acquired GPR data or electrical conductivity measurements on rock and water samples can be used for a preliminary assessment of the suitability of field sites for GPR imaging.

When arriving at a new field location and doing a site walkthrough for visual inspection, a GPR antenna is towed along for immediate assessment of GPR data quality and depth penetration on the field laptop screen. Radar data are acquired at regular distance intervals using an odometer wheel. With a sub-meter precision GPS receiver the path of the GPR antenna is plotted in real-time on aerial- or satellite imagery. Some of the initial scans can be repeated with a different antenna frequency in order to assess the

relationship between GPR investigation depth and resolution. Figure 1 shows a comparison of 100MHz, 200MHz and 500MHz antennae typical for clayfree carbonates. In our experience, 200-250 MHz antennae offer a good compromise between depth and resolution for fracture and karst imaging.

The 2D GPR profiles acquired during the reconnaissance survey give a field scale stratigraphic site overview and are used for correlation of separated outcrops. Site accessibility, data quality, and representation of stratigraphic intervals within the GPR depth range are the main criteria to determine locations suitable for detailed 3-D GPR imaging. Several such 2D GPR reconnaissance surveys at different locations within a field area can be completed in a day. By comparison of the different locations potential 3D GPR sites are ranked together with the scientific objectives of the reservoir analog outcrop study.

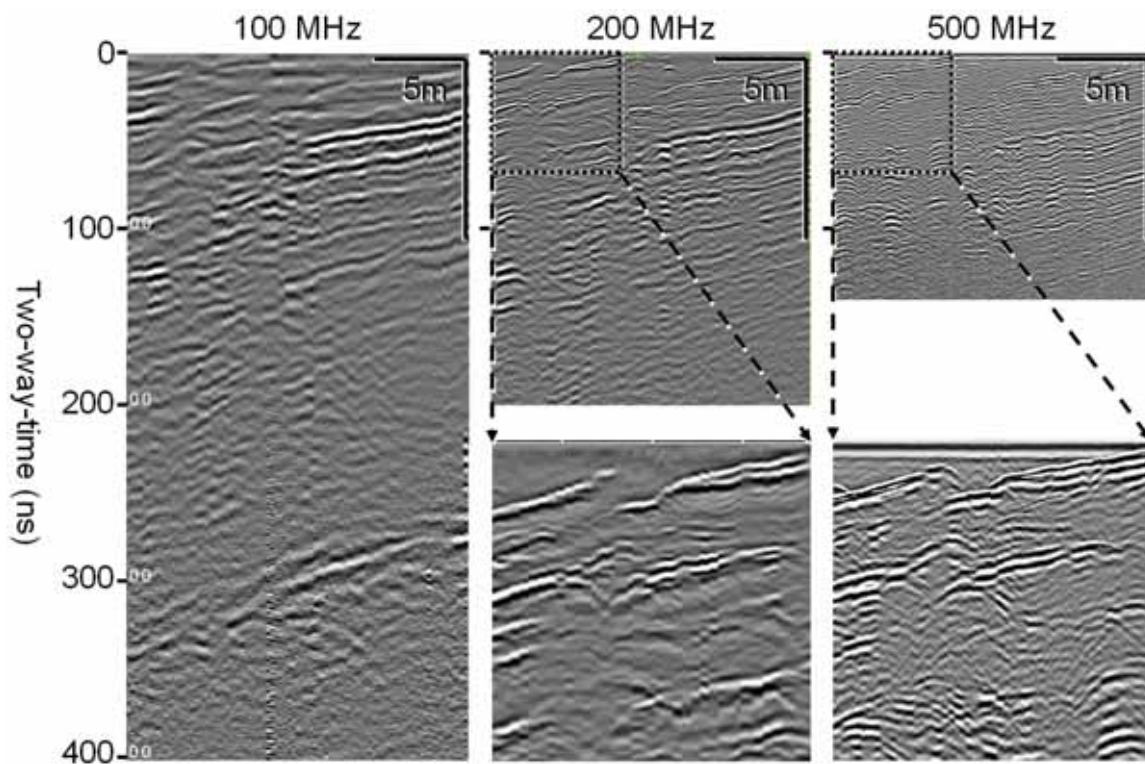


Figure 1: Comparison of gained but unmigrated GPR data recorded with 100 MHz, 200 MHz, and 500 MHz antenna. The profiles were acquired in 2008 and 2009 along the same line in the Madonna della Mazza Quarry imaging dipping stratigraphy and diffractions from fractures. The 100 MHz data provide subsurface information to a maximum two-way-time of 400ns. Data range decreases to 200ns for the 200 MHz antenna and to 140ns for the 500 MHz antenna. Insets are zoomed data portions to show details of resolution available from the higher frequency antennae.

Very dense 3D GPR Data Acquisition to sample High Frequency GPR Signals

For full-resolution 3D GPR imaging quarter wavelength spatial sampling of the GPR signals is a basic requirement (Grasmueck et al, 2005). Until recently we have chosen GPR profile spacing as a quarter wavelength of the center antenna frequency. For the 250MHz antenna and a typical subsurface radar velocity of 0.1m/ns, profile spacing used

to be 0.1m. Experiments in the Madonna della Mazza quarry show halving the trace spacing to 0.05m leads to a dramatic improvement in imaging of both shallow (< 1 m depth, Figure 2) and deeper (several meters depth) fractures (Marchesini and Grasmueck, 2010). Reason for the improved imaging is that the high frequency component of the GPR signals containing high resolution information is properly sampled and used for fracture imaging. Additionally all fracture orientations are imaged equally well. With the previous wider grid spacing, GPR profiles had to be oriented parallel to the dominant dip direction. The denser trace spacing allows the choice of the most practical survey line orientation and therefore simplifies 3D survey design and acquisition. Drawback of the very dense trace spacing is a doubling of acquisition effort and the requirement for increased antenna positioning accuracy. We have solved this problem by utilizing a dual antenna GPR system and a Rotary Laser Positioning system with 4 laser transmitters automatically guiding the antenna operator along the survey lines with two LED arrays (Grasmueck and Viggiano, 2007). In summary, the optimum profile spacing for full-resolution 3D imaging of fractures including the high frequency spectral content is: 0.025m for the 500MHz, 0.05m for the 200MHz, and 0.1m for the 100MHz Antenna. A typical 3D survey size acquired per day with dual 200 MHz antennae is 1000m², yielding 400'000 GPR traces or 1GB of data.

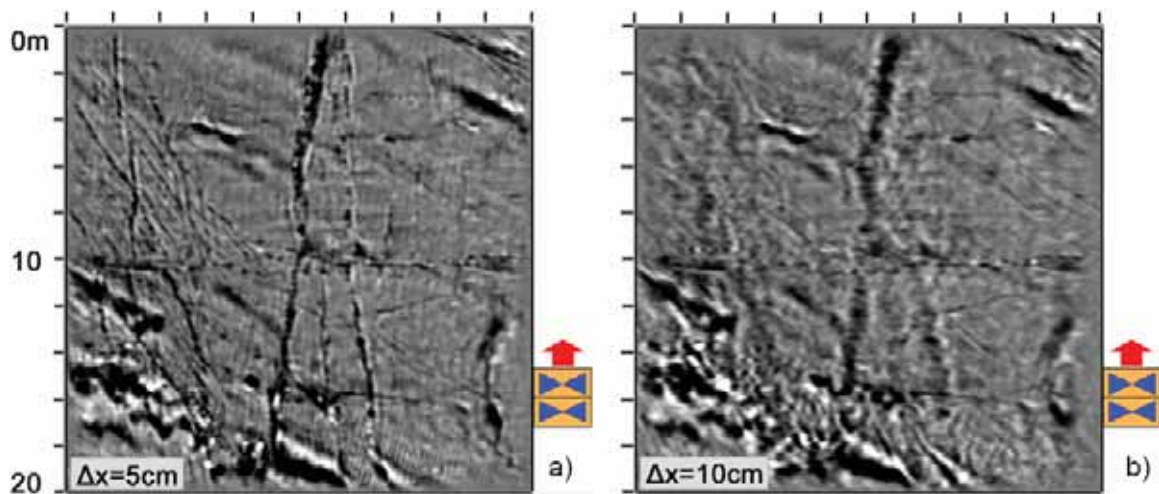


Figure 2: Horizontal slice extracted from migrated 250 MHz 3D GPR data cubes imaging deformation bands and faults in the Madonna della Mazza Quarry. **a)** 0.05m line spacing produces a clear image of fractures at all orientations. **b)** Acquisition with 0.1m linespacing causes severe degradation of fractures oriented parallel to the acquisition direction. Red arrow shows the GPR acquisition direction.

Relative amplitude preserving 3D migration processing

Main reason for the very dense 3D acquisition grid is the nonaliased sampling of diffractions. Diffractions are caused by sub-wavelength discontinuities such as corners, edges and small cavities and therefore are abundant in fractured and karstified carbonates. Diffractions have a hyperbolic cone shape, and appear as circles in horizontal slices (Figure 3a). The 3D migration process sums up diffraction amplitudes along hyperbolic trajectories and focuses the energy in the apice, the location of the sub-wavelength scatterer. With very dense data acquisition the maximum amount of

diffracted energy including far-offsets is recorded and 3D migrated. Before migration a dewow filter, time zero correction, gain, and background removal are applied. Time zero correction also includes an NMO stretch to account for the offset between transmitter and receiver. The gain function is based on the average energy decay curve computed over the entire survey to preserve relative amplitudes.

The 3D migration with the 3D phase shift algorithm and 90° aperture uses a constant velocity. The 90° aperture is necessary as the far-offset diffraction tails have an apparent dip near 90°. The initial migration velocity is based on hyperbolic moveout analyses of diffraction cones at different depths in the unmigrated 3D GPR volumes. The velocity value is then optimized by visually checking the quality of diffraction focusing throughout the 3D volume. The 3D migrated GPR data are exported in SEG-Y format for 3D visualization and interpretation e.g. in Geoprobe.

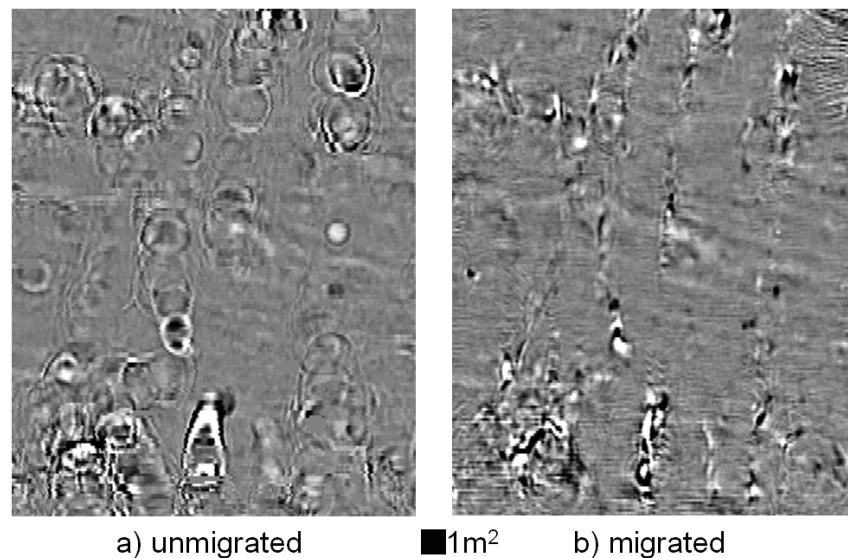


Figure 3: Topviews of 3D GPR cube acquired in the Solvay Quarry, Cassis (France): **a)** Unmigrated horizontal slice extracted at 1.95 m depth with abundant diffraction circles. **b)** 3D migration: Focuses diffrascions line up in fracture planes and cluster in karst features.

Visualization and Interpretation of Fractures and Karst.

Imaging of fractures and karst in full-resolution 3D GPR data can be subdivided in three main categories:

1) *Coherent reflections from subhorizontal deformation bands, joints and faults*

The imaging principle is similar as for continuous stratigraphic horizons. The maximum dip of fractures imaged is approximately 60-70 degrees and depends on the radiation angle of the GPR antenna. Modelling and field examples have shown that millimeter aperture fractures can be detected with 100 MHz Antennae if water or air filled. (Lane et al., 2000, Grasmueck, 1996). Our GPR work in the Madonna della Mazza Quarry has shown that cm thick deformation bands consisting of crushed and densely packed grains provide a sufficient electromagnetic contrast to generate detectable GPR reflections (Marchsini et al., 2008). With conventional horizon interpretation tools the fractures can be picked to build the fracture network. This type of fracture imaging does

not resolve subvertical fracture orientations. Also continuous fracture planes can be rare in outcrops with pervasive structural deformation. Field sites best suited for this type of fracture imaging contain few slightly dipping or horizontal fracture planes.

2) Fault imaging by stratigraphic reflection displacements

This type of fracture imaging is also well known from seismic imaging. Fracture network visibility and interpretability can be dramatically improved with semblance or coherency based attributes. This method works best in relatively undisturbed environments with clear subhorizontal stratigraphic reflections. The Madonna della Mazza quarry is a good example (Seki et al., 2009). However this method relies on the vertical displacement (i.e. faults) of subhorizontal stratigraphic reflectors. Seismic and GPR resolution theory show that a vertical displacement has to be at least quarter wavelength to be resolved. For 250 MHz GPR data the minimum detectable fault displacement is therefore around 10 cm. The main disadvantage of this method is that joints with no displacement are not imaged.

3) Delineation of Fractures and Karst by Diffractions

As diffractions originate from small sub-wavelength discontinuities they can be used to image very small features in the subsurface. Based on theoretical analysis and synthetic modeling studies, this type of imaging has been termed as super-resolution in reflection seismic (Moser and Howard, 2008). There are practically no reflection seismic field data acquired dense enough to fully sample diffractions. Current seismic acquisition and processing practice suppresses diffracted energy as it is undersampled and interferes with coherent reflections.

Our very densely sampled 3D GPR data show that diffractions can be used to image fractures and karst. The 3D phase shift migration collapses the diffractions into small points aligned in fracture planes (Figure 3b). Rapid vertical animation of horizontal slices visualizes the alignments. The discontinuities are small scale broken edges and corners developed in the rock volume due to joints and faults. For example, the Cassis Quarry with intense structural deformation contains mostly vertical joints and only few stratigraphic reflections. At this field site full-resolution 3D GPR diffraction imaging was the only method able to delineate all subsurface fracture sets.

Also in the Cassis 3D GPR data there are localized clusters of high amplitude diffractions. Many of these diffraction clusters occur at the intersection of multiple fracture sets. Corroborated by outcrop observation these zones are interpreted as karst features. The high amplitude of the diffractions is caused by the contrast between air and rock defining karstic voids. The unipolar (only positive) RMS amplitude attribute better visualizes karst than the dual polarity (positive and negative) GPR amplitudes. Volume rendering with low RMS amplitudes set to transparent visualizes the distribution of karst and prominent fractures. Geobody extraction on the RMS attribute volume automatically generates individual karst bodies for quantitative analysis of karst distribution (Figure 4). The connected body extraction is calibrated by comparing the karst geonomalies intersecting individual GPR profiles with the distribution and frequency of real karst features mapped in the adjacent outcrop (for further details see Pomar et al. 2010, this CSL extended abstract volume).

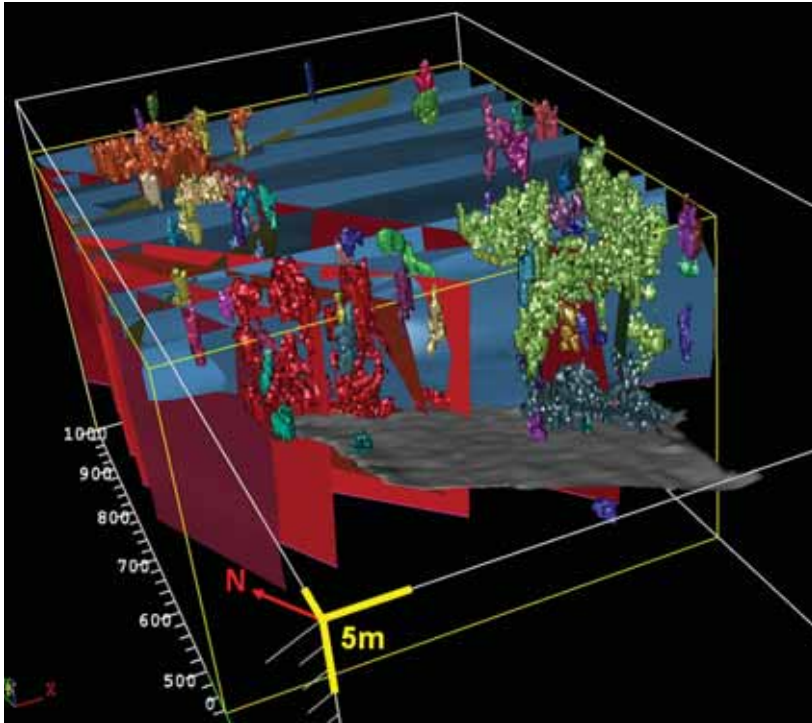


Figure 4: 3D view of interpreted vertical fracture planes and karst geoanomalies at the Cassis quarry. The blue fracture set and karst are limited by the SE dipping stratigraphic boundary shown in grey. Both karst and fracture interpretation are based on GPR diffraction imaging.

Conclusions

With 3D GPR surveys fully sampling the high frequency signal component, complex karst and all types of fractures including subhorizontal, subvertical deformation bands, joints, and faults can be imaged in unprecedented resolution. Our recent field studies at Madonna della Mazza and in Cassis show that such GPR diffraction imaging introduces a step change towards super-resolution imaging of carbonate reservoir analogues. As fractures and karst are among the most challenging imaging targets similar improvements can be expected in imaging of sedimentary structures, biogenic features, diagenetic patterns and stratigraphic complexities in other outcropping carbonate reservoir analogues. These complex features can now be investigated in 3D GPR volumes with side lengths of tens of meters at a resolution of a few centimeters.

References

- Grasmueck, M., 1996, 3D ground-penetrating radar applied to fracture imaging in gneiss: *Geophysics*, 61, 1050–1064.
- Grasmueck, M., R. Weger, and H. Horstmeyer, 2005, Full-resolution 3-D GPR imaging, *Geophysics*, 70, K12-K19, 2005.
- Grasmueck, M. and D.A. Viggiano, 2007, Integration of Ground-Penetrating Radar and Laser Position Sensors for Real-Time 3D Data Fusion, *IEEE Transactions on Geoscience and Remote Sensing*, Vol.45, no.1., 130-137.
- Lane J. W., M. L. Buursink, F. P. Haeni, and R. J. Versteeg, 2000, Evaluation of ground-penetrating radar to detect free-phase hydrocarbons in fractured rocks—results of numerical modeling and physical experiments: *Ground Water*, 38, 929–938.
- Marchesini, P., Grasmueck, M., Eberli, G.P., Sekti, R.P., and Coll, 2008, M. Fracture and Deformation Band Detection with 3D GPR, *CSL Annual Review 2008, Extended Abstracts*.
- Marchesini, P. and Grasmueck, M., 2010, Impact of Spatial Sampling and Antenna Polarization on 3D GPR Fracture Detection, Expanded Abstract, *Proceedings 13th International Conference on Ground Penetrating Radar*, June 21–25, 2010, Lecce, Italy.
- Moser T.J. and Howard C.B. 2008. Diffraction imaging in depth. *Geophysical Prospecting* 56, 627–642. doi:DOI: 10.1111/j.1365-2478.2007.00718.x
- Pomar, K., Eberli, G.P., Grasmueck, M., and Lamarche, J., 2010, Visualization and Quantification of Fracture-related Karst in Barremian Limestones, Cassis, France, *CSL Annual Review 2010, Extended Abstracts*.
- Sekti, R.P., Eberli, G.P. Grasmueck, M., Marchesini, P. and Coll, M., 2009, Sedimentology and Fracture Analysis using Ground Penetrating Radar (GPR) in Late Cretaceous Carbonates (Maiella, Italy), *CSL Annual Review 2009, Extended Abstracts*.

Visualization and Quantification of fracture-related karst in Barremian limestones, Cassis, France.

Kenri Pomar, Gregor P. Eberli, Mark Grasmueck, and Juliette Lamarche

Key Findings

- Karst of various sizes and shapes are observed along fracture planes in the Solvay quarry near Cassis. Karst occurs predominantly at the intersection of the fractures and areas with plenty of karst intersections tend to have large and extensive karst cavities.
- RMS amplitude attribute, volume rendering and automated geoanomalies extraction techniques of the migrated 200 MHz 3D GPR cubes visualize karst and fractures.
- Based on the 3D GPR data, karst cavities are up to 3.8% of the rock volume in the Solvay quarry.
- Small-sized karst features are more abundant than large-sized karst, following a power law size-frequency distribution.

Introduction

In carbonate strata, dissolution features often are associated with fractures either along fracture planes or as karst cavities in fracture corridors. Both fractures and karst play a major role in reservoirs: fractures strongly influence flow behavior while karst features influence flow and storage of hydrocarbons. Reservoirs of the Ellenburger Group in the Andector field, East Texas (Hoak et al., 1998), the Lower Ordovician Puckett field in west Texas (Loucks and Anderson, 1985) and the reservoirs in Tarim Basin (Guangpo et al., 2005) are proven or thought to be dominated by karst. Advanced seismic techniques can image large-scale karst features like the tower karst morphology in the Tarim Basin but the smaller-scale dissolution features along fault and bedding planes are beyond seismic resolution. In this study, 3D Ground Penetrating Radar (GPR) and outcrop observations in the Solvay quarry near Cassis in southern France visualize the distribution of fracture-related karst in three dimensions. This visualization allows the assessment of the karst size-frequency distribution and quantification of the dissolved rock volume by fracture-related karst in otherwise tight limestones.

The Solvay quarry (Figure 1A) is cut into fractured and karstified shallow-water carbonates of late Barremian age (Masse et al., 2003) in which the matrix porosity of the limestone is less than 1.8%. The quarry walls provide 2D information of the karst, including the size, shape, position relative to the stratigraphy, and the relationship between karst and fractures. The karst occurs predominantly along fracture planes and displays various sizes and shapes (Figure 1B).

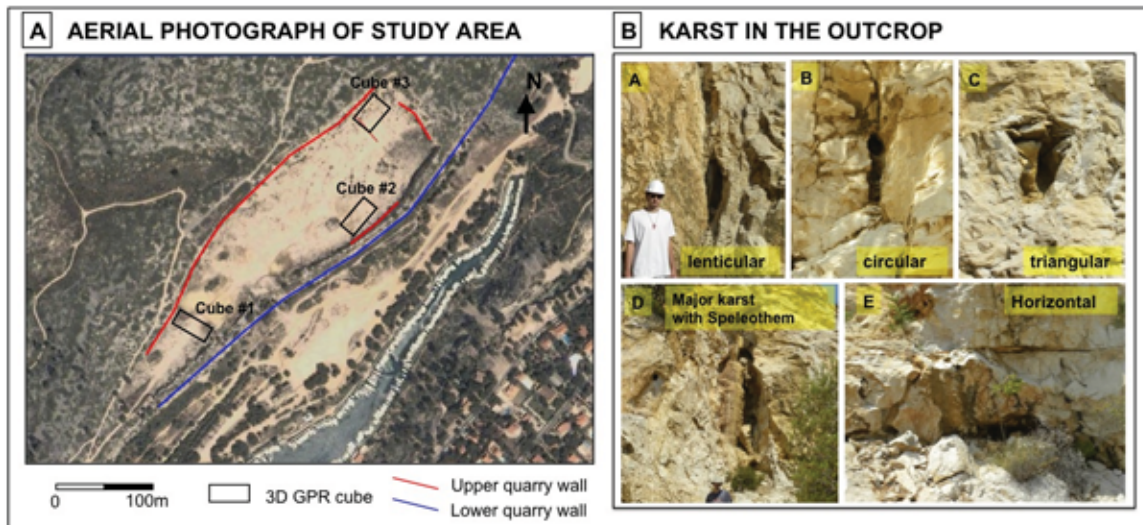


Figure 1. Solvay quarry near Cassis, France, has a NE – SW orientation and is approximately 500 m long and 100 – 200 m wide. A) Satellite image with the location of outcrop (the quarry wall) and the 3D GPR cubes. B) Various shaped and sized Karst are recognized along the fracture plane. A: lenticular shaped karst. B: circular karst. C: Triangular shaped karst. D: Big lenticular shaped karst with speleothem. E. Horizontal karst along bedding plane.

Method

Three 200 MHz 3D GPR cubes acquired on the quarry floor detect and image both fractures and karst in the shallow subsurface (GPR depth penetration is up to 12.5 m). The contrast between the massive limestone host rock and the open fractures and air-filled karst cavities produce strong diffractions of the electromagnetic signals. Innovative acquisition and processing techniques image the fractures and karst cavities in the 3D GPR cubes (see Grasmueck et al., CSL 2010 abstract). Signal attribute, volume rendering and automated geoanomalies extraction techniques available in the Geoprobe™ software are applied to the migrated 200 MHz 3D GPR cubes in order to enhance the visibility of karst and fractures. In particular, the root mean square (RMS) amplitude attribute helps visualize the karst bodies in the migrated GPR data. The window parameter used for the RMS amplitude attribute is determined iteratively based on knowledge obtained from outcrop observation. The 3D Volume Rendering technique isolates the karst by setting the low amplitude signals (of the RMS amplitude attribute) in the cubes transparent, hence preserving only the strong amplitude features which correspond to karst. (Figure 2).

The extraction of the karst from the 3D GPR volume allows the volume of individual karst bodies to be measured, using the automated geoanomalies extraction technique. The RMS amplitude attribute is the input volume and (karst) geobodies are extracted using quantitatively defined parameters such as: anomaly size limit and amplitude range parameters that define the size and amplitude range of strong amplitude anomalies. The results provide the volume of individual karst cavities as well as the distribution of karst in three dimensions.

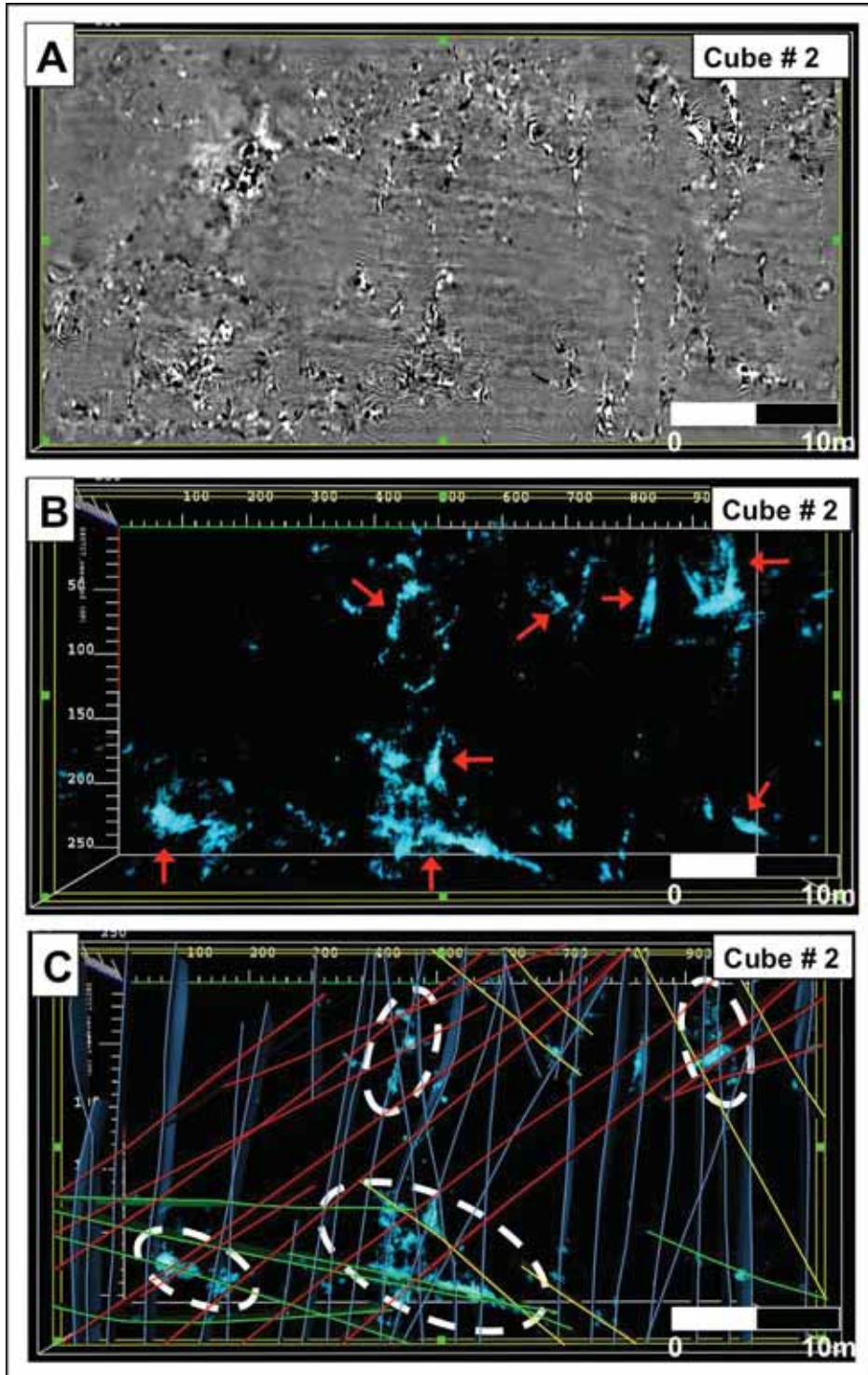


Figure 2. Visualization of karst in 3D GPR cube. A. Migrated 3D GPR amplitude cube. B. Semi-transparent volume rendering technique applied to the RMS amplitude attribute cube. The red arrows indicate cluster of strong amplitude diffractions that correspond to karst. C. Semi-transparent RMS amplitude cube with the fracture interpretation. Karst are preferentially located at the intersection of fractures (dashed white circles). The blue, red, green and yellow lines represent the NW-SE, N-S, NE-SW and E-W oriented fractures, respectively.

Karst Distribution

The distribution of karst in the 3D GPR cube is not uniform, but rather patchy. For example, the area in the middle of the cube #2 contains significantly more karst compared to the area on the lower right and upper left of the cube (Figure 2B). This patchiness is a direct result of increased dissolution at the intersection of fractures. In the middle of the cube three or four fracture families intersect while in the other areas only one or two fracture families are observed (Figure 2C). The occurrence of increased karst at fracture intersections is also observed in all three 3D GPR cubes acquired in the Solvay quarry.

Quantitative Analysis of the Karst

Automated geomanaly extraction provides the volume of individual karst bodies within the 3D GPR cubes. To test the accuracy of the extraction, the results were compared to the outcrop observations on the adjacent quarry wall. Cube#2 on the southeastern side of the quarry is located less than 20 m from a quarry wall. The wall exposes the same stratigraphic units that are imaged by GPR and the inlines of the 3D GPR cube are parallel to the quarry wall (Figure 3). The optimum parameters for the Karst anomaly extraction were iteratively determined by producing eleven pseudo GPR outcrop sections through the 3D GPR cube with intersecting karst anomalies and comparing them to the real outcrop image with observed karst features. As a result, 100 – 1,000,000 voxels size range and minimum amplitude of 5 proved to be the parameters to produce the best match when compared to the karst density in outcrop. The histograms displayed on Figure 4 show that the total karst surface area of the quarry wall falls within the range of total karst surface area of the 2D inlines, indicating that the volume extraction yields accurate results. Consequently, the same parameters are applied to the other 3D GPR cubes (cube #1 and #3).

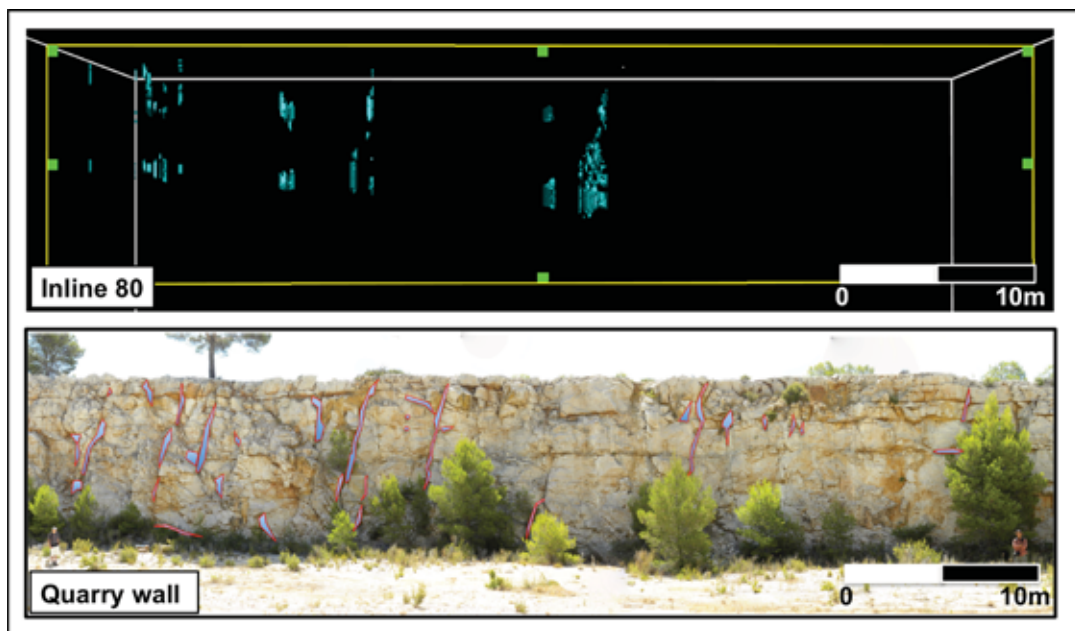


Figure 3. Comparison between karst on 2D inline of cube #2 (light blue) with karst on the adjacent quarry walls (red rectangles).

Based on the automated geonomalies extraction from all 3D GPR cubes, karst cavities contribute up to 3.8% porosity of the total volume of the strata in the Solvay quarry. Most of the dissolution forms vertical karst bodies (Figure 5A). This vertical geometry follows the near vertical orientation of the fracture planes (Pomar et al., 2009). The size-frequency distribution of karst in the quarry follows a power law distribution, indicating that small karst bodies are more common than large karst.

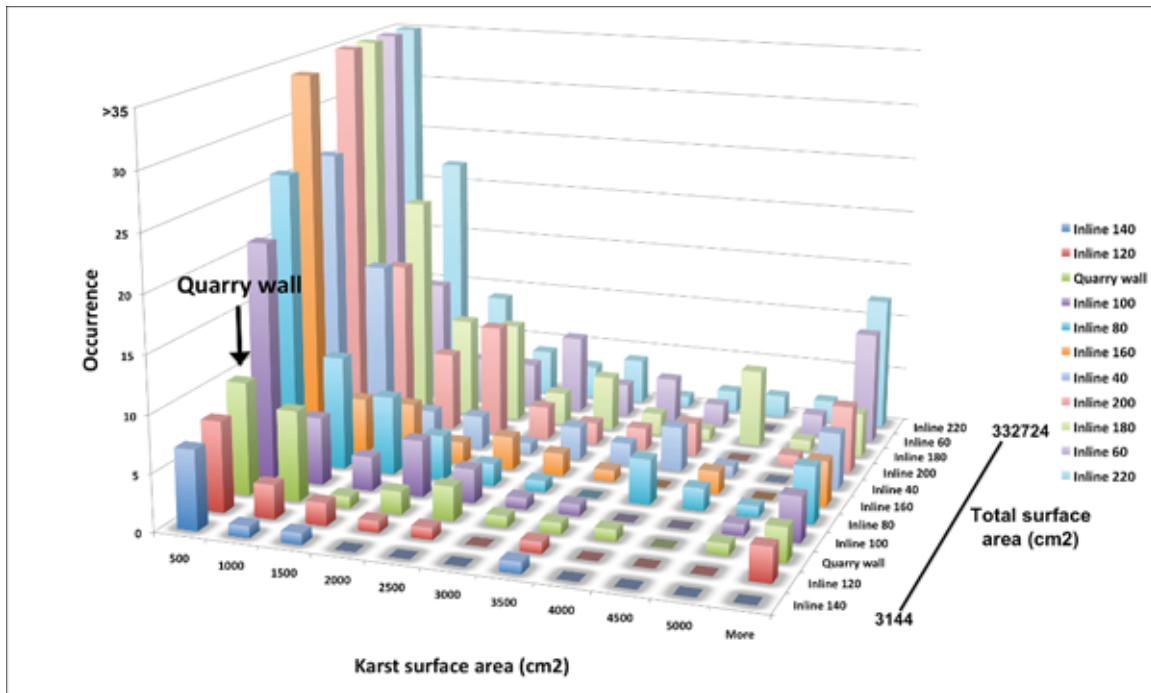


Figure 4. Comparison between size-frequency distribution of karst surface area in the quarry wall (yellow) and in the 2D inlines. The total karst surface area of the quarry wall falls within the range of karst surface area of the 2D inlines, indicating that the volume extraction yields accurate results.

Implications

The ability of 3D GPR to image decimeter to meter scale karst and quantify their volume has implications when estimating karst-related porosity in carbonate reservoirs. On reflection seismic data these karst features will be below resolution and calculation of the actual total porosity is likely underestimated when only matrix porosity and large-scale karst is taken into account. Results of this and similar studies will help assess the volume of fracture related karst.

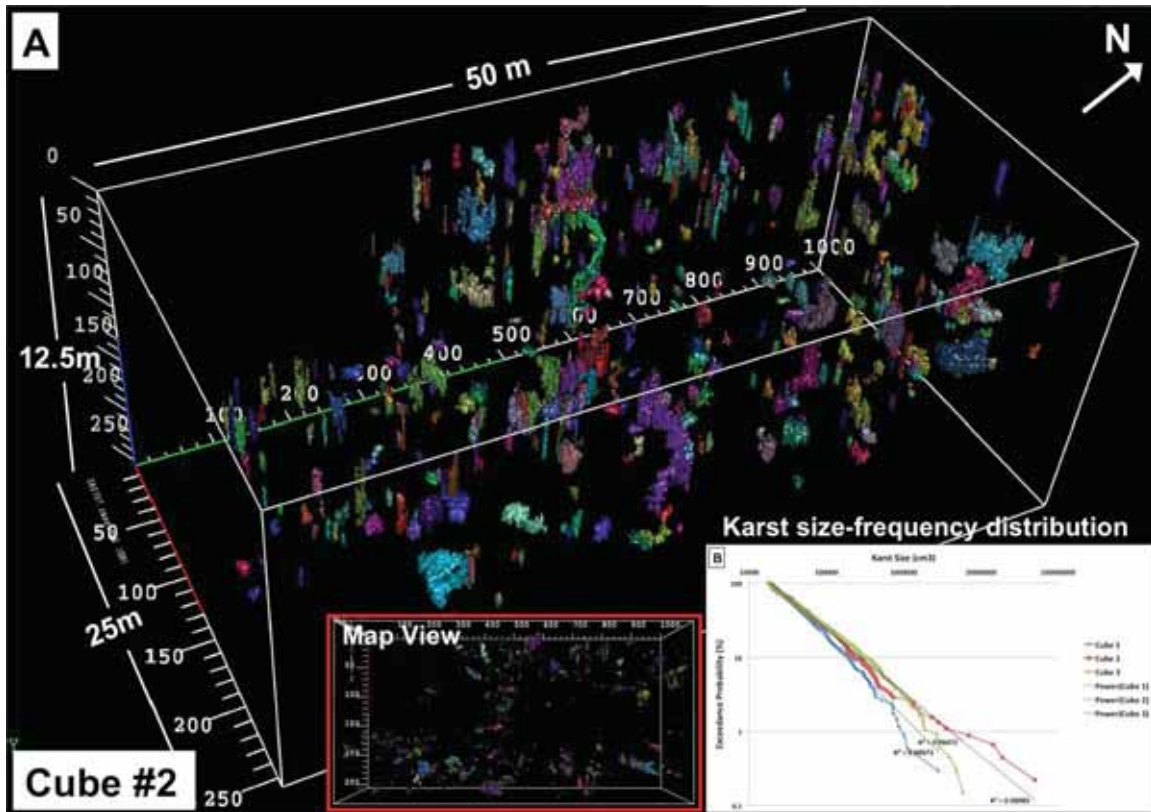


Figure 5. A. Distribution of karst in the 3D GPR cube (cube no.2). B. Cross-plots between karst size (cm^3) against exceedance probability (%) in all three 3D GPR cubes in a log-log scale, showing a power-law distribution. There is a bigger possibility for the occurrence of small karst compare to the large karst.

References

- Hoak, T.E., Sundberg, K.S., Ortoleva, P. and Shebl, M., 1998, Discrimination between karst and tectonic fractures in the Ellenburger Formation, West Texas: Implications for exploration models, AAPG poster session abstract, AAPG annual meeting, Slat Lake City, UT.
- Guangpo, C., Wenqing, P., Liming, S., Jianfa, H. and Wensheng, G., 2005, Application of prediction techniques in carbonate karst reservoir in Tarim Basin. Applied Geophysics, Vol.2, No.2.
- Masse, J.P., Fenerci, M., Pernarcic, I., 2003, Palaeobathymetric reconstruction of peritidal carbonates Late Barremian, Urgonian, sequences of Provence (SE France). Palaeogeography. Palaeoclimatology. Palaeoecology. 3132, 1 – 17
- Loucks, R. G. and Anderson, J. H., 1985, Depositional facies, diagenetic terranes, and porosity development in Lower Ordovician Ellenburger dolomite, Puckett field, west Texas, in P. O. Roehl and P. W. Choquette, eds., Carbonate petroleum reservoirs: Berlin, Springer-Verlag, p. 19-38.
- Pomar et al. 2009 CSL abstract.

Tracking and Quantifying Fluid Flow in Fractured Cretaceous Carbonates with 4D Ground Penetrating Radar (GPR): Madonna della Mazza Quarry, Italy

Pierpaolo Marchesini, Mark Grasmueck, Gregor P. Eberli, Remke L. Van Dam

Key Findings

- 4D GPR surveys allow to resolve watercontent changes within a 20x10x10m fractured carbonate volume with 1% accuracy in a 2 hours interval.
- Hydraulic properties of faults, deformation bands and porous matrix can be delineated at 1-10 m scale by tracking and quantifying water transport.
- Changes in characteristics of hydraulic properties are observed through time as a consequence of variations of hydraulic heads above wetting zones.

Goal of the study

Characterization of parameters controlling fluid flow in fractured carbonate rocks relies largely on 0.01-0.1 m scale sample measurements, upscaling, and modeling. We conducted a novel 1-10 m scale experiment by injecting and monitoring a moving water mass below a fractured grainstone quarry floor. Ground Penetrating Radar (GPR) was used to quantify local watercontent changes, delineate flooding/drainage boundaries, and determine the influence of faults and deformation bands on the fluid flow behavior.

Volumetric water content changes from 4D GPR

The Madonna della Mazza quarry is cut into a sequence of Upper Cretaceous rudist grainstones located in the inner part of the Majella anticline (Italy). Porosity values range from 27% to 35% and permeability from 150mD to 630mD. A total of 2952 liters of water were injected into the subsurface in 29 hours and 50 minutes. Sixteen repeated high-resolution 3D GPR surveys were acquired, 2 before and 14 after the infiltration during a monitoring period of 5 days. The sensitivity of GPR to subsurface watercontent changes allows to characterize the dynamics of wetting, saturation, and draining zones within a 20x10x10m GPR volume. Water slows down the propagation of the radar waves delaying the arrival time of the subsurface reflections. Event timeshifts between repeated surveys are related to subsurface water content changes. GPR reflection travel timeshifts from pairs of repeated surveys are extracted with a 3D warp algorithm, then quantitative fields of volumetric watercontent changes (θ_v) are generated by applying the Topp petrophysical transfer function (Topp et al., 1980). Results are visualized as a semitransparent attribute overlaying the regular 3D GPR data.

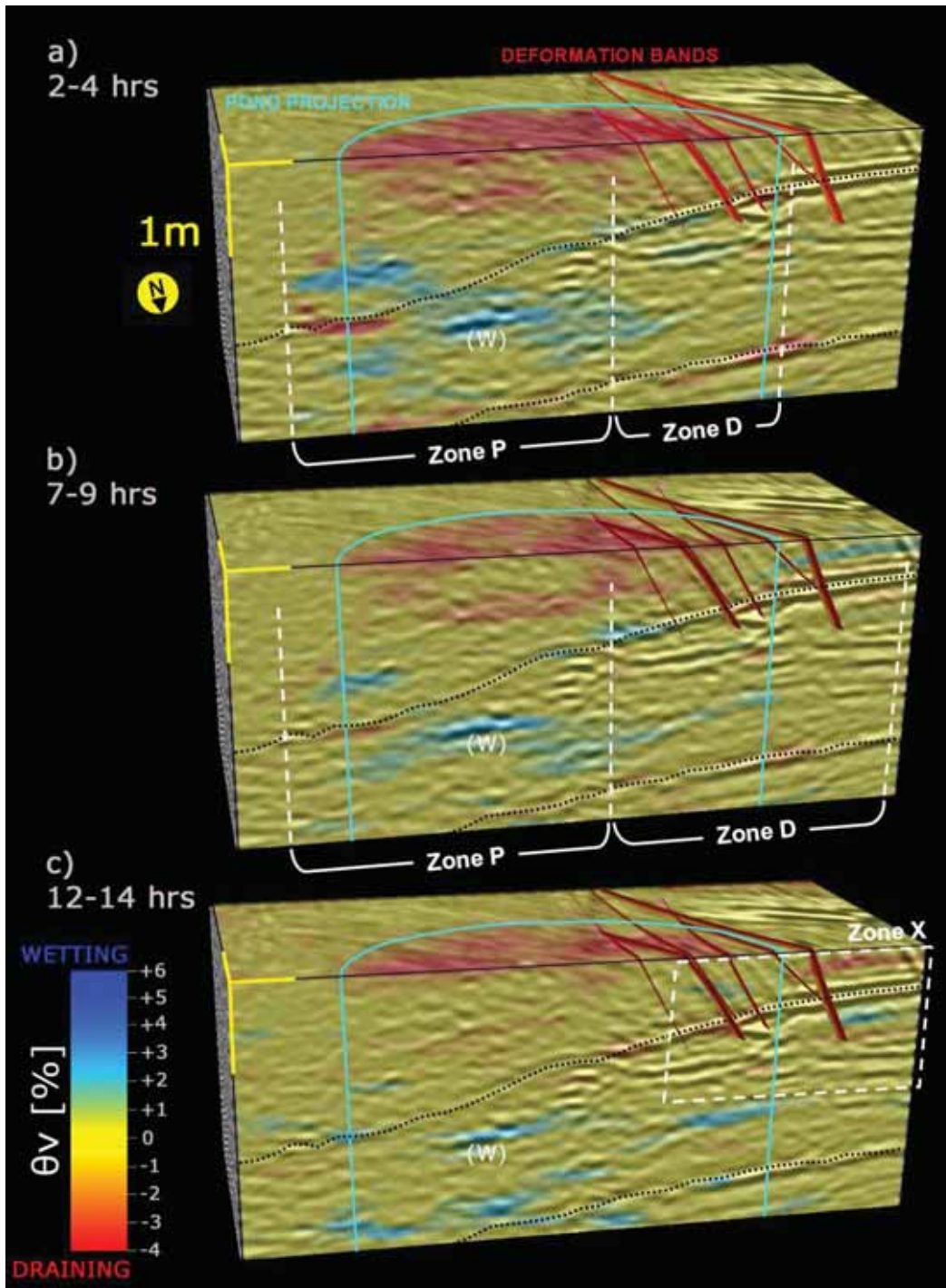


Figure 1: Two-hours snapshots of the computed watercontent changes for pairs of surveys acquired a) 2-4 hrs, b) 7-9 hrs and c) 12-14 hrs after the pond was removed. In a) peaks of 6% in watercontent changes in wetting zones indicate rapid fluid transport in the porous matrix (Zone P). In Zone D we observe less water transport. In b) watercontent changes decrease of a factor 2; in this stage fluid transport occurs across deformation bands (Zone D). In c) watercontent changes in a range of 1.5 - 2.5% show that deformation bands facilitate water transport across stratigraphic boundaries (Zone X). θ_v : volumetric watercontent change.

Deformation bands are responsible of lower watercontent changes

Volumetric watercontent changes have been computed with an accuracy of 1% for three different stages of infiltration using pairs of repeated 3D GPR surveys. Figure 1 shows two-hours snapshots of the watercontent changes produced with pairs of surveys acquired 2-4 hrs (Fig. 1.a), 7-9 hrs (Fig. 1.b) and 12-14 hrs (Fig. 1.c) after the pond was removed. For the 3 stages we observe differences in the distribution of watercontent changes. In particular: in Figure 1.a higher watercontent changes in Zone P than in Zone D suggest that the momentary wetting and drainage boundaries are mainly located in the undisturbed strata compared to zones including deformation bands. In this portion of the volume, characterized by porous matrix, we notice peak values of θ_v in a range of 4 - 6%. Moreover the lateral extension of the watercontent change clouds seems to follow the dipping stratigraphy. Values of θ_v lower than 1% in Zone D show that at this stage deformation bands reduce hydraulic conductivity. Deformation bands are a common strain localization feature found in porous rocks typically ranging from 5 to 10 mm thickness but do not represent slip surfaces. On the contrary, they are dipping sheets where grain crushing, rotation, compaction and frictional sliding along grain boundaries occurred (mechanism of cataclasis, Fig. 2). The decreasing of internal permeability relative to the surrounding rock matrix slows down the fluid flow across deformation bands (Fossen et al., 2007).

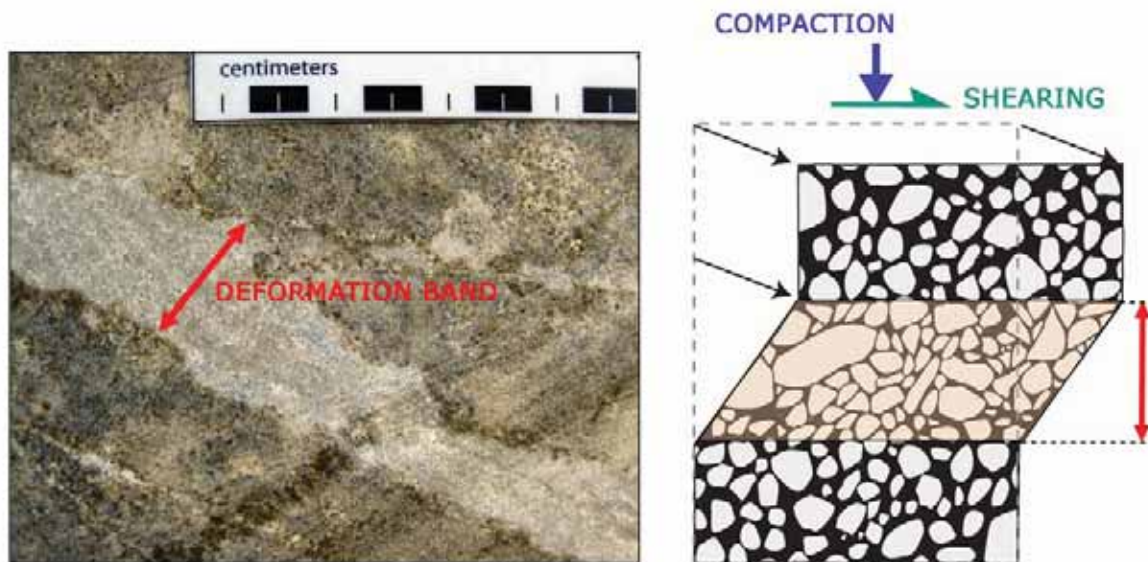


Figure 2: Deformation bands are dipping sheets where grain crushing, rotation, compaction and frictional sliding along grain boundaries occurred (cataclasis). Grain crushing during cataclasis results in loss of permeability (Modified from Fossen et al., 2007).

Figure 1.b shows a generalized decrease in magnitude of watercontent changes in Zone P whereas in Zone D wetting clouds start to appear across deformation bands with values of θ_v in a range of 2 - 3%. In the third stage (Fig. 1.c) water content changes lower down to 1 - 2% indicating a slow fluid propagation. In Zone X deformation bands now facilitate vertical water transport across stratigraphic boundaries enhancing flow parallel to their dipping direction with watercontent change values ranging between 1.5 and 2.5%.

In this last stage we can observe that watercontent changes in the shallowest portion of the rock volume did not decrease between the second and the third stage maintaining values of - 3-4%. This suggests that in the two-hours snapshot water evaporation occurred. The occurrence is supported by the observation that shallow and negative values of θ_v in the third stage are not balanced by deeper wetting zones as in the first and second stage. Moreover, the pair of 3D GPR surveys generating the last snapshot has been acquired in daytime with sun shining on the quarry floor.

In all the three stages we also noticed the presence of a localized wetting zone (W) with watercontent changes ranging from 5-6% (in the first stage) to 3-4% (in the last stage). The occurrence of these positive watercontent changes still has to be investigated.

Analysis of local watercontent changes

We investigated the relationship between values of θ_v and correspondent hydraulic heads to explain variations of watercontent changes among the 3 stages. Hydraulic heads are determined by measuring the saturated column of the watermass (the distance in depth between the bottom of draining and the top of wetting clouds). We determined hydraulic heads separately for porous matrix and deformation band areas. The maximum value of θ_v in the wetting cloud was associated to each correspondent hydraulic head. Results are shown in Figure 3: decrements of water heads through time correspond to linear decrease of watercontent changes in both porous matrix and zones with deformation bands. In particular, halving the water head causes halving the watercontent change percentage.

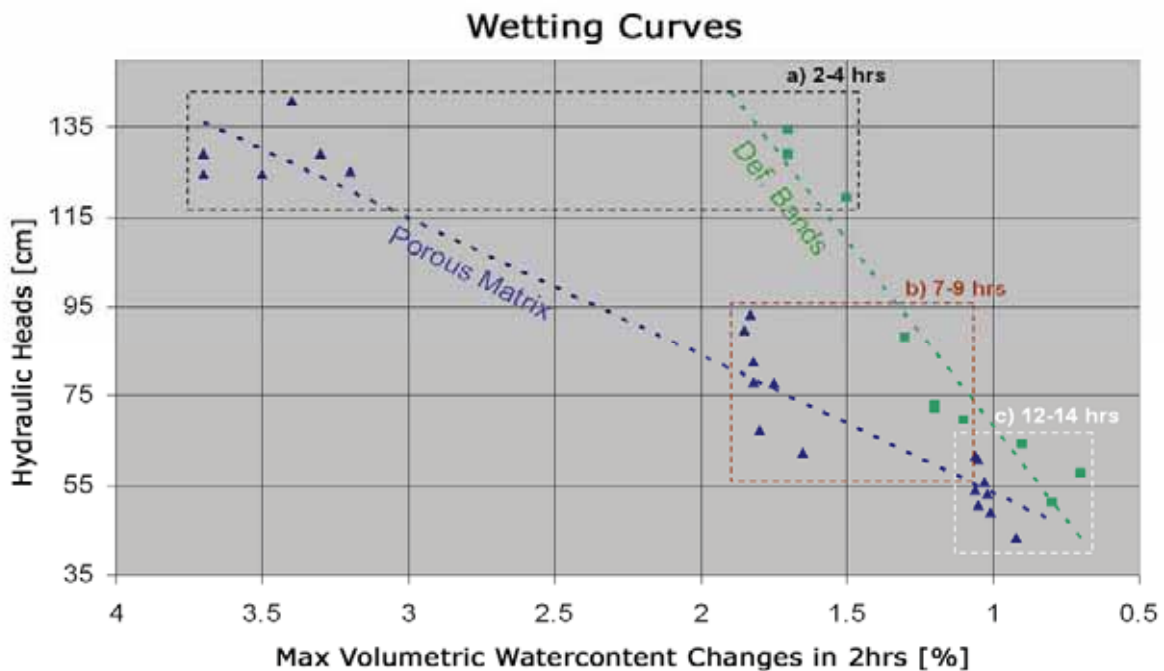


Figure 3: Hydraulic heads values plotted against maximum watercontent changes within the two-hours snapshot for porous matrix (blue) and deformation bands zones (green). Linear trend fits were applied to both plots. Results show that watercontent changes in the porous matrix are double the values observed in the deformation bands zones while maintaining hydraulic head constant.

Watercontent changes in the deformation bands zones (1.5 - 2%) are approximately half of the values measured in the porous matrix (3 - 3.5%) for the same hydraulic head in both stage a) and stage b). In the third stage we notice comparable values of θ_v in both zones validating the observation that, at this stage, water transport starts occurring in the deformation bands zone with the same mechanism than in the porous matrix. From a gravity driven water transport occurring in the first stage (greater hydraulic heads), a capillary driven transport now indicates that hydraulic properties changed over time. The occurrence is supported by the observation that within the second and third stage a largely spread distribution of wetting and drainage clouds also across deformation bands has been described.

Hydraulic heads are greater (average head=126cm) in the first stage a) than in b) and c): in this early stage the infiltrated waterbulb is still relatively shallow and homogeneous, there is more water available and watercontent changes are consequently higher (1.5 - 3.5%).

Open faults: fluid flow preferential paths

Vertical open faults are characterized by aperture varying from 0.5cm up to 10cm and are filled with sandy debris and colonized with grass and small bushes when exposed on the quarry floor. They cause a permeability increase representing preferential flow paths for the infiltrated watermass. Timeslices obtained from 4D GPR processing (Fig. 4) show the asymmetric distribution of higher values of watercontent changes along the fault plane and outside of the pond area experiencing same magnitude of θ_v values than in the porous matrix (+/- 3.5 - 4%). This indicates the active role played by the fault in conveying part of the infiltrated watermass otherwise propagating in the nearby porous matrix. Slow water transport occurs in the zone with deformation bands where both wetting and drainage zones experience low values of watercontent changes in a range of +/- 0.5 - 1%.

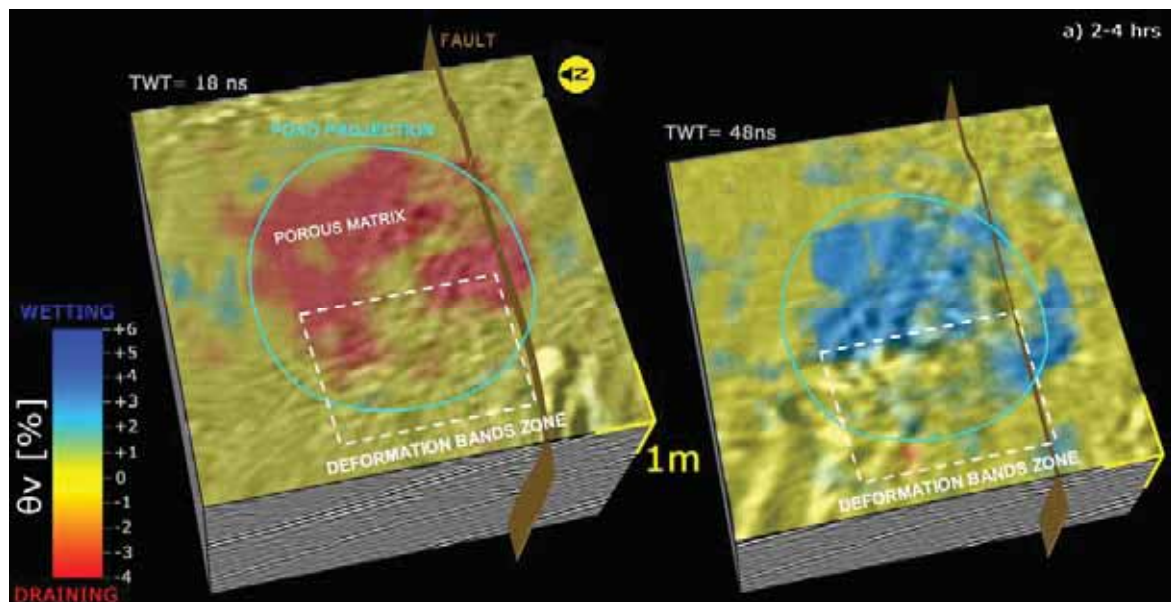


Figure 4: Asymmetric distribution along fault plane of watercontent changes for both draining (left) and wetting (right) boundaries. θ_v : volumetric water content change.

Conclusions

Time-lapse 3D GPR surveys used in a novel 1-10 m scale infiltration experiment allow to resolve volumetric watercontent changes within a 20x10x10m fractured carbonate reservoir with 1% accuracy in snapshots of 2 hours intervals. From data analysis we observed 3 distinct stages of fluid flow behavior due to a linear trend between θ_v and hydraulic heads. Variations of watercontent changes in time and space indicate the influence of faults and deformation bands in the water transport. Changes in characteristics of hydraulic properties are observed through time as a consequence of variations of hydraulic heads above wetting zones. Vertical open faults are characterized by high transmissibility and represent preferential flow paths for the infiltrated watermass.

References

- Topp, G. C., Davis, J. L., Annan, A. P., 1980, Electromagnetic Determination of Soil Water Content: Measurements in Coaxial Transmission Lines, *Water Resource Research*, Vol. 16, No. 3, Pages 574-582.
- Fossen, H, Schultz, R., Shipton, Z., Mair, K., 2007, Deformation Bands in Sandstone: a Review, *Journal of the Geological Society, London*, Vol. 164, pp. 755-769.

Effect of pore structure on electrical resistivity in carbonates

Klaas Verwer, Gregor P. Eberli & Ralf J. Weger

Key Findings

- The cementation factor of 72 carbonate samples varies from 1.72 to 4.14.
- Porosity is the most important factor influencing electrical resistivity but there are large departures from this general trend. The departures are related to the pore structure.
- Mineralogy (limestone vs. dolomite) and effective pressure have a limited effect on resistivity.
- Permeability displays an unexpected correlation to resistivity. Samples with low fluid permeability have the highest cementation factor. Samples with low permeability have lower cementation factors.

Introduction

The electrical resistivity log is a powerful tool for lithological discrimination, correlation, hydrocarbon indication and calculation of water saturation (Doveton, 1994; Schlumberger, 1972, 1974). The resistivity tool primarily responds to changes in the electrical conductivity of the rock matrix and pore fluid. Because the flow of electric charge is controlled by the size, shape and connectivity of the pore structure, a link between the electrical resistivity and the carbonate pore structure has been inferred, though there is no detailed understanding of this relationship (Archie, 1942; Bigalke 2000). This study closes this gap by correlating measured electrical resistivity to quantitative pore structure parameters derived using digital image analysis (DIA).

Data Set and Measuring Procedure

Seventy-one carbonate core-plug samples (1 in. [25.4 mm] and 1.5 in [38.1 mm] diameter by 1 to 2 in [25.4 to 50.8 mm] length) were selected from cores and outcrops at several locations in the Middle East, Australia, Italy, and the Bahamas. The Middle East samples are from the Khuff and the Shu'aiba Formation and are Permian and Cretaceous in age, respectively. The Australian samples are from drowned cool-subtropical platforms on the Marion Plateau and are Miocene in age (Ehrenberg et al. 2006). The Italian samples originate from Maiella Mountain and are Cretaceous in age. The samples from the Bahamas were taken from a Holocene stromatolite. The set of selected samples includes textures ranging from coarse-grained grainstone with interparticle to oomoldic porosity to fine-grained wackestone dominated by interparticle to intercrystalline porosity.

Complex electrical resistivity was measured using a four-electrode technique and measured over a range of frequencies created by a function generator (0.01 Hz and 100 KHz) using a NER Autolab 1000 system. All samples were saturated with brine with 35 ppt (NaCl) under vacuum for 48 hours. Before starting the measurement the samples were flushed with several volumes of pore fluid using steady state fluid flow at 2 MPa

pore pressure to ensure full saturation. The confining pressure of the surrounding oil was varied to produce a range of effective pressure conditions.

Relationship of Pore Structure and Electrical Resistivity

The cementation factor is calculated from the measured rock resistivity and porosity. It ranges from 1.72 to 4.14 for the data set and varies up to 2.5 units for any given porosity (Figure 1). High values for formation factor and cementation factor ($m > 3$) occur only in samples below 20% porosity with the highest variation in samples below 15% porosity. Samples with high amounts of microporosity ($> 20\%$) have low values for the formation factor for a given porosity and cluster around a cementation factor of 2 (Figure 1b). Generally there is an increase in formation factor with a decrease in microporosity for any given porosity

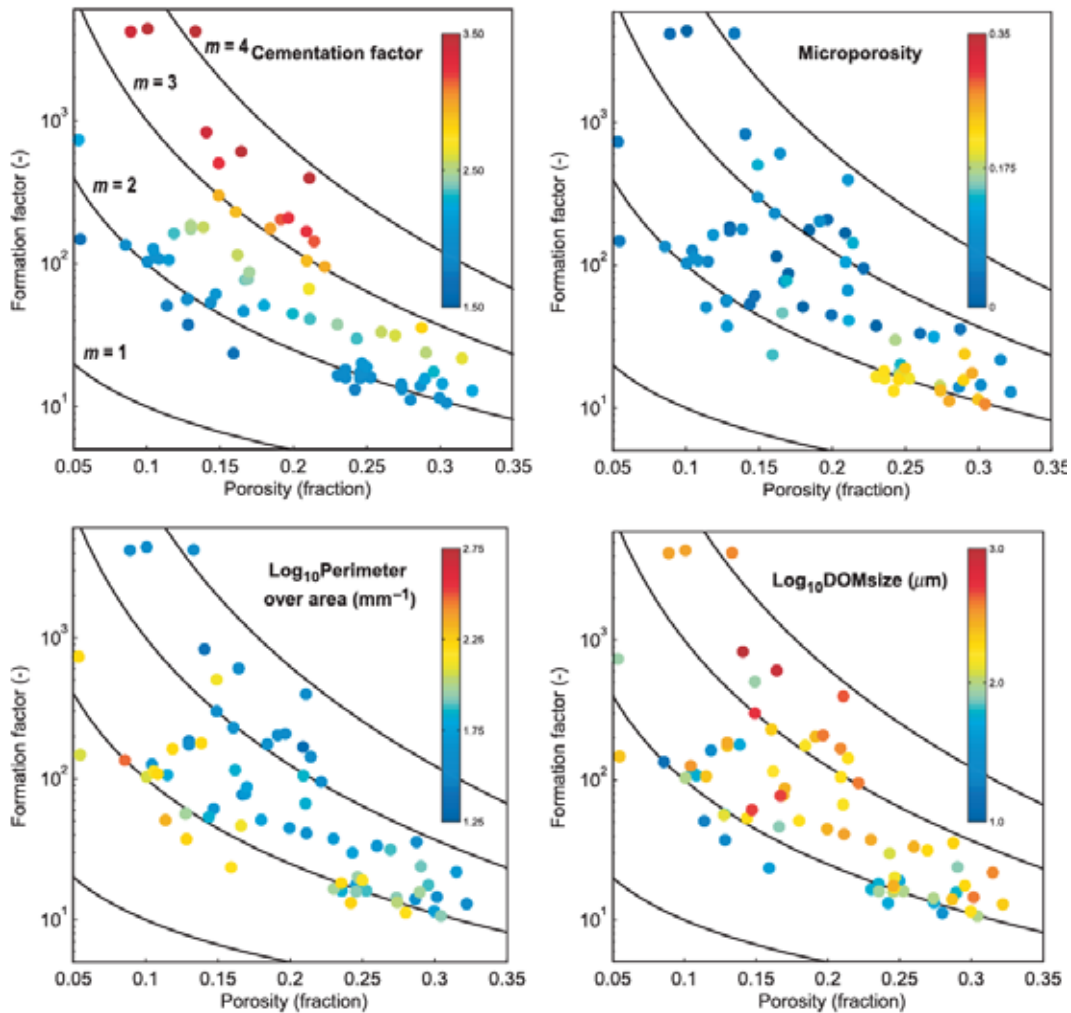


Figure 1. Cross plots of porosity versus formation factor with cementation factor (a), microporosity (b), and digital image analysis parameters perimeter over area (\log_{10} ; c) and dominant pore size (\log_{10} ; d) superimposed in color. Lines of equal cementation factor are shown. The cementation factor ranges from 1.75 to 3.5. All plots show a vertical gradient in parameter values at any given porosity indicating the correlation of formation factor and carbonate pore structure.

The digital image analysis parameters define distinct trends within the porosity-formation factor space. The parameters Dominant Pore Size (DOMsize) and Perimeter over Area (PoA) form trends in opposite direction (Figure 1c, d). The PoA displays a clear trend in which at any given porosity, samples with a low value of PoA (simple pore geometry) have relatively high formation factor values, whereas samples with high values of PoA (more complex pore network) have low formation factor values (Figure 1c). In other words, samples with simple pore geometries have higher resistivity than samples with complicated pore structures if the porosity is the same. The DOMsize also shows a clear trend with increasing values of DOMsize correlated to higher values for formation factor, i.e., higher resistivity. Samples with smaller DOMsize values have lower formation factor for a given porosity (Figure 3d). This indicates that for a given porosity samples with simple large pores have higher resistivity than samples with an intricate pore network dominated by small pores.

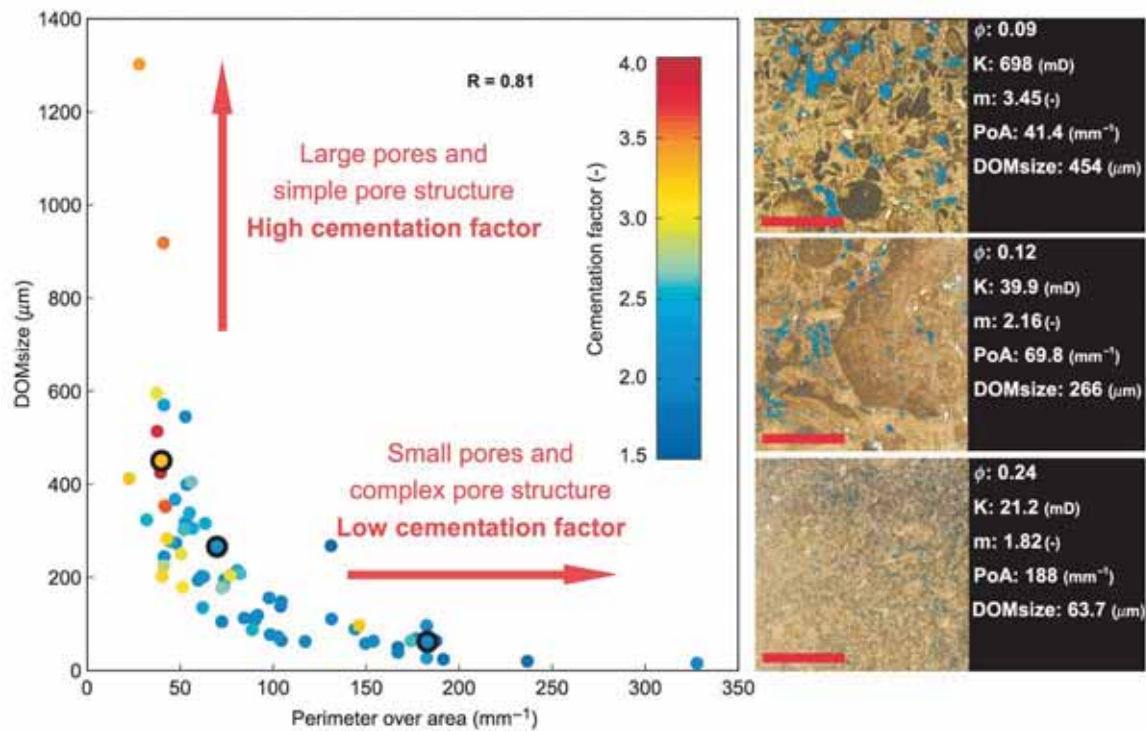


Figure 2. Cross plots of perimeter over area (PoA) versus dominant pore size (DOMsize) with cementation factor superimposed in color. Photomicrographs illustrate carbonate pore types corresponding to certain combinations of digital image analysis parameters. Scale bar is 2.5 mm. Observe correlation of pore structure parameters with cementation factor.

The cross plot with the cementation factor superimposed in color (Figure 2) illustrates the link between the two geological parameters PoA, DOMsize, electrical resistivity and rock texture. Three thin section images are shown to illustrate the difference in pore structure detected by high, medium, and low parameter values. Low-resistivity samples (cementation factor values below 2) are characterized by DOMsize lower than 200 μm and PoA greater than 60mm⁻¹. The corresponding thin-section images are dominated by small pores, a significant amount of small particles, and/or abundant

microporosity (Figure 2). In contrast, higher resistivity samples (cementation factor values greater than 2.5) are characterized by DOMsize above 300 μm and PoA below 70mm^{-1} . The corresponding thin section images show larger pores, larger particles, and little to no mud (Figure 2). In general, high resistivity corresponds to samples with simple and large pores with smooth pore surfaces, low specific surface, and a small amount of microporosity.

Relationship of Cementation Factor and Permeability

Carbonate pore structure has a strong control on permeability (Lucia, 1995; Weger et al. 2009). The size and geometry of the pores and their connections control the ability for fluid to flow. There is an increase in permeability with an increase in porosity but variations in permeability of several orders of magnitude at any given porosity are common. Generally, samples with high values of PoA and low values of DOMsize have low permeability for a given porosity. In contrast, samples with low values of PoA and high values of DOMsize have high permeability. An exception is presented by a number of samples which do have high values of DOMsize but a low permeability. These samples are dominated by oomoldic porosity which provides high, but non-connected porosity. From the data, it appears that samples with large pores and a simple pore structure have high permeability, if not oomoldic, and that samples with an intricate pore network have lower permeability.

In Figure 3 the cementation factor is compared with porosity-permeability trends. Samples with a cementation factor between 1.7 and 2.1 (dark blue colors) plot more or less on a straight line, displaying an increase in permeability with an increase in porosity. Those samples contain relatively low permeability for a given porosity. A number of samples have high values for the cementation factor (>3.0) accompanied by low permeability (red circles at low permeability). Those samples represent the porosity types where pores are unconnected (e.g. oomoldic porosity). This pore structure has a negative influence on the permeability and inhibits the flow of electric charge producing a high cementation factor. For a constant porosity an increase in permeability is accompanied by an increase in cementation factor. For example, in samples with 23 to 25% porosity the cementation factor increases from 1.8 to 2.9 as the permeability increases from 2.5 to 1400 mD (Figure 3). The grainstone samples have higher permeability *and* higher cementation factor than the wackestone example.

Implications

Electrical resistivity in carbonate rocks displays a remarkably wide range up to over one order in magnitude at any given porosity. The drastic changes in resistivity affect inversion of pore structure from resistivity logs and calculations of water saturation. The drastic changes in resistivity affect inversion of pore structure from resistivity logs and calculations of water saturation. Comparison of measurements of electrical resistivity with quantified pore structure data (through digital image analysis from thin sections) yielded the following results:

In carbonates the cementation factor of Archie's Law ranges from 1.72 to 4.14. Porosity is the most important physical factor that influences electrical resistivity.

Formation factor decreases with increasing porosity, but there are large departures from this general trend.

Mineralogy, limestone vs dolomite, and effective pressure have limited effect on variations in resistivity.

Different resistivity in rocks with equal porosities is the result of the carbonate pore structure. Quantitative digital image analysis parameters, perimeter-over-area and dominant pore size, show a strong correlation to variations in electrical resistivity.

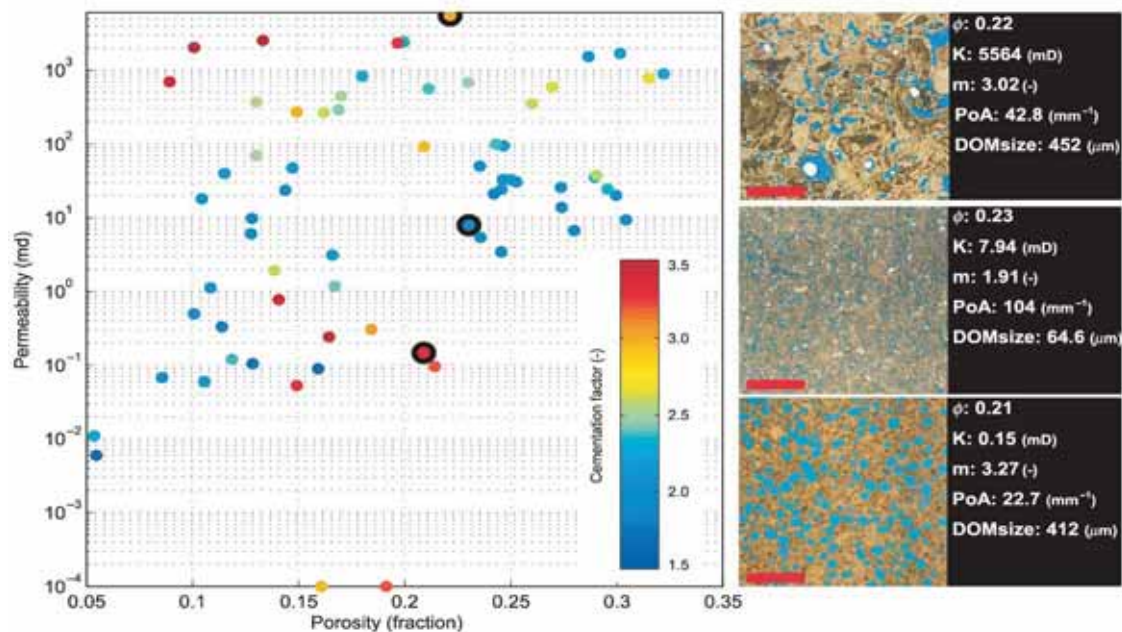


Figure 3. Porosity-permeability cross plot with cementation factor superimposed in color. It is evident from the graph that samples with high permeability have higher cementation factors for a given porosity. This is related to the pore structure; large simple pores facilitate fluid flow, while small intricate pore networks inhibit the flow of fluid. An exception is formed by the samples with separate vug porosity, which inhibit the flow of both electric charge and fluid. As a consequence those samples have low permeability combined with a high cementation factor.

Samples with highest cementation factor have low fluid permeability as the unconnected pore structure inhibits the flow of fluid and the flow of electric charge. Samples with intermediate cementation factor and a simple pore structure, however, have higher permeability than samples with an intricate pore structure along with lower values for the cementation factor. The dense pore network in intricate pore structures promotes the flow of electric charge, while the reduced number of pores and pore connections in simple pore structures limits electric connectivity.

In summary, the electrical resistivity in carbonates is controlled by the carbonate pore structure rather than cementation. The large variation in the cementation factor shows the difficulty of calculating water saturations in carbonate reservoirs in the absence of knowledge about the carbonate pore structure. In addition, the notion that high resistivity

rocks are cemented and hence have low permeability seems to be more complicated as high resistivity rocks can have high permeability. Given the relationship between permeability and the DIA parameters, PoA and DOMsize, in theory it should be possible to discriminate high and low permeability at a given porosity directly from well-log data (with knowledge of the conductivity of the pore fluid). Secondly, it is beneficial for an accurate interpretation of log-based pore-type estimates and drastically improves calculations of water saturation from down hole logging data.

References

- Archie, G.E., 1942, The electrical resistivity log as an aid in determining some reservoir characteristics: *Petroleum Transactions of AIME (Am. Inst. Min. Metall. Eng.)*, v. 146, p. 54-62.
- Archie, G.E., 1947, Electrical resistivity an aid in core-analysis interpretation: *American AAPG Bulletin*, v. 31, p. 350-366.
- Bigalke, J., 2000, A study concerning the conductivity of porous rock: *Physics and Chemistry of the Earth (A)*, v. 25, p. 189-194.
- Doveton, J. H., 1994, *Geological log interpretation—Reading the rocks from wireline logs: SEPM Short Course 29*, 169 p.
- Ehrenberg, S. N., G. P. Eberli, and G. Baechle, 2006, Porosity-permeability relationships in Miocene carbonate platforms and slopes seaward of the Great Barrier Reef, Australia (ODP Leg 194, Marion Plateau): *Sedimentology*, v. 53, p. 1289-1318.
- Schlumberger, 1972, *Log interpretation, Vol. I: Principles*: New York, Schlumberger Limited, 113 p.
- Schlumberger, 1974, *Log interpretation, Vol. II: Applications*: New York, Schlumberger Limited, 116 p.

Sonic Velocity of Holocene Interparticle Porosity Rocks

*Gregor P. Eberli, Ralf Weger, and Klaas Verwer**

**Statoil, Bergen Norway*

Key Findings

- Holocene hardgrounds within ooid shoals at the Tongue of the Ocean (Bahamas) are cemented by early marine fibrous aragonite and micritic cements.
- Hardgrounds samples have a simple pore system with variable pore sizes.
- Compressional wave velocities range from 3094 to 4995 m/s at 25MPa and display little change with increasing effective pressure.
- Small amounts of early marine cements can produce a stiff, acoustically fast, and compaction resistant rock that maintains primary porosity to great burial depth.

Interparticle porosity and rock stiffness

In rock physics models interparticle porosity rocks are usually considered to be a medium with somewhat compliant pore structure, and consequently as rocks with low stiffness and slow acoustic velocity. In contrast, rocks with moldic and vuggy porosity are classified as stiff, high aspect ratio rocks, resulting in high bulk modulus and velocity (e.g. Nurmi, 1984; Lucia and Conti, 1987; Wang and Lucia, 1993). This general rule is not always applicable, because rocks with interparticle porosity can achieve stiffness and high velocity at relatively high porosity, if the particles are cemented together at the grain contacts. Such grain-welding cements occur for example in stromatolites (Figure 1).

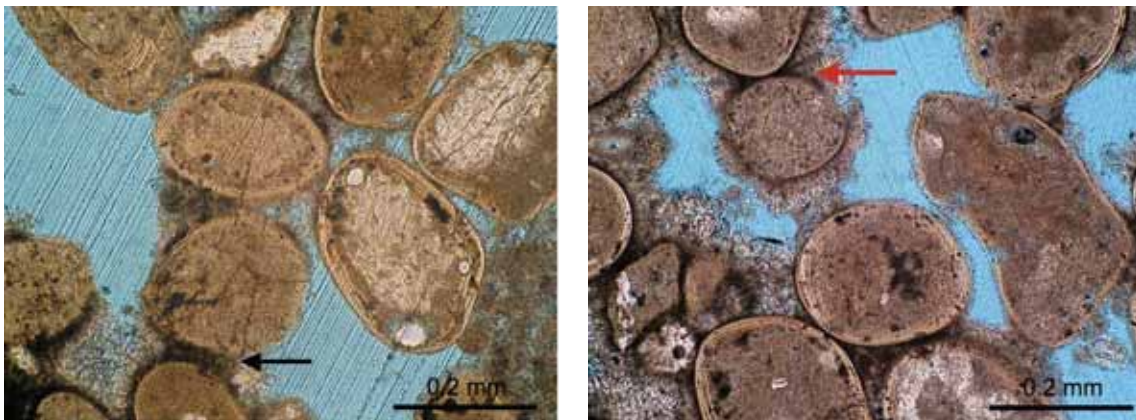


Figure 1: Photomicrographs of modern stromatolites from the Bahamas. Grains are cemented by a dark micritic cement (arrows). Fine aragonite needles overgrow these micritic contact cements. Both cements increase the stiffness of the rock, inhibiting compaction and increasing the acoustic velocity.

In 8 modern stromatolite samples velocities range between 4480 - 5420 m/s while porosities are relatively high (12-25%), making them faster than Wyllies' time average equation would predict. They are all at the high end of velocities at any given porosity but all have high permeability. The geological process responsible for these physical

properties is microbial induced cementation at grain contacts that produces a stiff frame in these young stromatolites.

Incze (1999) documents that early marine diagenesis in form of micritic cements at grain contacts is a potential mechanism to produce a young stiff rock. He measured in grainstone with only 12% contact cement and a high P-wave velocity of 4500 m/s that is maintained even as confining pressure is increased from 5 to 80MPa. This single rock sample indicates that small amounts of contact cements can preserve primary porosity to great burial depths. To test this finding we measured 23 samples from submarine hardgrounds in the Bahamas. The samples are from an ooid shoals in the southern Tongue of the Ocean, where they are embedded in Holocene sediment.

The Cements of the Modern Hardground Samples

Micritic and fibrous aragonitic cements are the dominant cements in the Holocene submarine hardgrounds. The first cement is often a micritic rim around the ooid grains. The fibrous aragonite cement subsequently forms an isopachous cement in the pore space (Figure 2). At many grain contacts a dark micritic cement is observed that is reminiscent of the marine meniscus cement described by Hillgärtner et al. (2001) (Figure 2).

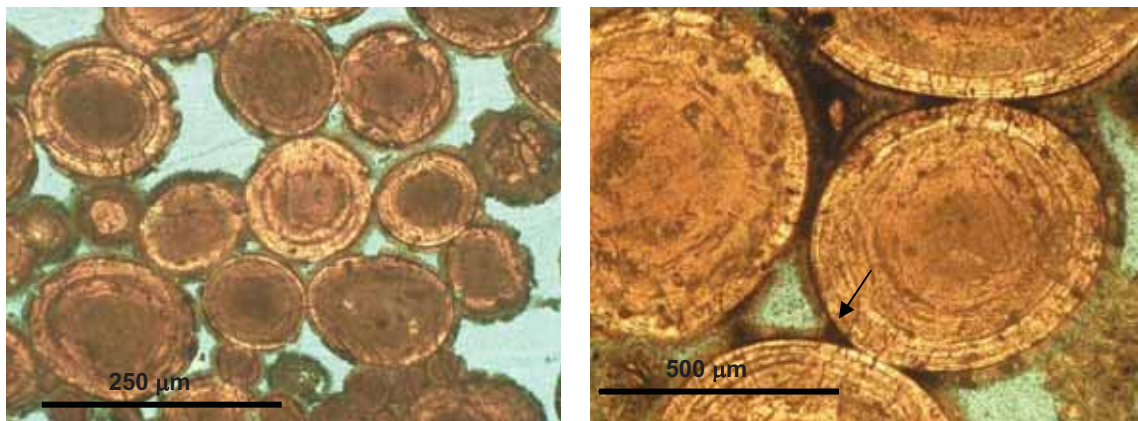


Figure 2: Photomicrographs of two submarine hardground samples investigated in this study. Left: Ooid grains are coated by a micritic rind that is overgrown by fibrous aragonite cement. Right: Micritic meniscus cement (arrow) welding two ooids together. In addition, micritic material is filling part of the pore space.

The Pore System of the Modern Hardground Samples

The main pore type of all hardground samples is interparticle. Using digital image analysis parameters this uniform pore structure can be quantified. The aspect ratio is very uniform, reflecting the similar pore type; it ranges between 0.54 and 0.62. Likewise the Perimeter over Area (PoA), which is a measure of the complexity of the pore structure, displays little variations; it ranges between 0.32 – 76.4 mm⁻¹. The dominant pore size (DOMsize) on the other hand shows large variations. It ranges from 203 – 1100 µm. In summary, the pore system of the investigated samples is characterized by simple pores of variable size (Figure 3).

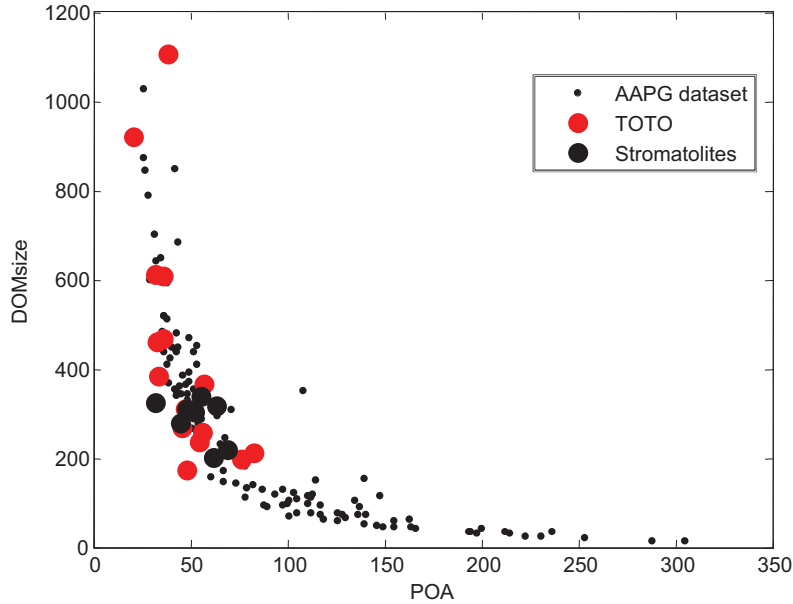


Figure 3: Characterization of the pores system of the hardground samples (TOTO) with digital image analysis parameters and a comparison with stromatolites and the data set of Weger et al., (2009).

The TOTO samples have simple (small PoA) pores of variable size (DOMsize).

Acoustic Properties

V_p values range from 3094 to 4995 m/s, while porosities range from 13 – 42%. The most important characteristic of the acoustic behavior is the lack of velocity increase with increasing pressure (Figure 4). In most (low and high velocity) samples, velocity remains nearly constant when pressure is increased to 35 MPa.

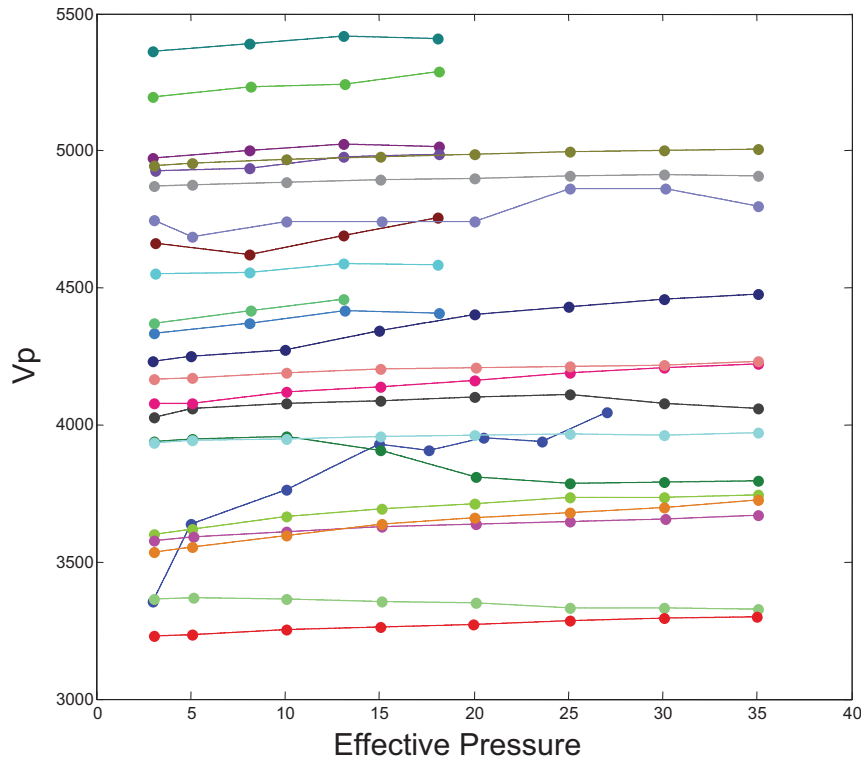


Figure 4: V_p versus effective pressure of hardground samples (3-35 MPa) and stromatolites (3-20 MPa).

Most samples do not display a strong increase with increasing pressure.

Conclusion and Implications

Early marine cements weld carbonate grains together to form a stiff rocks that are capable to maintain their initial acoustic properties under high effective pressure. This acoustic behavior documents that interparticle porosity rocks can resist compaction and maintain primary porosity to great burial depth, while having a high acoustic velocity.

References

- Hillgärtner, H., Dupraz, C. and Hug, W., 2001, Microbially induced cementation of carbonate sands: are micritic cements indicators of vadose diagenesis? *Sedimentology*, v. 48, p. 117-131.
- Lucia, F.J. and R.D. Conti, 1987. Rock fabric, permeability, and log relationships in an upward-shoaling, vuggy carbonate sequence. The University of Texas at Austin, Bureau of Economic Geology, Geological Circular 87-5, 22 p.
- Nurmi, R. D., 1984, Carbonate pore systems: porosity/permeability relationships and geological analysis: *AAPG Bull.* V. 68, no. 4, p. 513-514.
- Wang, R.F.P. and F.J. Lucia 1993. Comparison of empirical models for calculating the vuggy porosity and cementation exponent of carbonates from log responses. The University of Texas at Austin, Bureau of Economic Geology, Geological Circular 93-4, 27 p.
- Weger R. J. Weger, Eberli, G. P., Baechle, G. T., Massaferro, J. L., and Sun, Y.F., 2009, Quantification of pore structure and its effect on sonic velocity and permeability in carbonates. *AAPG Bulletin*, v. 93/10, p. 1-21.

From Sediment to Rock: Velocity Evolution during Controlled CaCO_3 precipitation

Ralf J. Weger, Peter Swart, and Gregor P. Eberli

Key Findings

- Even small concentrations of CaCO_3 in solution can produce substantial precipitation of both calcite and aragonite (1-5% of porosity reduction) within only a few days.
- Initial precipitation of calcite cement in the transformation of ooid sediment to rock significantly alters the acoustic velocity (up to 300m/s increase) .
- Very small amounts of Mg appear to be responsible for precipitation of aragonite while inhibiting precipitation of calcite.
- Regular DI water dissolves $\sim 150\text{mg}$ of CaCO_3 from ooids within minutes.

Introduction

In the past, experiments on the influence of rock fluid interaction examined the temporary, reversible effects of pore fluids on the rocks framework and its acoustic properties (Baechle et al., 2009, Verwer et al., 2010, Fabricius et al., 2010). Ongoing studies assess the influence of early cementation on the rock stiffness, porosity preservation and acoustic properties. In this study the main objective is to capture the acoustic evolution during the transformation of the sediment to the rock.

To achieve this goal an experimental setup is needed that allows for the production (or dissolution) of calcite cement by filtration of pore fluids that are either under or supersaturated with respect to CaCO_3 and the simultaneous measurement of acoustic velocity. The challenge in this experiment is to produce a rock in a timely and

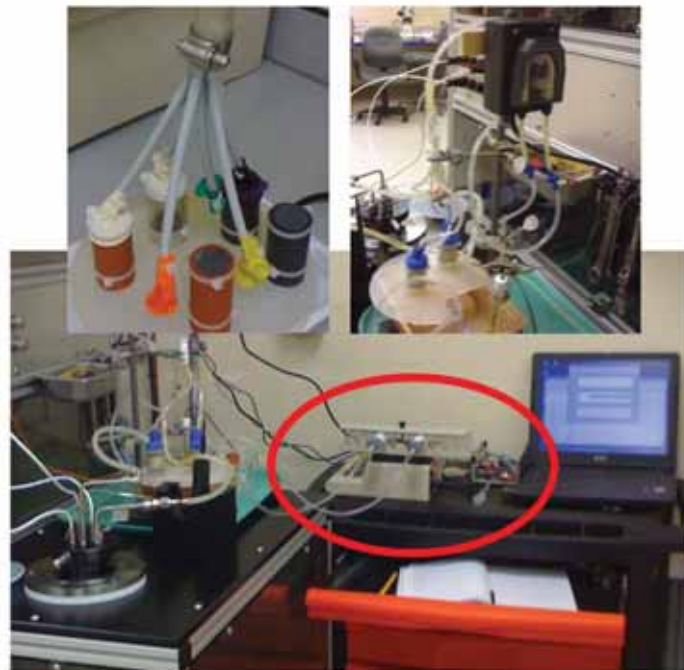


Figure 1: Overview of the continuous filtration system that is used to circulate pore fluids through sediment to precipitate cement: peristaltic pump (top right), solution distribution octopus (top left), and dosing syringe pump with microcontroller (center, red oval).

chemically controlled fashion while at the same time measuring the rocks acoustic properties. Here we report on our first attempts to (1) design equipment and workflow that will allow for continuous filtration of rocks with controlled pore fluids (regulated pH and temperature) while monitoring the rocks acoustic properties and assessing changes in other physical properties such as weight and volume; (2) assess the feasibility of methods that will induce measurable changes to the rocks acoustic properties while maintaining chemical properties that are realistic compared to natural settings; and (3) assess the timing required for such changes. In the longer term, questions addressing precipitation of calcite vs aragonite, and a more accurate determination of the influence of temperature variations are to be addressed.

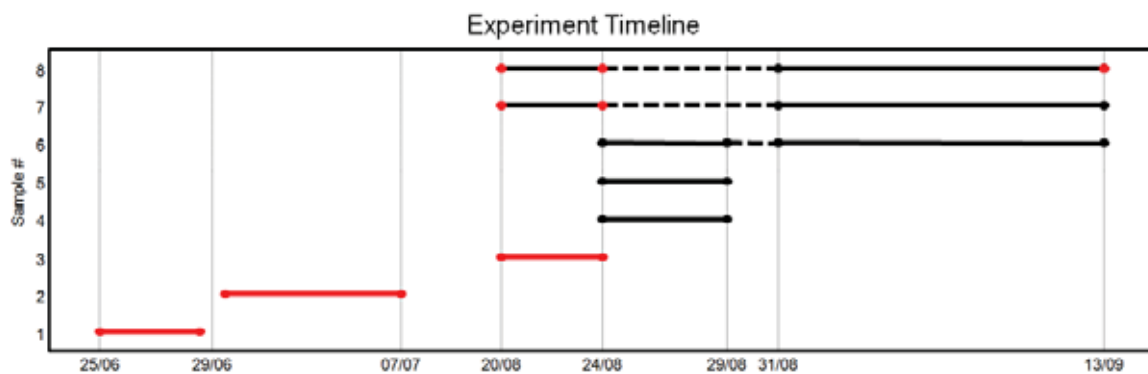


Figure 2: Experiment timeline showing length of experiment for 8 of the 9 samples analyzed. Red lines and dots show experiments/samples where acoustic velocities were measured. Dashed lines indicate interruption of analysis that continued on the same sample at a later time.

System Description

A filtration system was added to the NER Autolab1000 that allows for continuous filtration of rock samples and both monitoring and alteration of the fluid properties. An Aqua Medic SP 3000 peristaltic pump provides a continuous flow rate of 50ml/min or less if used with splitting octopus and multiple samples (Figure 1). Temperature and pH of the pore fluid are monitored using an Arduino microcontroller board in combination with MATLAB. The microcontroller logs data from the pH electrode and a temperature sensor in 5sec intervals. In addition, it controls a Corning Hot Plate/Stirrer and a KD Scientific 220 Multi-Syringe Infusion Pump to adjust fluid chemistry and temperature as needed.

The Experiments

So far, the 9 sediment samples (8 ooids, and 1 of mixed skeletal debris) were prepared and analyzed under different conditions (see Figure 2 for overview of experimental timeline). In the first two experiments, the sample was placed into the pressure chamber of the Autolab1000, and a solution was continuously pumped through this closed system for 90 and 160 hours, respectively. Fluid flow rate, temperature, and chemical composition were, however, captured at periodic intervals. Acoustic velocity (both compressional and shear) was measured every hour. In experiment #1 it was measured in 5 MPa increments up to 40 MPa and back to 10 MPa, and maintained there for ~90 hours. In experiment #2 it was measured in 5MPa increments up to 15 MPa and

then reduced to 5 MPa and held for ~160 hours. To increase the amount of CaCO₃ in solution the temperature of the fluid was elevated to ~35 degrees C.

To monitor and control the circulating fluid, the experimental setup was changed. Experiment #3 was performed with continuous logging of both temperature and pH in 5sec intervals. One sample was placed into the pressure chamber of the Autolab1000 while two samples remained outside under ambient pressure. Acoustic velocity was captured for all three samples at the beginning of the experiment at 3, 5, and 10 MPa. Sample Sleeve # 3, acoustic velocity was measured throughout the experiment in 1 hour intervals at 5 MPa. All three samples were continuously flushed with liquid at a constant flow rate of 50 ml/min. The solution consisted initially of DI water with a pH of 7.7 containing 24 mg Ca and 36 mg CO₃. The dosing pump contained 60 ml of each [0.25M] NaHCO₃ and [0.25M] CaCl₂ and administered the solution as needed in 0.1ml doses (~0.1mg Ca and ~0.15mg CO₃). In Experiment #4, no acoustic measurements were performed but an additional syringe in the dosing pump containing 60 ml of [.25M] NaOH administered NaOH as needed to maintain the initial pH in .1ml doses.

These initial experiments showed that a better estimate of the timing of the controlled precipitation is needed. As a result, the other experiments were performed outside the Autolab1000 without measuring acoustic velocity but changes in weight and volume of the samples were used to determine the amount of precipitation/dissolution. In addition, Scanning Electron Microscopy (SEM) was used to visualize the amount and type of precipitation on the ooids.

Preliminary Results

Precipitation Experiments

In the first two experiments, where a continuous flow of a premixed solution was circulated through the sample in the pressure chamber, acoustic velocity increased steadily throughout the experiment by ~ 100 m/s from ~2520 to 2620 m/s. SEM analysis revealed that many ooids were damaged by the initial high pressure and that only very small amounts of small crystals precipitated mostly within the solution and not on the ooids (Figure 3a). Thus, compaction rather than precipitation are likely responsible for the slight velocity increase. In the second experiment, CaCO₃ concentration was deliberately decreased while temperature was increased to avoid crystallization in the solution. After a small, initial increase in acoustic velocity of ~30 m/s, acoustic velocity remained basically constant throughout the experiment. SEM images reveal that some small crystals had precipitated on the ooids, but also a substantial amount of dissolution had occurred as ooids were partially dissolved (Figure 3b).

Consequently during experiment #3, the CaCO₃ concentration was kept close to but above saturation for ~90 hrs. SEM analysis clearly shows variable amounts of small crystals forming on all of the ooid surfaces (Figure 3 c-d). Many of these crystals formed directly at the grain to grain contact (Figure 4), fusing the ooids together into a more coherent unit. Acoustic velocity increased by ~50 m/s in one sample and by ~300 m/s in another. The small but consistent increase in compressional velocity is attributed to the formation of crystals at grain-grain contacts.

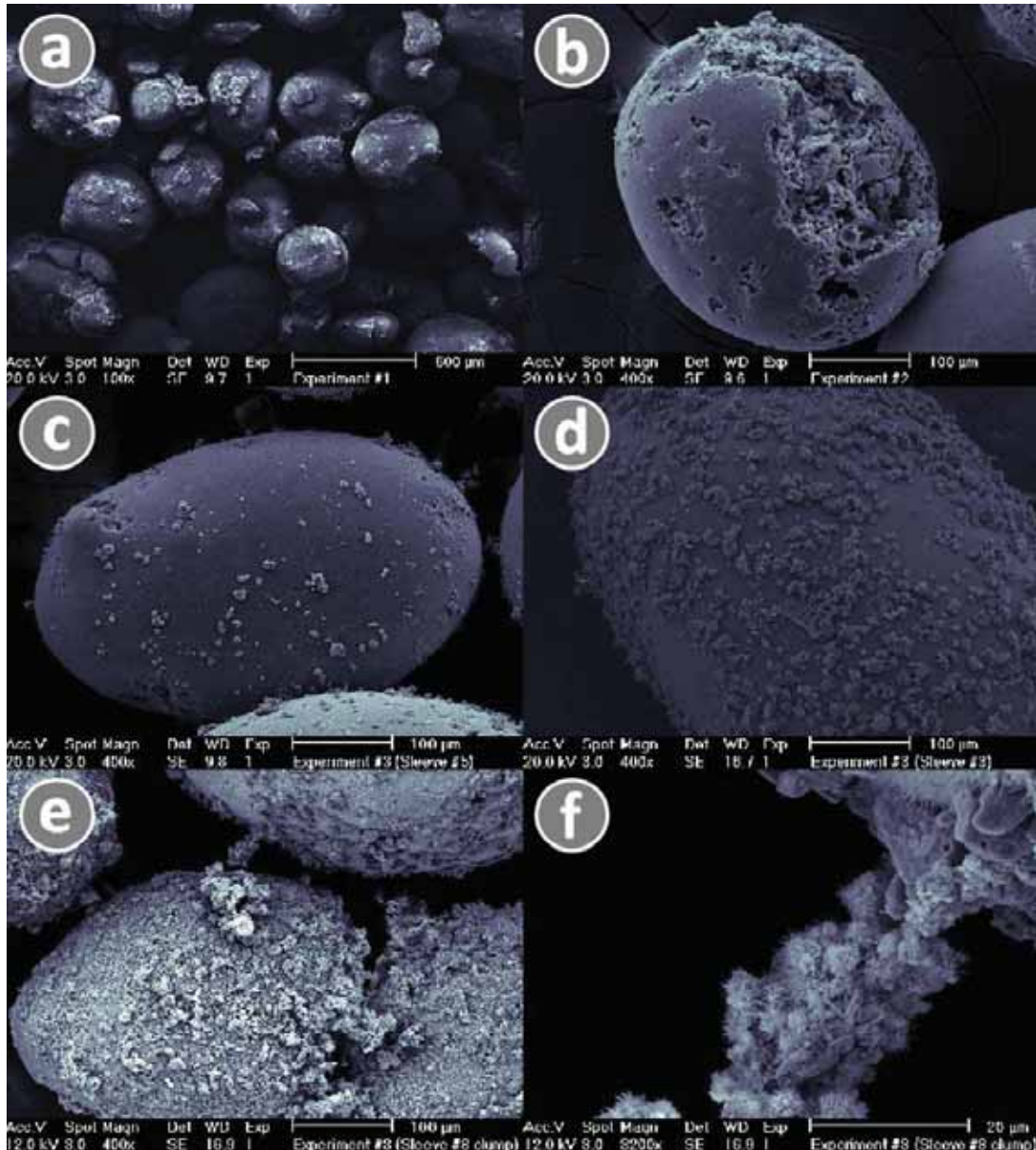


Figure 3: SEM images from different experiments. (a) Exp. #1, initial pressure damaged many ooids and only small amounts of precipitation occurred in ~90 hrs; (b) Dissolution of ooids in exp.#2 that had ~120 hrs of circulation at elevated temperature; (c-d) Exp.#3, 4 calcite precipitates on ooids that occurred in ~90 and ~120 hrs; (e-f) Examples of aragonite precipitation on samples of experiment 5 with controlled solutions over a period of ~13 days.

In samples from the subsequent experiments where filtration continued for two weeks while temperature and pH were monitored and logged, considerable amounts of precipitation occurred. SEM images show massive growth of aragonite as virtually all ooids are covered with a carpet-like blanket of aragonite needles. Flower-like structures formed between the ooids creating bridge-like needle structures (Figure 3e-f). Surprisingly, Mg was present in the circulating solution although no Mg was added. Obviously some dissolution occurred that freed Mg from the sample.

Dissolution Experiment

15g of clean ooids were filtrated with fresh DI water twice for 24 hrs and once for 72 hrs to investigate possible dissolution. During this period, pH and temperature were logged at 5sec intervals. Seven water samples were collected in the first 24 hrs and analyzed for chemical composition. The pH values of the water increased within 20 to 30 min from their original 4.8 to 5.3 to over 10. Chemical analysis of the collected water samples revealed that ~4.8 mg of Ca and ~1.3mg of Mg were taken up by the water in the first 40 minutes. During the initial 24 hours, the DI water was able to dissolve ~16.1 mg of Ca and ~3 mg of Mg. Within the 120 hours of the experiment, the DI water decreased the weight of the ooids by 317 mg (from 15g to 14.683).

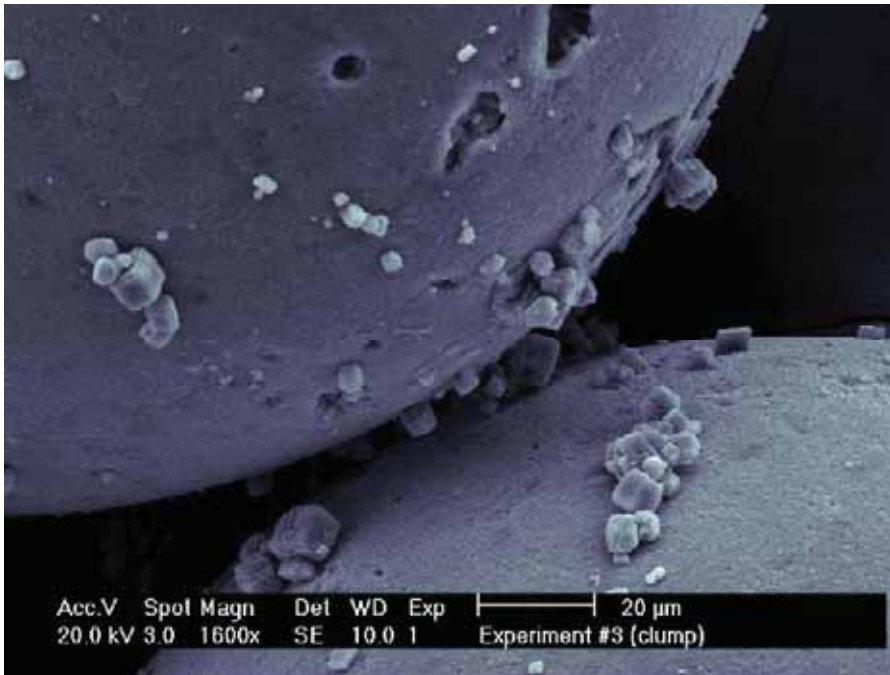


Figure 4: Crystals at the surface of the ooids and along the grain-grain contacts of the ooids.

Conclusion

All experiments produced permanent alteration of the ooids within only hours or days. The precipitation experiments show small but measurable increases in acoustic velocity, but velocities remained unchanged during minor dissolution.

References

- Gregor T. Baechle, Gregor P. Eberli, Ralf J. Weger, and Jose Luis Massaferro, 2009, Changes in dynamic shear moduli of carbonate rocks with fluid substitution, *Geophysics* vol. 74, no. 3, p. E135 E147
- Verwer, K., Eberli, G.P., Baechle, G. T., and Weger R. J, 2010, Effect of carbonate pore structure on dynamic shear moduli. *Geophysics*, v. 75/1, P. E1–E8. doi:10.1190/1.3280225
- Fabricius, I.L., Baechle, G. T., Eberli, G. P., 2010, Elastic moduli of dry and water-saturated carbonates - effect of depositional texture porosity and permeability. *Geophysics*, vol. 75/ 3, p. N65–N78, doi: 10.1190/1.3374690

